# Fabrication of zinc oxide based thin films and nanostructures for photocatalytic applications

by

Htet Su Wai

Student ID Number: 1246004

A dissertation submitted to the
Engineering course, Department of Engineering,
Graduate School of Engineering,
Kochi University of Technology,
Kochi, Japan

in partial fulfillment of the requirements for the degree of
Doctor of Philosophy

Assessment Committee:

Supervisor: Prof. Chaoyang Li
Co-Supervisor: Prof. Hiroshi Furuta
Co-Supervisor: Ass. Prof. Alexandra Apostoluk
Committee member: Prof. Hisao Makino
Committee Member: Prof. Toshiyuki Kawaharamura

September, 2023

# Abstract

## Fabrication of zinc oxide based thin films and nanostructures for photocatalytic applications

In past several decades, photocatalysis has become crucial for tackling environmental issues by efficiently breaking down harmful chemical pollutants and microorganisms. Recently, there has been great interest in the potential of metal oxides primarily based on zinc oxide (ZnO) for photodegradation. This can be attributed to their distinctive properties, involving a direct wide bandgap (3.37 eV), large exciton binding energy (60 meV) at room temperature.

The efficiency of ZnO in photocatalysis is greatly influenced by its surface morphology, wherein modifications of ZnO nanostructures, such as spheres, rods, tubes, and needles, play a pivotal role in improving photodegradation performance. Notably, in the ZnO crystal growth, the orientation along the (0001) crystal plane exhibits remarkable activity in photodegradation, because of its high surface energy and polar character of the (0001) crystal plane of ZnO. This polar facet enables efficient degradation of organic contaminants, thus leading to improved photocatalytic efficiency. Additionally, controlling the growth of large surface area is crucial, as it enhances the ability to absorb chemical reactants from the degradation process, facilitating the high production of reactive oxygen species (ROS) and contributing to improve the photodegradation efficiency.

Nevertheless, the rapid recombination rate of ZnO photogenerated charge carriers can weaken the photodegradation efficiency. Strategies to mitigate this recombination include surface modification, defects introducing, or incorporating transition metals by doping. Among these, aluminum (Al) doping has demonstrated promise in reducing electron-hole recombination rates. Various methods, such as atomic layer deposition, direct current or radio frequency magnetron sputtering, chemical vapor deposition, spray pyrolysis, and sol–gel processes, have been employed to introduce Al into ZnO films. Nevertheless, challenges persist in controlling the morphology, growth orientation, and cost-effectiveness of AZO films.

In this content, mist chemical vapor deposition has attracted interests due to its advantages, involving high uniformity, reproducibility, simplicity, controllability, and cost-effectiveness. In our prior success in depositing titanium dioxide films using this method, we plan to use the mist chemical vapor deposition process to deposit AZO thin films, exploiting on its potential for efficient photocatalysis. Addressing the challenge of growth direction and surface area, we propose a novel hybrid approach that combines radio frequency magnetron sputtering with mist

chemical vapor deposition. This synergistic technique aims to fabricate AZO films with controlled crystal growth orientation with a large surface area, thereby enhancing their performance in photocatalytic applications.

In summary, this research aims to contribute the photodegradation efficiency of ZnO by several innovative points:

1. Deposition of highly uniform ZnO films with varying thicknesses using mist chemical vapor deposition.
2. Fabrication of AZO films with different Al doping ratios by mist chemical vapor deposition to reduce the electron-hole pairs recombination rate. Investigation of the resultant photocatalytic efficiency.
3. Controlling the growth and crystallinity of AZO films via sputtered AZO seed layers with varying Al doping ratios through mist chemical vapor deposition. Investigation of the resultant photocatalytic efficiency.
4. Fabrication of well-aligned ZnO nanorods with different growth conditions through chemical bath deposition to enhance surface area and (0001) crystal plane exposure. Investigation of the resultant photocatalytic efficiency.
5. Fabrication of AZO/ZnO core-shells nanorods using mist chemical vapor deposition to reduce the recombination rate of electron-hole pairs and enhance the surface area to improve the generation rate of ROS species. Investigation of the resultant photocatalytic efficiency.

## 1. Fabrication of high uniformity ZnO thin films

To improve the photodegrading efficiency of ZnO-related thin films, we applied a novel mist chemical vapor deposition method to fabricate ZnO thin films with remarkable uniformity and high crystallinity. We systematically investigated the effect of varying film thicknesses on the characteristics of resulted ZnO thin films.

Resulting ZnO films exhibited a consistent and uniform surface. Despite this, an observable trend emerged as the average grain size was significantly increased with the thickness increasing from 300 nm to 750 nm. Moreover, the structure of the obtained ZnO films displayed an obvious improvement, with the emergence of a more defined columnar structure at high thicknesses. As the thickness increased from 300 nm to 750 nm, there was a clear enhancement in the crystalline quality observed in the direction of (002) growth. The high crystallinity was achieved at the 750 nm-thick ZnO film. The ZnO films with high crystallinity are expected to improve the photodegradation efficiency.

Furthermore, the increased film thickness significantly influenced the optical properties of the ZnO thin films. As thickness increased, there was a corresponding increase in optical transmittance. This increase in optical transmittance further enhances the potential of these ZnO thin films for effective photocatalysis.

In summary, through the innovative mist chemical vapor deposition method, we successfully fabricated ZnO thin films which was characterized by exceptional uniformity, high crystalline quality, and high transmittance. These developments established the improvement of ZnO-based photocatalytic efficiency, and offered the promising prospects for various applications.

### 2. Fabrication of aluminum doped zinc oxide thin films with varied aluminum ratios

In order to minimize the recombination rate of electron-hole pairs for ZnO, AZO films were fabricated on glass substrates using mist chemical vapor deposition method. We focused on investigating the influence of varying Al doping ratios, ranging from 1 wt% to 5 wt%, on the structural, optical and photocatalytic properties of the AZO films.

From XRD analysis, a significant diffraction peak corresponding to the (101) crystal plane was observed for AZO films exhibiting with increasing of Al ratios to 3 wt%. Significantly, the alteration of Al/Zn ratios caused a significant effect on the structural development of the AZO films. Specifically, a distinctive intertwined nanosheet morphology emerged under conditions where the ratios of Zn/O exceeded the ratios of Al/O, with a deposition temperature at 400 °C.

Within the visible range, the high transmittance of over 85% was achieved for all AZO films. Significantly, 2 wt% Al-doped ZnO film displayed the most pronounced photocatalytic effectiveness within the 475 nm to 700 nm wavelength range with high degradation reaction rate of 0.004 $\text{min}^{-1}$. In order to study the underlying relationship of AZO films with varied Al doping ratios during mist chemical vapor deposition process, the growth mechanism was revealed in this section.

### 3. Controlling the growth orientation and surface area of AZO films with different AZO seeds layer

We present a hybrid methodology combining the mist chemical vapor deposition with radio frequency magnetron sputtering to fabricate AZO films with adjustable growth orientation and crystallinity. Here is a breakdown of the proposed method:

1. Radio frequency magnetron sputtering for AZO seed layer deposition: We initiated the process by employing a radio frequency magnetron sputtering system to deposit a 300 nm-thick AZO film onto a glass substrate. Two different AZO targets were utilized for comparison: one with a 2 wt% aluminum (AZO-2wt%) and the other with 5 wt% aluminum (AZO-5wt%).

2. In addition, we utilized the as-deposited AZO films with different Al ratios of 2 wt% and 5wt% as distinct seed layers for the further deposition of 300 nm-thick AZO films using the mist chemical vapor deposition process.

The pivotal role of crystallinity in the AZO seeds layers was revealed after radio frequency magnetron sputtering process, as it influenced the growth direction of AZO films. After the mist chemical vapor deposition process, the obtained AZO films achieved the growth orientation in the (0001) crystal plane, corresponding to the under-deposited AZO seed layer. In particular, the low lattice mismatch between the obtained AZO films and the as-deposited AZO seed layer facilitated the improvement of a more columnar structure. The high photodegradation efficiency with high degradation rate of 0.0043 $min^{-1}$was achieved from the AZO film deposited on the AZO-5wt%.

## 4. Synthesis of ZnO nanorods by chemical bath deposition method

In this part, we applied the chemical bath deposition method to grow high vertically alignment ZnO nanorods on an AZO seeds layer. The structural, optical, and photocatalytic properties attributes of the obtained ZnO nanorods were conducted, with particular attention given to various growth reaction times.

It emerged that the growth direction of AZO seeds layer was notably influenced on the growth orientation of the ZnO nanorods. Interestingly, as the duration of the reaction is extended, there is an observed enhancement in the crystallinity of ZnO nanorods. It indicates that the length of the ZnO nanorod increases with the growth rate in the c-axis orientation. The most remarkable result was observed with ZnO nanorods grown for 5 hours, resulting in the longest nanorods with the highest crystallinity.

This study further highlighted that extending the growth reaction time from 1 hour to 5 hours had a direct impact on improving the crystallinity of the ZnO nanorods. Notably, the ZnO nanorods grown for 5 hours showed optimal alignment with the (0001) growth direction, a result attributed to their high absorption of $OH^-$ ions and subsequent generation of hydroxyl radicals, which is essential for degrading the methyl red dyes.

Furthermore, ZnO nanorods grown for 5 hours exhibited a large specific surface area compared to those grown under other reaction times. This development potentially transferred to a generation the greater number of reaction sites on the surface of ZnO nanorods, thereby attributing the photodegradation reaction rate. Impressively, optical transmittance was around 70% within the visible region. The high photocatalytic efficiency was achieved with ZnO nanorods grown for 5 hours, with a substantial photodegradation rate of 0.0051 $min^{-1}$. This comprehensive study offered insights into the photocatalytic mechanism sustaining ZnO nanorods.

## 5. Fabrication of AZO/ZnO core-shells nanorods by mist chemical vapor deposition method

In this section, we modified the AZO core-shells structure on the well-aligned ZnO nanorods by using mist chemical vapor deposition method. In order to evaluate the AZO coating effects on the ZnO nanorods, the coating times were set up for 5, 10, 15, 20 minutes during mist chemical vapor deposition process. The structural, optical, and photocatalytic properties were investigated.

It was clearly observed that the formation of uniform ZnO nanorods exhibiting a hexagonal structure on the AZO substrate before the coating process. Remarkably, as the coating time was extended to 20 minutes, the entire surface of ZnO nanorods became entirely covered by AZO particles. Moreover, it was observed that the ZnO nanorods exhibited a vertical growth orientation on the AZO substrates before the coating process. After the coating time was increased from 5 minutes to 20 minutes, the uniform distribution of AZO particle layers on the surface of ZnO nanorods was observed.

Prior to the AZO coating, the as-deposited ZnO nanorods exhibited a growth direction along the (002) crystal plane, which was identical to the growth direction of the underlying AZO substrate. Upon initiation of the AZO coating, the resulting AZO/ZnO core-shell nanorods maintained a single dominant (002) peak and it was observed that the crystallinity improved as

the coating time increased to 20 minutes. The highest crystallinity was achieved from the AZO/ZnO core-shell nanorods with AZO coating of 20 minutes.

The high transmittance of around 60% was observed in obtained all AZO/ZnO core-shells nanorods. In the photodegradation process, the degradation efficiency of AZO/ZnO core-shells nanorods was significantly improved when the AZO coating time was increased. The high degradation rate of 0.0053 $\text{min}^{-1}$ with the high degradation efficiency was achieved from the AZO/ZnO core-shells nanorods with AZO coating of 20 minutes.

# Acknowledgement

First, I would like to express my sincere gratitude to my supervisor, Prof. Dr. Chaoyang Li. She allowed me an excellent opportunity to pursue a Ph.D. degree, a milestone in my life. From the moment I joined the KUT until now, she treated me like a family. When I was going through a difficult time due to personal trauma for half a year, she helped me understand and support my life. I will always be proud to have been her student in my whole life.

Another person to extend my appreciation is my co-supervisor, Ass. Prof. Alexandra Apostoluk. Although she could not join my pre-defense due to the pandemic, she made a significant effort to be present in person for my final defense and shared her knowledge. Even within the limited time of our in-person interactions, I learned a lot of valuable experiences from her.

I would like to thank another co-supervisor, Prof. Hiroshi Furuta, and committee members, Prof. Hisao Makino, and Prof. Toshiyuki Kawaharamura for their helpful comments and suggestions in my research. Their assistance in conducting experiments and analyzing data greatly contributes to have good efficiency of my research.

I would also like to express my gratitude to all my laboratory members, specially, Mr. Tomoya Ikuta, a master student in my laboratory. His invaluable assistance in conducting my experiments, coupled with our collaborative efforts in data analysis, have left an indelible mark on my research journey. His support will always be remembered with deep appreciation.

I would like to extend my heartfelt thanks to the staffs of the International Relations Center from KUT. Their continuous support has not only on my research life but has also significantly facilitated my daily life activities. Additionally, their guidance and consultations on a wide array of matters have been hugely valuable. Through their arrangements, I had the pleasure of sightseeing new places and gaining insights into various aspects of Japanese cultures. Their contributions to my academic and personal experience have been truly invaluable.

Lastly, I want to express my deepest gratitude to my three sisters. Despite the absence of our parents and the numerous challenges we faced, their unwavering support allowed me to pursue my education without hindrance. Their kindness and sacrifices have been the cornerstone of my journey, and I owe my achievements to their selflessness. I will remain eternally grateful to my sisters for the rest of my life.

## Lists of figures

# List of Tables

## Contents

## Chapter 1 Introduction

## Chapter 2 Synthesis equipment and characterization devices

## Chapter 3 Synthesis and characterization of AZO films with varied Al doping ratios using mist CVD method

**Chapter 4 Influence of AZO seeds layer on the control of growth and crystallinity of AZO Films**

**Chapter 5 Synthesis and characterization of ZnO nanorods and AZO/ZnO core-shell nanorods by mist CVD method**

# Chapter 1

# Introduction

## 1.1. The literature review of photocatalysis

Water is an invaluable resource that is essential to human and environmental health. However, the increasing demand for clean water due to industrialization, urbanization, and climate change has resulted in a global water crisis [1]. The lack of clean water can spread several diseases, such as typhoid, dysentery, hepatitis A, and diarrhea. Unfortunately, industrial activities and human negligence have contaminated many freshwater sources worldwide, necessitating purification [2-4]. In the last decades, industrialization has brought rapid development to our society but also posed a significant challenge to reduce pollution and fossil fuel consumption [5,6]. One of the challenges is the treatment of wastewater from the textile industries, which uses many organic dyes. Approximately $7 \times 10^{-5}$ tons of organic dyes are released globally every year, and more than 16% of them are discharged into the wastewater during production and processing [7-9]. These chemicals have a high potential for toxicity and damage to the living organism, and their intermediates can generate potentially carcinogenic or mutagenic compounds through reductive processes unless inhibited. Among the various hazardous dyes involved in wastewater, methyl red (MR) belongs to the category of Azo dyes, which are notorious for their harmful and toxic characteristics. These dyes, including MR, have been classified as hazardous substances due to their potential to induce irritation of eyes and serious risks to both the skin and the digestive system. Ingestion or inhalation of these dyes can lead to adverse health effects. It is imperative to handle Azo dyes with great caution and adhere to proper safety protocols to mitigate the associated health hazards [10-12]. MR dyes have the potential to induce elevated body temperature, harm the kidneys, and lead to spasms, given their strong ability to dissolve in water and infiltrate the human body via the food chain. Indeed, developing an effective degradation method for MR dyes utilizing metal oxide semiconductors holds significant promise in addressing environmental pollution concerns. By harnessing the photocatalytic properties of semiconductors metal oxides, it becomes possible to efficiently degrade MR and mitigate its potential impact as an environmental pollutant. This approach offers a sustainable solution for treating MR-contaminated water or wastewater, reducing the risk of releasing harmful compounds into the environment and contributing to a cleaner and safer ecosystem. Removing these MR dyes from wastewater is a severe issue, and developing an environmentally friendly and cost-effective method is challenging for all researchers. Dye degradation is a degradation process that involves the catalytic activity of semiconductor materials under photon irradiation [13]. However, the low separation of the electron-hole pairs in the highly stable semiconductor metal-oxide can weaken the practical applications of this attractive photocatalytic technique [14-18].

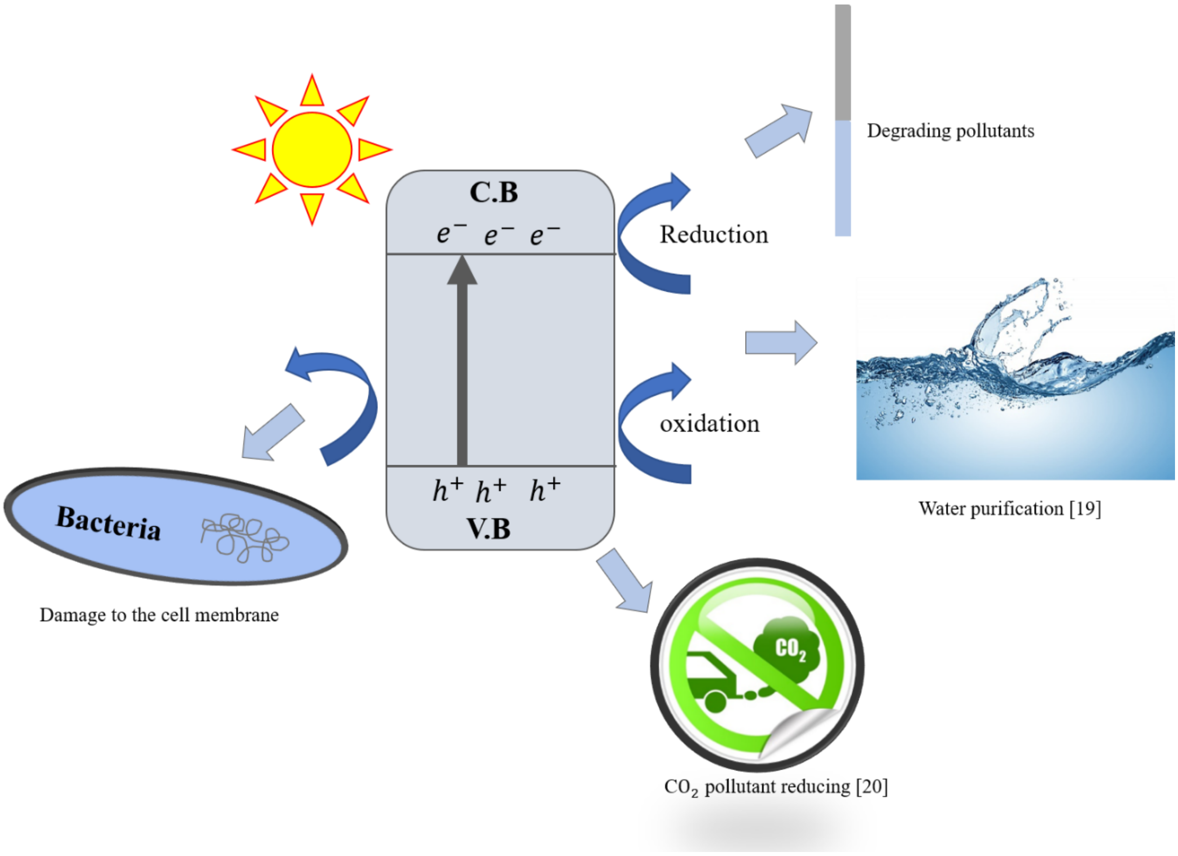

Fig. 1.1 Photocatalytic process and its application.

### 1.1.1 Semiconductor metal-oxide based photocatalysis

During the photocatalytic process, semiconductors metal-oxide with nanostructured materials can produce photogenerated charge carriers and then generate active oxygen species when exposed to a suitable light spectrum such as ultraviolet (UV) or visible (VIS) light [19]. Photocatalysis involves modifying a chemical reaction rate due to the presence of a photocatalyst, typically a semiconductor material when it is exposed to a light source. This light source can include UV light, VIS light, a combination of both UV and VIS, or even solar radiation. The interaction between the photocatalyst and light initiates a series of photochemical reactions that can lead to the degradation or transformation of pollutants, contaminants, or organic substances present in the environment. This process has gained significant attention for its potential applications in environmental remediation, water purification, and air treatment due to its ability to harness solar energy for catalytic reactions that contribute to reducing pollution and promoting sustainability [20-23]. The photocatalytic system requires certain unique features, such as the optimal band gap, high surface area, chemical stability, and reusability. Several kinds of photocatalyst metal oxides, including zinc oxide (ZnO), titanium dioxide ($TiO_2$), copper oxide, silver oxide, and iron (III) oxide have been applied in wastewater treatment [24,25]. The use of various semiconductor photocatalytic nanomaterials as catalysts has been investigated extensively, and their efficiency in various light sources for MR dye degradation is described in Table 1.1.

Table 1.1. Different semiconductor photocatalyst materials for MR dye degradation

| **Photocatalytic material** | **Synthesis method** | **Light sources** | **Reaction time (min)** | **Degradation efficiency (%)** | **Ref.** |
|---|---|---|---|---|---|
| ZnO | Sol-gel, RF sputtering, CVD, Spray pyrolysis | UV lamp | 120 | 95 | [26] |
| $TiO_2$ | Sol-gel, MOCVD | UV lamp | 60 | 94 | [27] |
| $SnO_2$ | Precipitation, RF sputtering, Sol-gel | UV lamp | 120 | 90 | [28] |
| AgO | Precipitation, Sol-gel, Laser ablation | UV lamp | 70 | 87 | [29] |
| MgO | Solvothermal | UV lamp | 120 | 81 | [30] |
| ZnO/GNc Composite | Chemical Precipitation | Visible light | 35 | 85 | [31] |
| $Ag/TiO_2$ | γ-Irradiation | Solar light | 45 | 84 | [32] |
| $Fe_2O_3/Cu_2O$ | Hydrothermal | 150 W Xe lamp | 120 | 87 | [33] |
| CuO | Co-precipitation | 300 W Xe lamp | 180 | 77 | [34] |
| $Al_2O_3$ | Sol-gel | 11 W UV lamp | 90 | 79 | [35] |
| $BiFeO_3$ | Sol-gel | UV lamp | 180 | 79 | [36] |

Among various photocatalyst materials, ZnO and $TiO_2$ are the most widely used photocatalysts for the degradation of antibiotics in water due to their non-toxicity, chemical stability, and low cost. The photocatalytic performances of ZnO and $TiO_2$ are anticipated to be comparable due to their same band gap energy [37]. However, the performances of photocatalyst metal oxide are dependent on the different morphology, charge-transfer process, and surface reactions with dye molecules. Absolutely, ZnO indeed possesses specific intrinsic characteristics that make it a promising and effective photocatalyst, positioning it as an alternative metal oxide to $TiO_2$. Notably, ZnO exhibits a high electron mobility, surpassing that of $TiO_2$ by a significant factor of 10 to 100 times. The high electron mobility is accompanied by a higher quantum yield, further enhancing its potential as a photocatalyst [38,39]. Moreover, ZnO is naturally abundant and has been widely used as photocatalyst materials for several decades due to their biocompatibility, remarkable stability in various conditions, and ability to produce electrons and holes when excited with sufficient energy. Due to its direct and wide band-gap energy near the UV spectral region, powerful oxidation ability, excellent photocatalytic property, and high free-exciton binding energy (60 meV), ZnO has attracted attention for environmental applications [40].

## 1.2. ZnO based photocatalytic properties

ZnO represents a notable semiconductor material classified within the II-VI category of compound oxides. Since its initial exploration in 1912, ZnO has garnered considerable attention as a compound semiconductor among semiconductor materials [41]. ZnO exhibits three distinct crystalline structures: the hexagonal wurtzite, the cubic zinc blende, and the rock salt. The primary crystalline of ZnO is the wurtzite structure, characterized by a hexagonal unit cell and categorized under the space group p6mc. In this structure, $Zn^{2+}$ and $O^{2-}$ ions establish two interpenetrating sublattices that exhibit tetrahedral coordination [42,43]. The ZnO crystal exhibits various common surface orientations, especially the polar facets of Zn-terminated (0001) and O-terminated $(000\bar{1})$, as well as non-polar $(10\bar{1}0)$ and $(11\bar{2}0)$ facets. Among these orientations, the (0001) orientation emerges as the most thermodynamically favorable, as indicated by its small Gibbs free energy, thereby serving as the preferred orientation for the growth of wurtzite hexagonal ZnO structures [44,45].

Moreover, ZnO emerges as an environmentally friendly material, exhibiting biocompatibility that is well-suited for everyday applications with minimal side effects on human health and the environment [46]. The photocatalytic behavior of ZnO exhibits a sequence of processes, excitation, diffusion, and the induction of photo-generated charge carriers. When exposed to light with energy exceeding its band gap, ZnO experiences the generation of charge carriers, wherein electrons get excited to the conduction band, leaving holes in the valence band behind.

Consequently, the excited electrons within the valence band undergo a transition to the conduction band, giving rise to electron-hole pairs. A visual representation of the ZnO photocatalytic mechanism is provided in Fig. 1.2. Particularly, these photo-induced electrons and holes undergo migration to the surface of the ZnO, wherein they take place in oxidation and reduction reactions with oxygen and water molecules. The underlying reaction mechanism of ZnO can be delineated as follows:

$$e^- + O_2 \rightarrow .O_2^- \quad (1)$$

$$h^+ + H_2O \rightarrow OH^- + H^+ \quad (2)$$

$$.O_2^- + OH^- \rightarrow {}^\circ HO_2 \quad (3)$$

$$^\circ HO_2 + H^+ \rightarrow H_2O_2 \quad (4)$$

$$H_2O_2 + e^- \rightarrow OH^- + {}^\circ OH \quad (5)$$

According to Eq (1-5), The photo-excited electrons ($e^-$) can migrate across the surface of ZnO, where they engage in oxidation processes with atmospheric $O_2$, producing superoxide radicals ($.O_2^-$). In parallel, the positively charged holes ($h^+$) initiate reactions with water molecules ($H_2O$), leading to the generation of hydroxide ions ($OH^-$). The produced superoxide radicals ($.O_2^-$) undergo a continuous reaction with dissociated hydrogen ions originating from water molecules, resulting in the formation of hydrogen peroxide ($H_2O_2$). This subsequently leads to the generation of hydroxyl radicals ($^\circ OH$). Remarkably, ZnO characterized by high crystallinity facilitates an efficient occurrence of direct band transitions, thereby increasing the rate of electron-hole pair generation and, consequently happening, the formation of superoxide radicals ($.O_2^-$) and hydroxyl radicals ($^\circ OH$).

The utilization of ZnO nanoparticles in powder form is accompanied by certain limitations inherent to repeated photocatalytic processes [47]. A strategy to overcome these limitations involves the utilization of thin films or nanostructures deposited onto substrates [48,49]. In its nano-structural form, ZnO presents significant potential for photocatalytic applications, such as physical and chemical stability, less toxicity, abundance in nature, different fabrication methodology, and the availability of varied nanostructure morphologies [50]. Incorporating ZnO nanostructures has generated a distinct enhancement in photocatalytic efficiency, primarily attributed to the large surface area-to-volume ratio that enhances high efficiency in photocatalytic applications.

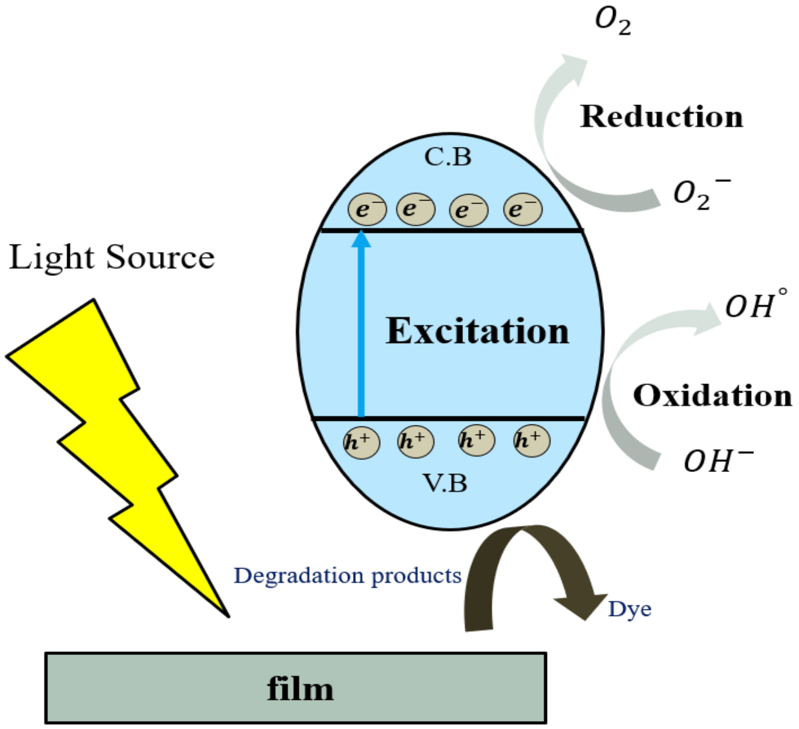

Fig. 1.2. Sketch of ZnO photocatalytic principle

### 1.2.1 Remained issues for ZnO in dye degradation from water pollutants

Although ZnO possesses a range of distinctive photocatalytic characteristics, it also exhibits certain limitations that hinder its effectiveness in photodegradation. The primary issues related to the usage application of ZnO from its unique tendency to exclusively absorb UV light, a component constituting only a small portion of the broader solar spectrum. It also requires expensive external sources of UV light to excite the bandgap of ZnO and generate electron-hole pairs [51,52]. Moreover, the high recombination rate in ZnO prevents the migration of pairs of electron-holes to the surface and thus reduces the photodegradation efficiency [53]. Furthermore, the fast recombination rate of ZnO hinders efficient movement of charge carriers toward the surface of a material, thereby reducing the overall photodegradation efficiency during the photodegradation process [54].

Hence, several strategies have been explored to enhance the capacity for absorbing visible light, including several modifications like metal and non-metal doping, dye sensitization, and synergistic combinations with other semiconductor materials. One particularly promising method involves the Al incorporation into ZnO, as shown in the Fig. 1.3, which could reduce the recombination rate within ZnO and consequently enhance photocatalytic performance [55,56]. Furthermore, the practical extension of light absorption into the visible spectrum, alongside the enhancement of electronic characteristics, can be achieved through surface modifications of ZnO by integration with other semiconductor materials, noble metals, or graphene, formation of innovative hybrid structures which consequently enhances the photocatalytic activities [57-59]. The formation of defects within ZnO, coupled with additional photocatalyst materials, is presumed to contribute to its visible light photocatalytic potential. Notably, ZnO heterostructures have found widespread application in the high degradation of diverse organic dyes under UV and visible light irradiation. However, the activity of these heterostructures in catalyzing dye degradation in the absence of light remains unexplored. This study focuses on the mechanism of dye degradation in ZnO under light irradiation.

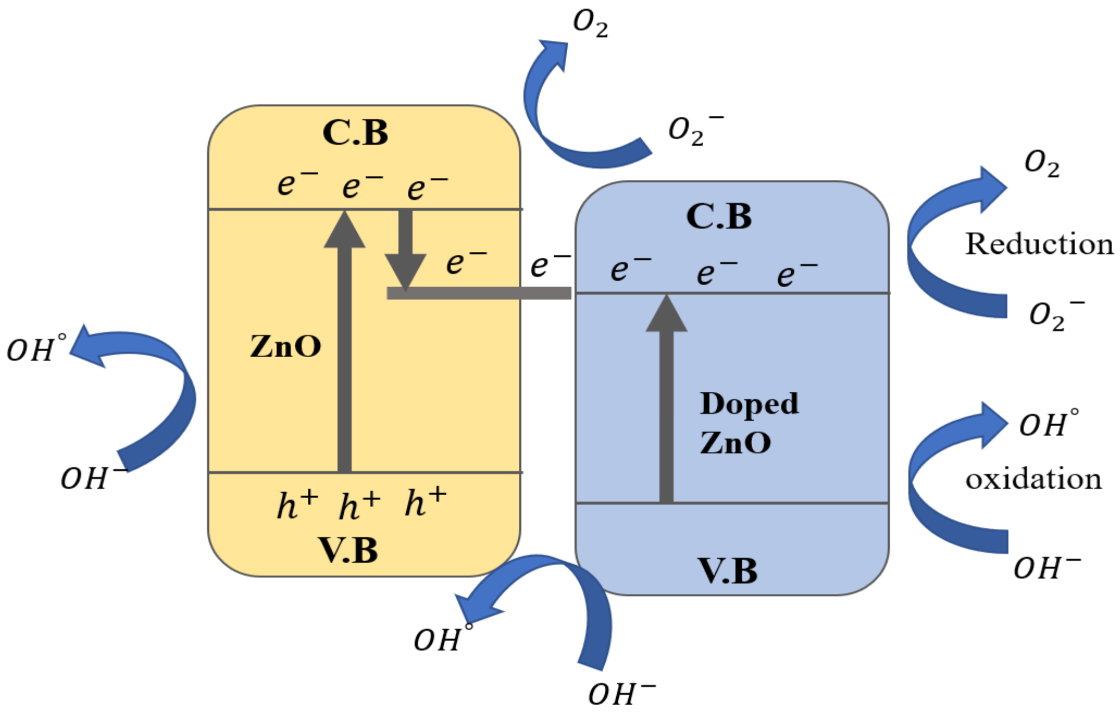

Fig. 1.3. Minimizing the recombination rate of charge carriers by doping method

## 1.3 Fabrication methods of ZnO nanostructures

The controlled synthesis of ZnO nanostructures, with precise control over their size and shape, is a compelling pursuit for researchers. ZnO possesses a diverse array of nanostructure forms, ranging from one-dimensional (1D) configurations to three-dimensional (3D) shapes. The 1D category encompasses a spectrum of shapes, including needles, nanorods, helices, rings, springs, ribbons, tubes, belts, combs, and wires, while the 2D structures comprise nanosheets and nanoplates. The 3D classification involves flowers, coniferous formations, snowflakes, urchin-like arrangements, and dandelions [60-64].

To date, various fabrication methods have been utilized for the synthesis of ZnO nanostructures, involving chemical bath deposition (CBD), vapor-liquid-solid (VLS) processes, metal-organic chemical vapor deposition (MO-CVD), chemical vapor deposition (CVD), thermal evaporation techniques, and metal-organic vapor-phase epitaxy, and etc. [65-69].

Several methods have been developed to synthesize different ZnO nanostructures. However, numerous challenges remain for industrial applications, such as low reproducibility, difficulty in controlling the alignment, complex fabrication processes, high cost, low stability, and environmental pollution. Consequently, a novel method is required to fabricate controlled vertical well-aligned ZnO nanostructures. Our research group has extensive experience in fabricating high-quality ZnO thin film using a radio frequency (RF) magnetron sputtering process [70]. We have already investigated the relationship between the deposition parameters, the substrates, and the properties of obtained films. Recent advancements within our group have successfully fabricated well-aligned hexagonal-cone ZnO nanostructures on as-deposited AZO film by using the CBD method, which was distinct from other existing techniques of ZnO nanostructures synthesis [71]. Nevertheless, using the current synthesis method, there still needs to be a strict issue with fabricating doped ZnO nanostructures with good uniformity, large surface area, and high crystallinity. In order to fabricate doped ZnO nanostructures with those properties, it is essential to innovate a pioneering fabrication method.

## 1.4 Purposes and outlines of thesis

The focal point of this doctoral research is on the fabrication of thin films and nanostructures related to ZnO, specifically emphasizing their properties for photocatalytic applications. The ongoing investigation is directed toward enhancing the morphology, surface area, crystallinity, and overall photocatalytic performance of ZnO-related thin films and nanostructures. This research introduces a series of academic innovations and original contributions to enhance photocatalytic efficiency. ZnO nanostructures intended for photocatalytic applications must satisfy three primary criteria:

(a) Low recombination rate of electron-hole pairs
(b) Large surface area to absorb MR dye molecules
(c) High crystallinity along (0001) crystal plane to generate more hydroxy radicals

In my research, I have proposed several innovative approaches to address these requirements:

1. In order to minimize the high recombination rate of charge carriers, Al was successfully doped to ZnO using mist CVD method. The growth mechanism of obtained AZO films with controllable Al doping ratios by mist CVD process was investigated. (one paper published)
2. The crystallinity of deposited AZO films was controlled by using AZO seeds layer by mist CVD process. The observed lower lattice mismatch between the AZO films and the AZO seeds layer can be attributed to the significant growth of a high columnar structure and high crystallinity along (0001) crystal plane. (one paper published)
3. Large surface area was achieved by growing the ZnO nanostructures for 5 hours using the CBD method (one paper published) and modifying the AZO core-shells on ZnO nanorods to hinder the recombination rate of electron-hole pairs.

The primary work of the thesis will be described the fabrication of ZnO-based thin films with different thicknesses, different Al doping ratios, different AZO seeds layers, fabrication of ZnO nanorods with different growth reaction times, and fabrication of AZO/ZnO core-shells nanorods with different coating times.

**Chapter 1**: In this chapter, a detailed exploration of the general knowledge surrounding ZnO material and ZnO-related photocatalysis was provided. Historical evaluation of ZnO and its applications across various fields were extensively discussed, emphasizing its potential in addressing environmental concerns. The primary objectives of the thesis were clearly outlined, aiming to advance our understanding of ZnO photocatalytic capabilities and its potential for pollutant degradation. Furthermore, the chapter established the overall structure of the thesis, guiding the reader through the subsequent chapters and the logical progression of the research.

**Chapter 2:** This chapter offered a concise comprehensive overview of the underlying principles about the fabrication and characterization processes, including the necessary characterization methods and equipment. The fundamental mechanisms behind the fabrication techniques were outlined, and the crucial role of various characterization tools in assessing material properties was highlighted. By providing a clear foundation of the methodologies used, this chapter helped the reader to understand the essential knowledge required to comprehend the subsequent experimental work.

**Chapter 3**: In this pivotal chapter, the focus shifted to the detailed investigation of fabrication of ZnO and AZO films—the deposition process of the films, varying in aluminum doping ratios. The structural, optical, and photocatalytic properties on the properties of AZO films were characterized. Special emphasis was placed on understanding the photodegrading properties, and the influence of Al doping ratios on photocatalytic efficiency was thoroughly examined. By addressing both fabrication and characterization aspects, this chapter arranged the foundation for subsequent discussions and conclusions.

**Chapter 4**: The growth and crystallinity of AZO films were controlled by using the AZO seeds layer by mist CVD method and photocatalytic properties of obtained samples were examined in detail.

**Chapter 5**: Synthesis of well-aligned ZnO nanorods with different reaction times and AZO/ZnO core-shells nanorods with different AZO coating times using the hybrid synthesis methods of CBD and mist CVD method. The photocatalytic properties were investigated as well.

**Chapter 6**: The primary works of this thesis have been summarized.

## 1.5 References

[1] A. Mojiri, M. J. K. Bashir. Water. 14 (2022) 448.

[2] R. Lin, Y. Li, T. Yong, W. Cao, J. Wu, Y. Shen. A review. J. Environ. Manag. 306 (2022) 114460.

[3] A. Mojiri, J. Zhou, M. Vakili, H. Van Le. J. Contam. Hydrol. 235 (2020) 103736.

[4] M.B. Ahmed, J. L. Zhou, H.H. Ngo, W. Guo. Sci. Total Environ. 532 (2015) 112.

[5] A.F. Kohan, G. Ceder, D. Morgan, and C.G. Van de Walle. Phys. Rev. B, 61 (2000) 15019.

[6] X.L. Guo, J.H. Choi, H. Tabata, and T. Kawai. Jpn. J. Appl. Phys. 40 (2001) L177.

[7] D.K. Hwang, S.H. Kang, J.H. Lim, E.J. Yang, J.Y. Oh, J.H. Yang, and S.J. Park. Appl. Phys. Lett. 86 (2005) 222101.

[8] J.F. Wager. Science, 300 (2003) 1245.

[9] S.H. Park, C.W. Ahn, S. Nahm, and J.S. Song. Jpn. J. Appl. Phys. 43 (2004) L1072.

[10] J.H. He, C.L. Hsin, J. Liu, L.J. Chen, and Z.L. Wang. Adv. Mater. 19 (2007) 781.

[11] L. Vayssieres. Adv. Mater. 15 (2003) 464.

[12] C.Y. Jiang, X.W. Sun, G.Q. Lo, D.L. Kwong, and J.X. Wang. Appl. Phys. Lett. 90 (2007) 263501.

[13] J. Bardeen, and W.H. Brattain. Phys. Rev. 74 (1948) 230.

[14] A.S. Kamble, K. Chung, B.B. Sinha, M.G. Gil, V. Burungale, C.J. Park, J.H. Kim, and P.S. Patil. Electrochim. Acta, 149 (2014) 386.

[15] O. Dulub, L.A. Boatner, and U. Diebold. Surf. Sci. 519 (2002) 201.

[16] D.R. Lide (Ed.). CRC Handbook of Chemistry and Physics, 73rd Edition, CRC Press, New York, (1992).

[17] Z.W. Pan, Z.R. Dai, and Z.L. Wang. Science, 291 (2001) 1947.

[18] X. Pan, X. Liu, A. Bermak, and Z. Fan. ACS Nano, 7 (2013) 9318.

[19] S.E. Ahn, J.L. Soo, H. Kim, S. Kim, B.H. Kang, K.H. Kim, and G.T. Kim. Appl. Phys. Lett. 84 (2004) 5022.

[20] T. Okada, B.H. Agung, and Y. Nakata. Appl. Phys. A, 79 (2004) 1417.

[21] X. Liu, X. Wu, H. Cao, and R.P.H. Chang. J. Appl. Phys. 95 (2004) 3141.

[22] A. Yengantiwar, R. Sharma, O. Game, and A. Banpurkar, Curr. Appl. Phys. 11 (2011) S113.

[23] S. Chu, D. Li, P.C. Chang, and J.G. Lu. Nanoscale Res. Lett. 6 (2011) 1.

[24] I. Gonzalez-Valls, Y. Yu, B. Ballesteros, J. Oro, and M. Lira-Cantu. J. Power Sources, 196 (2011) 6609.

[25] S. Kahraman, H.M. Çakmak, S. Çetinkaya, H.A. Çetinkara, and H.S. Güder. Internat. J. Mater. Res. 104 (2013) 799.

[26] P.K. Baviskar, P.R. Nikam, S.S. Gargote, A. Ennaoui, and B.R. Sankapal. J. Am. Ceram. 551 (2013) 233.

[27] P.P. Das, S. Mukhopadhyay, S.A. Agarkar, A. Jana, and P.S. Devi. Solid State Sci. 48 (2015) 237.

[28] S. Ameen, M.S. Akhtar, M. Song, and H.S. Shin. ACS Appl. Mater. Interfaces, 4 (2012) 4405.

[29] N. Islavath, E. Ramasamy, D. Das, and S.V. Joshi. Ceram. Int. 41 (2015) 4118.

[30] A. Tubtimtae, and M.W. Lee, Superlattice. Microst. 52 (2012) 987.

[31] Q. Hu, Y. Li, F. Huang, Z. Zhang, K. Ding, M. Wei, and Z. Lin, Sci. Rep. 5 (2015) 11499.

[32] A.A. Rani, and S. Ernest, J. Mater. Sci. Mater. El., 26 (2015) 762.

[33] C. Li, M. Furuta, T. Matsuda, T. Hiramatsu, H. Furuta, and T. Hirao. Thin Solid Films, 517 (2009) 3265.

[34] J. Nomoto, M. Konagai, K. Okada, T. Ito, T. Miyata, and T. Minami. Thin Solid Films, 518, (2010) 2937.

[35] D. Wang, Z. Li, T. Kawaharamura, M. Furuta, T. Narusawa, and C. Li. Phys. Status Sidi C, 9 (2012) 194.

[36] X. Li, C. Li, S. Hou, A. Hatta, J. Yu, and N. Jiang. Compos. Part B: Eng. 74 (2015) 147.

[37] X. Li, C. Li, T. Kawaharamura, D. Wang, N. Nitta, M. Furuta, H. Hiroshi, and A. Hatta. Nanosci. Nanotech. Lett. 6 (2014) 174.

[38] J. Musil, and J. Vlček. Mater. Chem. Phys. 54 (1998) 116.

[39] P.F. Fewster. Rep. Prog. Phys. 59 (1996) 1339.

[40] F. Jensen, Introduction to Computational Chemistry. John Wiley & Sons, New York, 1999.

[41] D.R. Hamarm, M. Schhter, and C. Chiang. Phys. Rev. Lett. 43 (1979) 1494.

[42] J. Gong, J. Liang, and K. Sumathy. Renew. Sustainable Energy Rev. 16 (2012) 5848.

[43] Z. You, and G. Hua. J. Alloy Comp. 530 (2012) 11.

[44] X.M. Duan, C. Stampfl, M.M. Bilek, and D.R. McKenzie. Phys. Rev. B, 79 (2009) 235208.

[45] C. Li, T. Kawaharamura, T. Matsuda, H. Furuta, T. Hiramatsu, M. Furuta, and T. Hirao. Appl. Phys. Exp. 2 (2009) 091601.

[46] M.N. Ashfold, R.P. Doherty, N.G. Ndifor-Angwafor, D.J. Riley, and Y. Sun. Thin Solid Films, 515 (2007) 8679.

[47] Z.L. Wang. J. Phys. Condens. Mat. 16 (2004) R829.

[48] D. Che, A.K Ray. Chem. Eng. Sci. 56 (2001) 1561.

[49] A. Mills,; S.L. Lehunte. A Chem. 108 (1997) 1.

[50]. H. Gerischer. Soc. 1966, 113, 1174.

[51]. A. Mills, C. O'Rourke, K. Moore. J. Photochem. Photobiol. 310 (2015 66.

[52]. M. Kanemoto, T. Shiragami, C. Pac, S. Yanagida. J. Phys. Chem. 96 (1992) 3521.

[53]. P. Franco, O. Sacco, I. De Marco, V. Vaiano. 9 (2019) 346.

[54]. K. Vanheusden, W.L. Warren, C.H. Seager, K. Tallant, T.A. Voigt. J. Appl. Phys. 79 (1996) 7983.

[55]. M. Ferroni, C. Baratto, G. Faglia, E. Comini, G. Sberveglieri. Cryst. Eng. Comm. 15 (2013) 7981.

[56]. Y.S. Seo, S.G. Oh. Korean J. Chem. Eng. 36 (2019) 2118.

[57]. D. Gaspar, L. Pereira, K. Gehrke, B. Galler, E. Fortunato, R. Martins. Sol. Energy Mater. Sol. Cells. 163 (2017) 255.

[58]. B.K. Meyer, H. Alves, D.M. Hofmann, W. Kriegseis, D. Forster, F. Bertram, J. Christen, A. Hoffmann, M. Straßburg, M. Dworzak. Phys. Status. Solidi. 241 (2004) 231.

[59]. S. Mukhopadhyay, P.P. Das, S. Maity, P. Ghosh, P.S. Devi. Appl. Catal. B Environ. 165 (2015) 128.

[60]. J. He, Y. Zhang, Y. Guo, G. Rhodes, J. Yeom, H. Li, W. Zhang. Environ. Int. 132 (2019) 105.

[61] C.B. Ong, L.Y. Ng, A.W. Mohammad. Renew. Sustain. Energy. Rev. 81 (2018) 536.

[62] M. Kanemoto, T. Shiragami, C. Pac, S. Yanagida, J. Phys. Chem. 96 (1992) 3521.

[63] X. Li, J. Wen, J. Low, Y. Fang, J. Yu. Sci. China. Mater. 57 (2014) 70.

[64] P. Franco, O. Sacco, I. De Marco, V. Vaiano. Catalysts. 9 (2019) 346.

[65] S. Fujita, H. Tanaka, S. Fujita, Appl. Phys. Lett., 86 (2005) 192911.

[66] Y.Z. Zhang, H. Li, T. Wang, E.Q. Xie, X.J. Pan. J. Alloys Compd., 472 (2009) 208

[67] K. Ito, J. Katayama, J. Tamaki, M. Matsuoka. J. Appl. Electrochem., 34 (2004) 687.

[68] H. Nanto, S. Takata, T. Minami. Jpn. J. Appl. Phys., 23 (1984) 280.

[69] X.L. Guo, H. Tabata, T. Kawai, J.H. Choi. Jpn. J. Appl. Phys., 40 (2001) 177.

[70] C. Li, M. Furuta, T. Matsuda, T. Hiramatsu, H. Furuta, T. Hirao. Research Lett. Mater. Sci. (2007) 26459.

[71] S. Hou, C. Li. Thin Solid Films, 605 (2016) 37.

# Chapter 2

# Synthesis equipment and characterization devices

## 2.1 Introduction

This chapter described a brief overview of the synthesis equipment performed for fabricating and characterizing the obtained thin films, nanorods, and core-shell nanostructures. Following the fabrication process of ZnO and AZO thin film, ZnO nanorods, and AZO/ZnO core-shells nanorods, a comprehensive evaluation of the morphological, structural, optical, and photocatalytic attributes was conducted using several characterization devices.

A scanning electron microscope (FE-SEM) was used to examine the surface morphologies of the films and nanostructures. An atomic force microscope (AFM) was utilized to measure the surface roughness and surface area measurements. The structural properties were analyzed employing an X-ray diffraction (XRD) system. A confocal Raman microscope was utilized to perform Raman spectroscopy. A spectrophotometer acquired to measure optical transmittance spectra and absorbance of obtained samples after photodegradation measurement. All characterization was measured at ambient room temperature. In the next two sections, each part of equipment was explained in detail.

## 2.2 Synthesis equipment

### 2.2.1 Mist chemical vapor deposition

An innovative mist CVD technique was used to fabricate the metal oxide thin films. The illustration of the conventional mist CVD setup is presented in Fig. 2.1. The mist CVD system comprises two primary components: the supply chamber and the reaction chamber. In the supply chamber, precursor materials are prepared through chemical solutions and transformed into mist droplets via ultrasonic transducer-driven atomization. Film deposition is accomplished through thermal decomposition and chemical reactions occurring in the vapor phase of these droplets. The mist droplets, transferred by carrier gas and dilution gas, proceed to the reactor.

The reaction chamber encompasses a fine channel reactor (FC reactor) above a heater. The FC reactor incorporates a narrow channel design to achieve a uniform thermal distribution [1,2]. Its initial section termed the mist mixing pool, promotes mist droplet collision. During this phase, pressures experience a rapid decrease due to the expansion of volume from a narrow to a large space, resulting in a uniform flow of mist into the fine channel with a height of 1 mm. After this transition, as mist droplets transfer from the mist mixing region to the FC, their kinetic and pressure diminish due to the smaller space. The mist droplets do not undergo immediate evaporation; instead, they generate a vapor phase covering the liquid phase. Upon reaching the heated substrate, these mist droplets acquire thermal energy through heat flux, resulting in vapor gas discharge into the surrounding environment. This prolonged evaporation is attributed to the Leidenfrost state [3]. The combined effect of gravitational forces and absorption ensures the effective transfer of mist droplets onto the substrate above the heating stage. This inventive reaction chamber design enables precise growth control, large-area deposition, cost-effectiveness, and operational simplicity. Hence, it stands as a promising advancement in material growth and deposition.

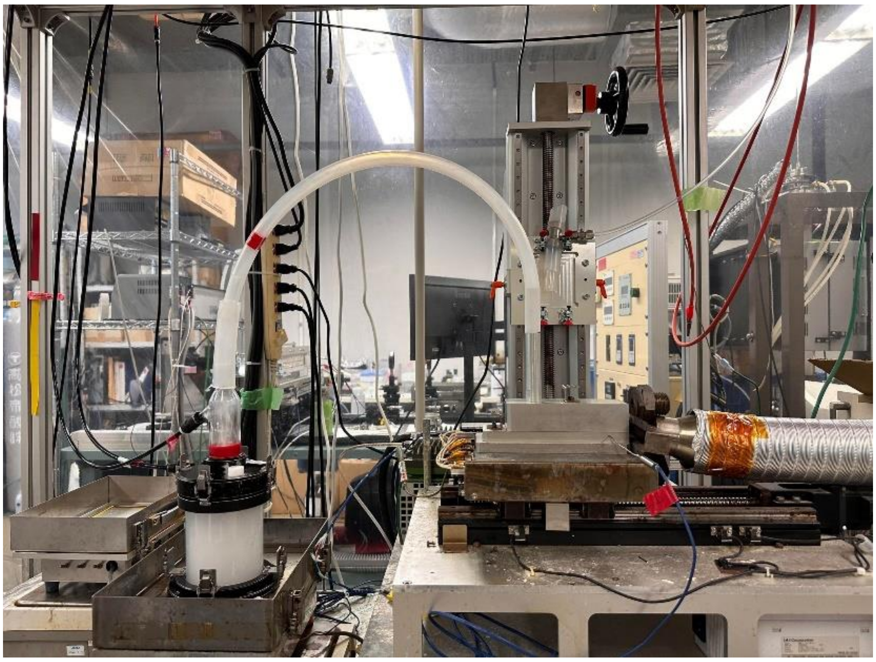

Fig 2.1 Mist chemical vapor deposition process

### 2.2.2 Chemical Bath Deposition

The CBD method stands out as a notably uncomplicated and cost-effective approach for depositing thin films and nanostructures, primarily attributed to its utilization of economical equipment and its capability for facilitating large-scale depositions [4]. The CBD technique includes separate components, as illustrated in Fig. 2.2, specifically the heating and reaction parts. The heating section serves the purpose of elevating the temperature of water or other solutions to a predetermined level for initiating reactions. Concurrently, the reaction zone is dedicated to the deposition of thin films or nanostructures, a process inherently governed by chemical reactions. The main benefit of CBD is that it needs only solution containers and substrate mounting devices.

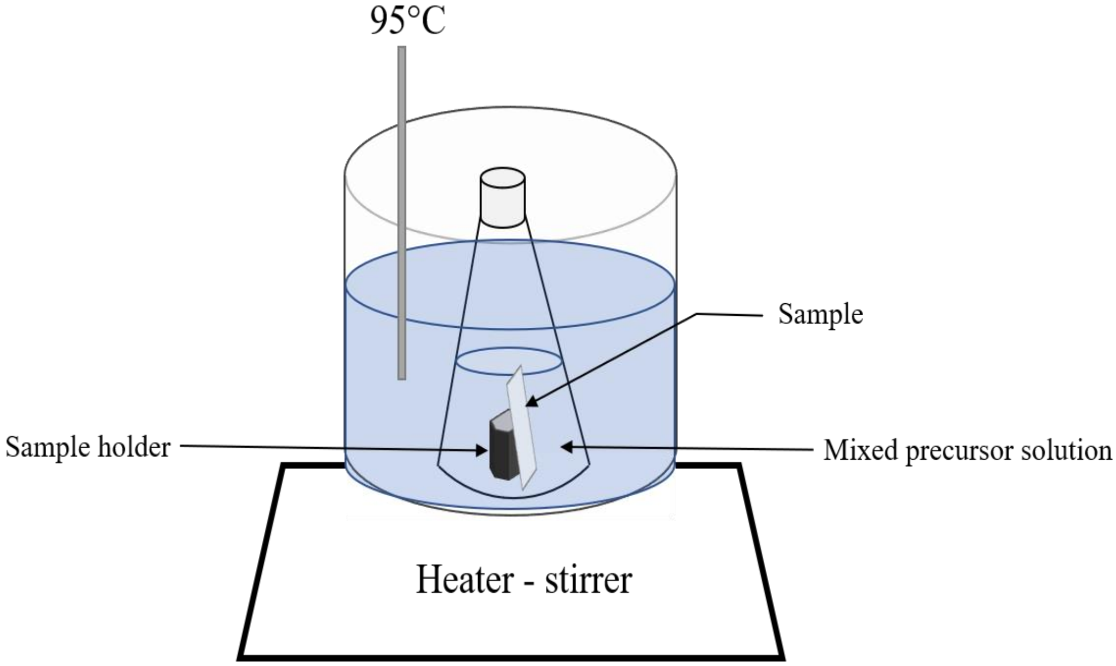

Fig. 2.2 Illustration of CBD process.

### 2.2.3 Radio frequency magnetron sputtering

Sputtering, a physical vapor deposition is a widely employed technique for depositing thin films onto various substrates [5]. A typical sputtering system comprises two main components: the target and the substrate. The sputtering system can be categorized by the different power supply: RF magnetron sputtering and direct current sputtering.

The RF magnetron sputtering process can be described as follows: Initially, inlet gas such as argon, was generated an ionic plasma, by applying a high voltage to the glow tube. The target placed on the cathode was bombarded by generated ions and induced the ejection of target atoms, facilitated by energy and momentum transfer. Subsequently, the sputtered atoms are deposited onto the substrate, positioned on the anode, as shown in Fig. 2.3.

The rapid oscillation of the electric field causes a reciprocal movement of the plasma between the substrate and target, thus upholding the potential difference between the cathode and anode, during the sputtering process [6]. This unique characteristic allows RF sputtering deposition of insulating materials and semiconductors.

On the other hand, the magnetron effect is the magnetic field orientation parallel to the cathode surface. This enhanced plasma confinement results in high plasma density, leading to a more substantial ejection of target atoms.

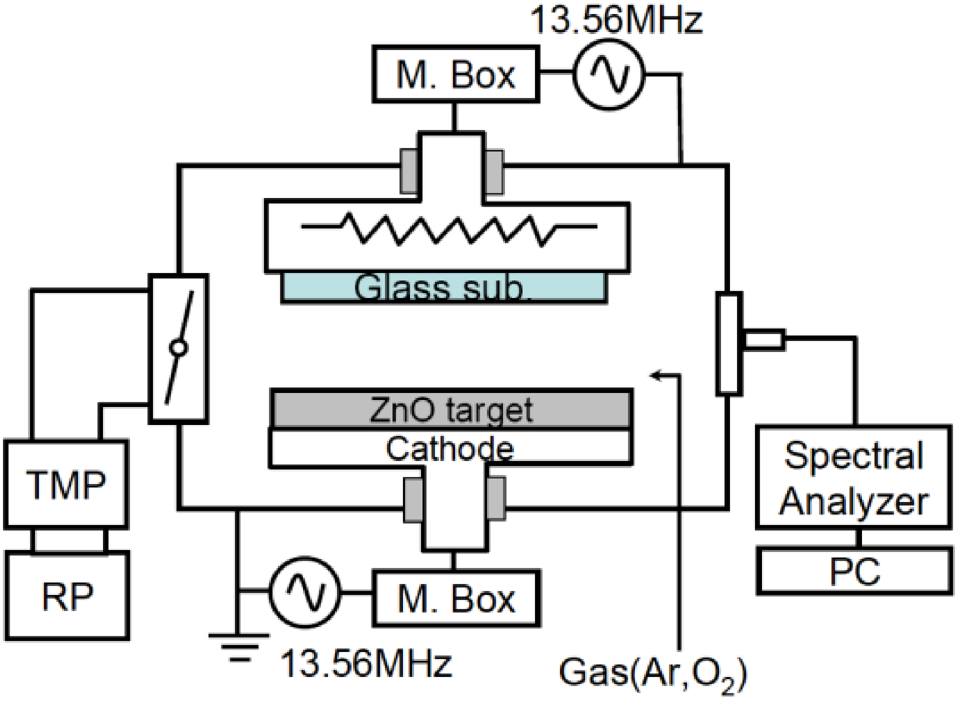

Fig. 2.3. Illustration of RF magnetron sputtering process.

## 2.2.4 Photocatalytic degradation process

Photodegradation entails a photo-activated chemical process that occurs upon light illumination onto the surface of a photocatalytic material positioned within a dye solution. This interaction occurs as the material is submerged under the dye solution. Upon attaining a required energy level, the excitation process happens, initiating free radicals at the contact area of the material and dye molecules. The configuration of the photodegradation setup is outlined in Fig. 2.4, offering a schematic representation of the apparatus performed for the photodegradation process.

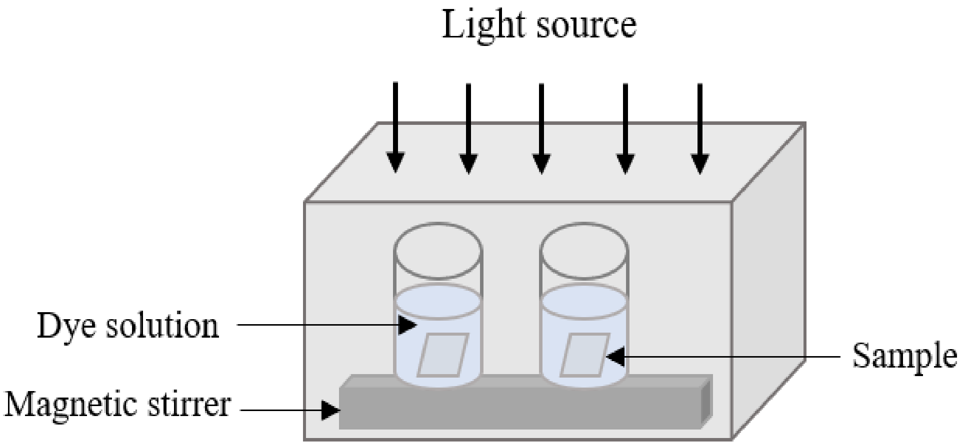

Fig. 2.4. Photodegradation measurement process

## 2.3 Characterization devices

### 2.3.1 Ellipsometry

Ellipsometry is a widely employed as a technique for measuring the thickness and refractive index of thin films deposited on a substrate. The underlying principle of this measurement revolves around the interaction of incident light waves, which are both reflected from and transmitted through the surface of the thin film, as depicted in Fig. 2.5. The reflection at a dielectric interface depends upon the polarization state of the incident light [7,8]. In contrast, the passage of light through a transparent layer imparts a phase alteration to the incoming wave, predicated upon the refractive index of the material.

Therefore, the film thickness and refractive index can be calculated when the refractive index of the film and substrate are known. In this thesis, the thin film thickness and refractive index was evaluated by employing the Cauchy model. The measurements were conducted across 28 distinct transparent regions, performed a spectroscopic ellipsometer (J.A. Woollam, W-VASE).

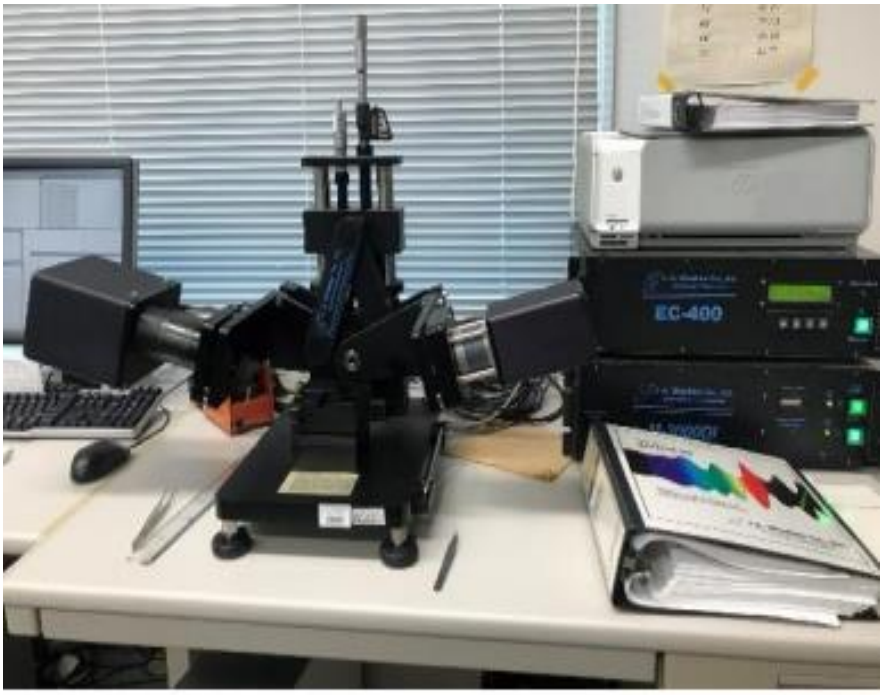

Fig. 2.5 Ellipsometry

### 2.3.2 Field emission scanning electron microscope

FE-SEM is one of the most versatile instruments available for analysis of the microstructure morphology characterization. Field emission source are used for liberation of the electrons and accelerated in a high electric field gradient. The primary electrons are focused and deflected by electron lenses under the high vacuum in order to provide a narrow scan beam, which exposes to the sample. Consequently, secondary electrons are emitted from sample. The electrical signal was created from the detector, which detects the secondary electrons from the sample. The digital image was obtained by the amplified electrical signal and transformed to a video scan-image. The process of FE-SEM is described in Fig. 2.6.

Energy Dispersive X-ray Spectroscopy (EDX) is a methodology employed for discerning the elemental composition of minute quantities, even on the scale of a cubic micron. This apparatus is integrated with the FE-SEM to enable the retrieval of elemental details. In the EDX, the atoms of the sample were ionized by electron beam, resulting in electrons were removed and produces the holes in the core shell. The electron from the outer shells fill the holes and generate the emission of the X-ray fluorescence lines. The EDX detector detects the emission of the X-rays. The measurement of composition in the films was using the point measurement mode, where five areas of the film and three points for each area were measured to reliably obtain the composition ratios in the film.

Fig. 2.6 FE-SEM

Fig. 2.7 AFM

### 2.3.3 Atomic force microscopy

AFM belongs to the category of scanning probe microscopes (SPMs). A fundamental characteristic shared by all SPM techniques is the utilization of an exceedingly sharp probe that is systematically moved across a surface of specimen to generate remarkably high-resolution images of the sample. In the case of the AFM, the probe directory interacts with the surface of the sample. The sample surface with high resolution was produced by probing the repulsive and attractive force in which exist between the probe and surface sample. The AFM (AFM; Pacific Nanotechnology, Nano-RJ) are shown in Fig. 2.7, with the closed contact mode was used for the measurement the film surface roughness and surface morphology.

### 2.3.4 X-ray diffraction

XRD stands as a pivotal technique for analyzing a diverse array of materials, spanning from fluids to powders and crystals. XRD finds extensive application in two primary domains: the fingerprint characterization of crystalline substances and the elucidation of their structural attributes. When a stream of X-rays interacts with a solitary crystal, multiple diffraction spots emerge. The spatial coordinates of these spots are dictated by the dimensions and configuration of the unit cell, as well as its inherent symmetry [9,10]. Meanwhile, the relative intensities of these spots are governed by the spatial arrangement of atoms within the crystal lattice. In this research, the structural properties of ZnO nanostructures were determined using an X-ray diffractometer (XRD; Rigaku, Smart Lab) with using $Cu - K\alpha$ tube ($\lambda = 0.154178$ nm) radiation. The applied XRD equipment was described in Fig. 2.8.

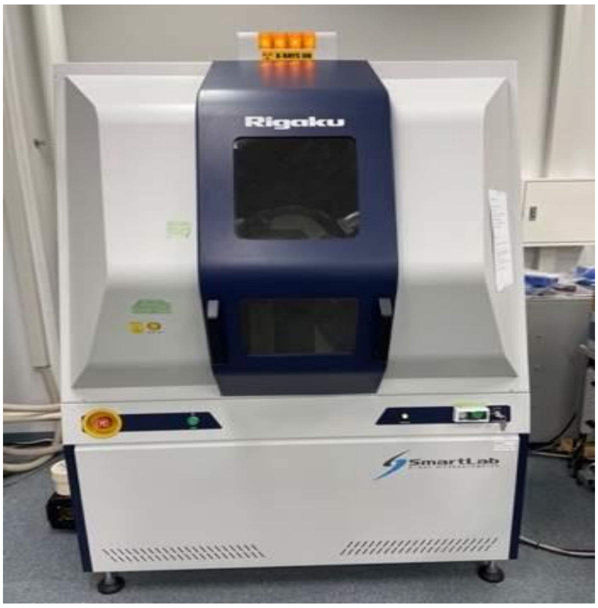

Fig. 2.8 The X-ray diffractometer

## 2.3.6 Raman spectroscopy

Raman spectroscopy is an analytical method used to study the vibrational and rotational modes of a system. A laser beam is employed to excite rotations of phonons in the materials, molecular vibrations that cause energy shifting and provide the vibrational modes present in that system. This technique offers qualitative and quantitative analysis for characterizing different materials or phases of similar ones with high specificity. A confocal Raman microscope (HORIBA, Lab RAM HR800) was utilized to investigate the structure of ZnO films shown in Fig. 2.9.

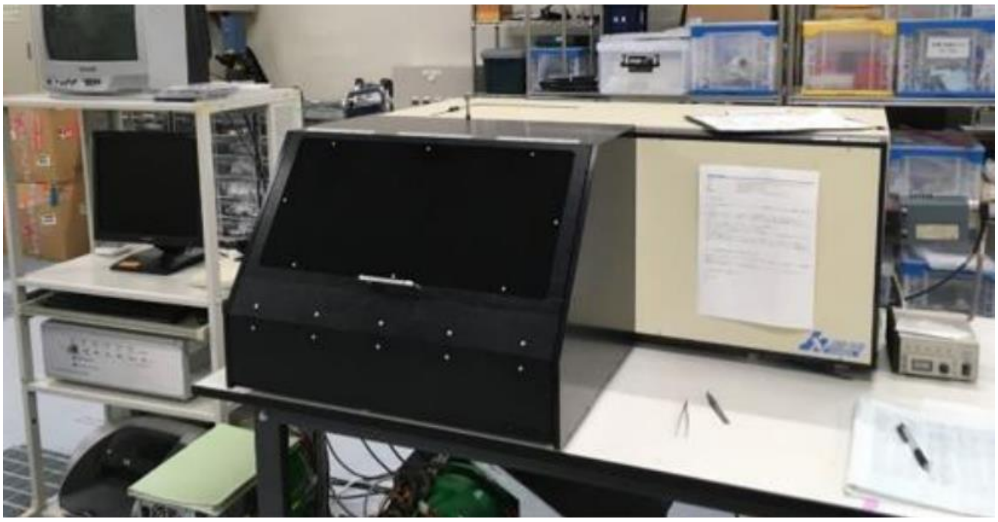

Fig. 2.9 Raman spectroscopy

## 2.3.6 Spectrophotometer

A fundamental method, spectrometer is used for examining the optical characteristics of specimens within the spectrum spanning from near-ultraviolet to infrared light, as shown in the Fig. 2.10. The light from the source passes through a sample, some light is transmitted and some are absorbed by the sample. The detector detected the light and compares light that passes through a sample and compared to light that has not. The resulting spectrum depends on the path length or sample thickness. The obtained spectrum from the measurement is unique to the sample itself. Therefore, the system for generation of mist into TG-DTA 31 transmission spectroscopy can be used as the qualitative measurement of the sample [11-13]. In this research, the optical transmittance spectra of the thin films were measured using a UV-visible spectrometer (Hitachi UV-Vis U-4100) in the wavelength range from 200 to 1000 nm and these results were used to estimate the band gaps of the films from the Tauc relation [14]:

$$(\alpha h\nu)\ 2 = A\ (h\nu - Eg) \tag{1}$$

Where $\alpha$ is the absorption coefficient, $h\nu$ is the photon energy, $Eg$ is the band gap, and $A$ is a constant.

The transmittance spectra and the photodegradation measurements of AZO films, ZnO nanorods, AZO/ZnO core-shell structures, were characterized by this equipment.

Fig. 2.10 Spectrophotometer

## 2.4 References

[1] T. Kawaharamura, H. Nishinaka, S. Fujita. Jpn. J. Appl. Phy. 47 (2008) 4669.

[2] T. Kawaharamura, S. Fujita. Phys. Status Solidi c 5 (2008) 3138-3140.

[3] A. L. Biance, C. Clanet, D. Quere. Phy. Fluids. 15 (2003) 6.

[4] M.A. Sutton, N. Li, D.C. Joy, A.P. Reynolds,X. Li. Experimental Mechanics 47 (2007) 775.

[5] J.L. Vossen, W. Kern. Academic press, San diego, (2012) 177.

[6] J.M. Jensen, A.B. Oelkers, R. Toivola, D.C. Johnson, J.W. Elam, S.M George. Chem. Mater. 14 (2002) 2276.

[7] S. Ahmed, C.M. Hussain. Volume 1. John Wiley & Sons: Beverly, MA, USA, (2018).

[8] G.D. Gilliland. Mater. Sci. Eng. R-Rep. 18 (1997) 99.

[9] S. Hong, T. Joo, W.I. Park, Y.H. Jun, G.-C. Yi. Appl. Phys. Lett. 83 (2003) 4157.

[10] S. Kim, K.D. Kihm, T. Thundat. Exp. Fluids 48 (2010) 721.

[11] G. Binnig, C.F. Quate, C. Gerber. Phys. Rev. Lett. 56 (1986) 930.

[12] S.W. Jung, H.D. Cheong, W.I. Park, H.M. Jang, S. Hong, T. Joo, G.C. Yi. Appl. Phys. Lett., 80 (2002) 1924.

[13] H. Li, X.J. Pan, Y.Z. Zhang, E.Q. Xie, T. Wang. J. Alloys Compd., 472 (2009) 208.

[14] P. Makula, M. Pacia, W. Macyk. J. Phys. Chem. Lett. 9 (2018) 6814.

# Chapter 3

# Synthesis and characterization of AZO films with varied Al doping ratios using mist CVD method

## 3.1 Introduction

Regarding photocatalytic applications, ZnO films emerge as promising semiconductor metal oxide films owing to their exceptional stability and high photocatalytic efficacy, and developing ZnO films with novel structures and cost-effectiveness is essential to further enhancing their photocatalytic potential [1-3]. However, notable challenges still need to be addressed regarding the fundamental principles of photocatalysis utilizing ZnO, alongside the complexity inherent in its synthesis methods. Until now, several methods such as chemical vapor deposition, pulsed laser deposition, molecular beam epitaxy, sputtering have been investigated to generate ZnO films with high crystallinity [4-7].

The innovative mist CVD method had unique properties including growth control, deposition of large-area, cost-efficiency, and simplicity. In our previous research [8], we successfully deposited $TiO_2$ thin films utilizing this novel mist CVD approach. The current chapter extends this method to the synthesis of ZnO thin films. Notably, the thickness of the deposited film, solution concentration, and different substrate stand as significant parameters on the properties of ZnO films during the mist CVD process.

This investigation is focused on the influence of film thickness on the properties of the ZnO thin film, synthesized using a mist CVD process. A subsequent thermal annealing process was operated to enhance the quality of the ZnO thin film. The ensuing exploration encompasses an in-depth analysis of the structural, optical, and electrical attributes intrinsic to the fabricated ZnO thin film.

## 3.2 Influence of film thickness on the properties of ZnO thin film

### 3.2.1 Experiment conditions

The experimental parameters for the deposition of ZnO films through mist CVD are described in Table 1. A mixed precursor solution was prepared by dissolving zinc acetate (ZA)

(0.04 mol/L) in a mixture of methanol and water (in a ratio of 90 ml methanol to 10 ml water). This solution was subsequently introduced into the mist solution chamber and transported to the reaction chamber by employing nitrogen gas as carrier and dilution gas. In order to investigate the influence of deposition thickness, film thicknesses were systematically varied, encompassing values of 300 nm, 450 nm, 600 nm, and 750 nm, each incremented by intervals of 150 nm. The structural and optical properties of the deposited ZnO films were investigated by using SEM, XRD and transmission spectroscopy techniques.

Table 3.1. Deposition conditions of ZnO films with varied thicknesses by mist CVD

| Deposition Parameter | Condition |
|---|---|
| Solute | Zinc acetate |
| Solvent | Methanol, $H_2O$ |
| Concentration (mol/L) | 0.04 |
| Deposition temperature (°C) | 400 |
| Carrier gas, flow rate (L/min) | 2.5 |
| Dilution gas, flow rate (L/min) | 4.5 |

### 3.2.2 Results and discussion

Fig. 3.1 illustrates SEM images of ZnO films through the mist CVD technique, with various thicknesses. In the top view, the surface images distinctly revealed the wedge-like structure comprised of ZnO nanosheets with high uniformity across all film surfaces. Notably, as the thickness of the ZnO films increased from 300 to 750 nm, the average grain sizes were also increased, ranging from 98 to 200 nm. From the cross-sectional view, the columnar structure was found and the 750 nm-thick ZnO film exhibited the most prominent columnar structure.

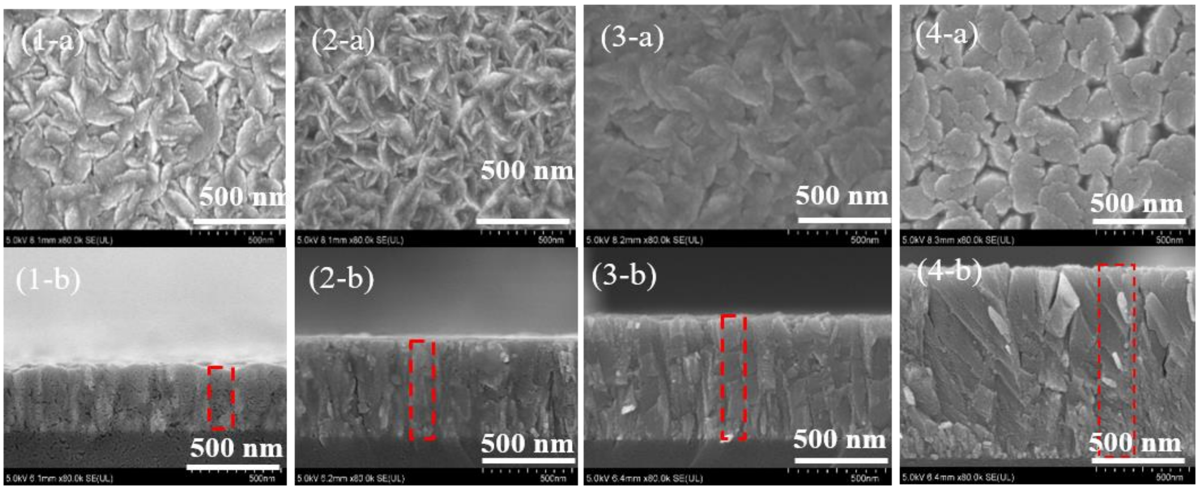

Fig. 3.1 SEM images of fabricated ZnO films with varied thicknesses by mist CVD. ((1) 300 nm; (2) 450 nm; (3) 600 nm; (4) 750 nm; (a) top view; and (b) cross-section view).

Fig. 3.2 presents the XRD patterns of ZnO thin films deposited by different thicknesses. A dominant (002) peak appeared for all the films, which indicated the preference for c-axis-oriented growth during the mist CVD process. The peak intensity was significantly increased by increasing the film thickness from 300 nm to 750 nm. Remarkably, the 700 nm-thick ZnO film exhibits the highest (002) peak intensity and the sharpest full width at half maximum (FWHM). The highest crystallinity and smallest FWHM values were achieved from the 750 nm-thick ZnO film.

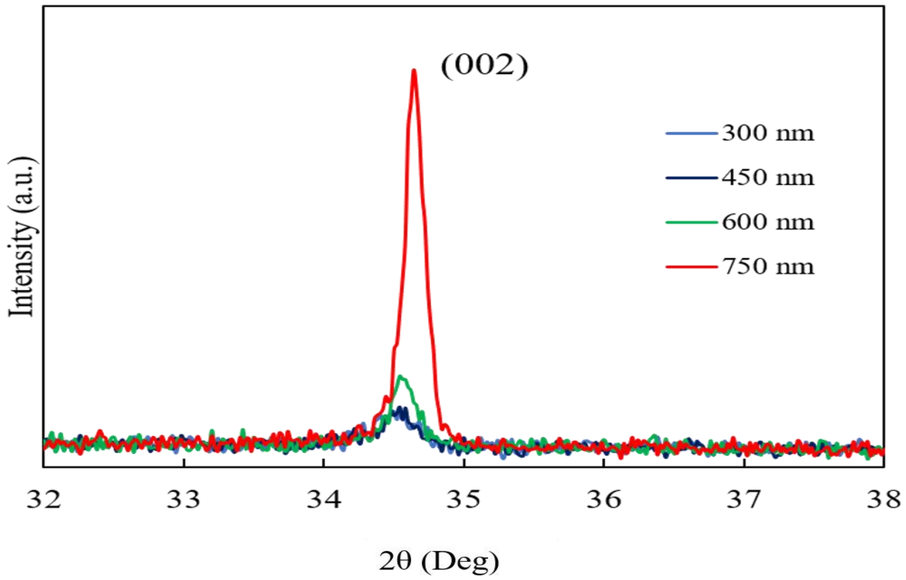

Fig. 3.2 2 theta patterns of fabricated ZnO films with varied thicknesses by mist CVD.

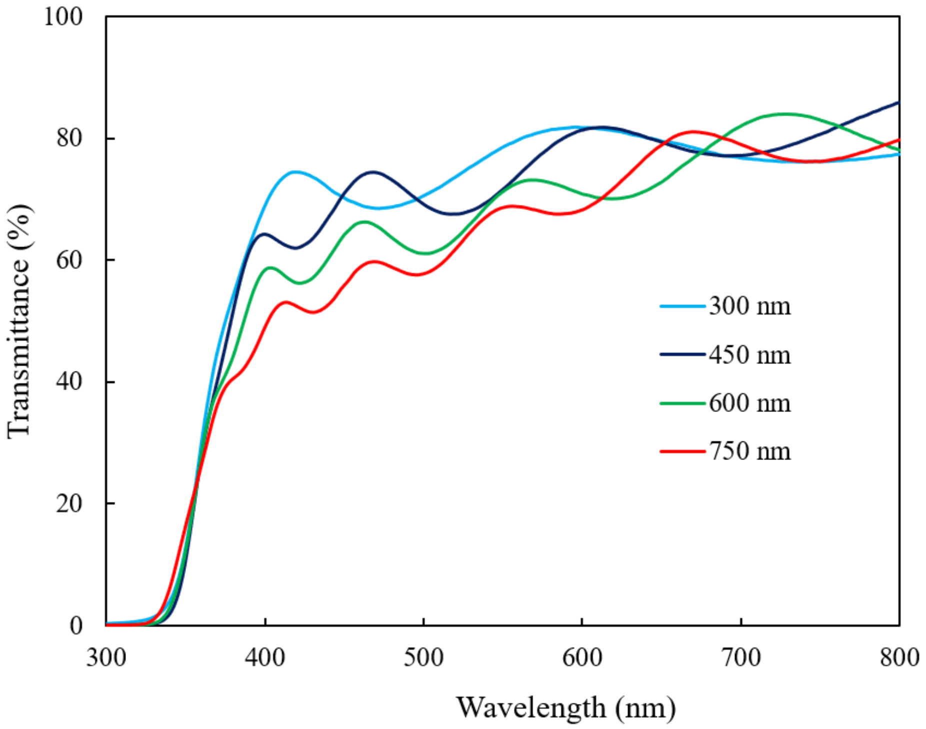

Fig. 3.3 Transmission spectra of fabricated ZnO films with varied thicknesses by mist CVD.

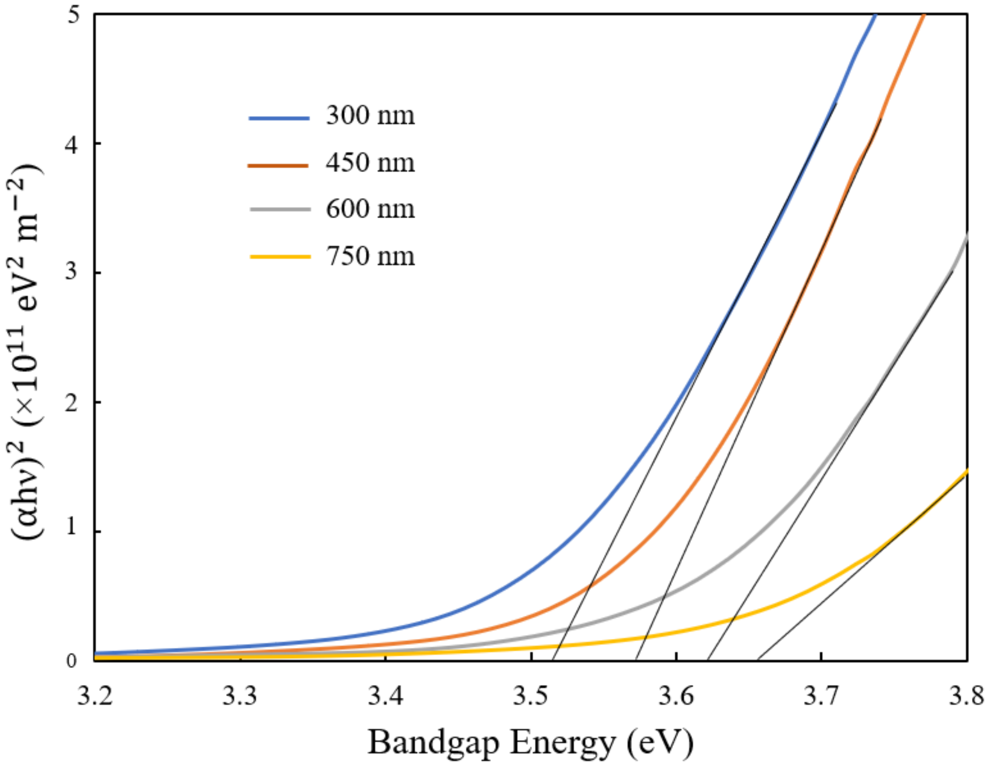

Fig. 3.4 Variation of $(\alpha h\upsilon)^2$ of the fabricated ZnO films with varied thicknesses by mist CVD as a function of the photon energy (hυ).

The optical transmittance of ZnO films with varying thicknesses as shown in Fig. 3.3, revealing an average transmittance of 72% within the visible region. A significant observation is the shifting of the absorption edge towards shorter wavelengths as the film thickness increases. Based on the Tauc's plot theory [9]. The determination of the optical band gap involves extrapolating the plot of $(\alpha h\nu)^2$ against hν, as depicted in Fig. 3.4. Notably, the calculated band gap energies for the as-deposited ZnO films are 3.244 eV, 3.269 eV, 3.273 eV, and 3.271 eV, corresponding respectively to film thicknesses of 300 nm, 450 nm, 600 nm, and 750 nm. This variation underscores the influence of film thickness on the band gap energy of ZnO films.

### 3.2.3 Conclusions

ZnO films with different thicknesses were successfully deposited by the mist CVD method. Wedge-like structures of ZnO nanosheets with good uniformity were observed for all films and the average grain size was increased when thickness of the ZnO film is increased. The dominant peak of (002) was occurred for all films and high crystallinity was obtained from 750 nm-thick ZnO film. The transmission spectra of all obtained ZnO films were around 70% in the visible region. The obtained ZnO films were expected to apply in photocatalytic applications.

## 3.3 Influence of thermal annealing on the properties of ZnO film

In order to improve the film quality and the properties of obtained ZnO films. The vacuum annealing treatment was carried out after the mist CVD process.

### 3.3.1 Experiment conditions

The deposition conditions of ZnO films were summarized in Table 3.1. The deposited thickness of ZnO film was 300 nm. Following the mist CVD deposition, the obtained ZnO film was annealed in the vacuum at 700°C for one hour. The structural and optical properties were investigated as well.

### 3.3.2 Results and Discussion

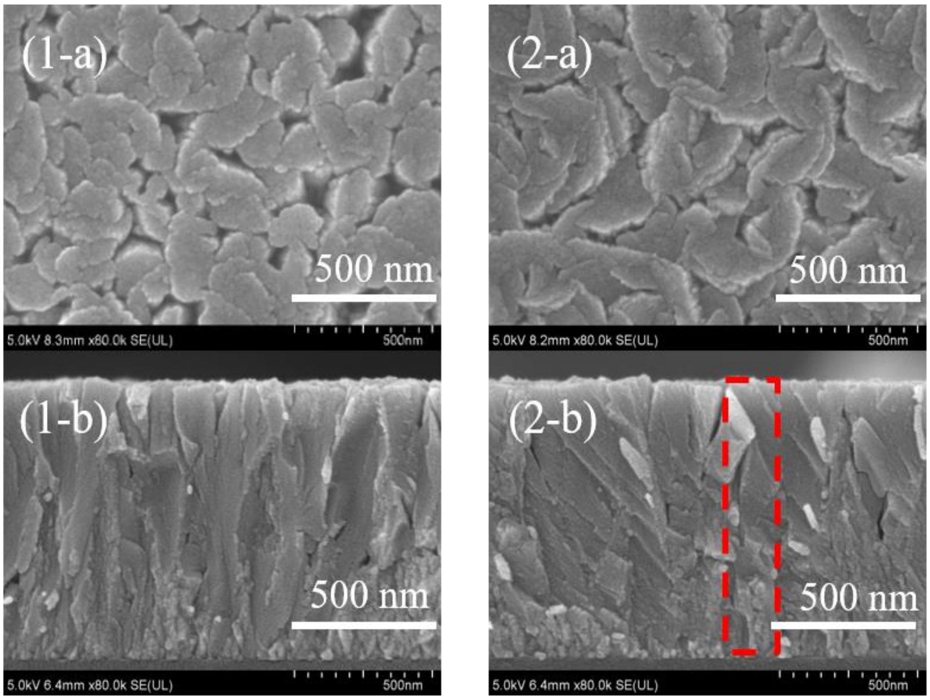

Fig. 3.5 SEM images of (1) as-deposited ZnO film, and (2) annealed ZnO film with 300 nm thickness: (a) top view; and (b) cross-section view.

The morphology of as-deposited ZnO film and annealed ZnO thin film were examined using an SEM, as illustrated in Fig. 3.5. Wedge-like structure was found on both ZnO surfaces and the average grain size was increased from 200 nm to 240 nm when the ZnO was annealed. It can be clearly observed that the most columnar structure was found in the annealed ZnO film.

Fig. 3.6 shows the XRD patterns of both as-deposited and annealed ZnO thin films. A single dominant (002) peak was obtained in all the films, corresponding to the preferred c-axis orientation growth. Following the annealing process, the intensity of the (002) peak was enhanced with a reduction in the FWHM values. Moreover, the average c-axis crystallite size was increased from 57.53 nm to 66.36 nm after annealing. It was clearly revealed that the annealed ZnO films might be contributed to enhance the crystallinity of ZnO film.

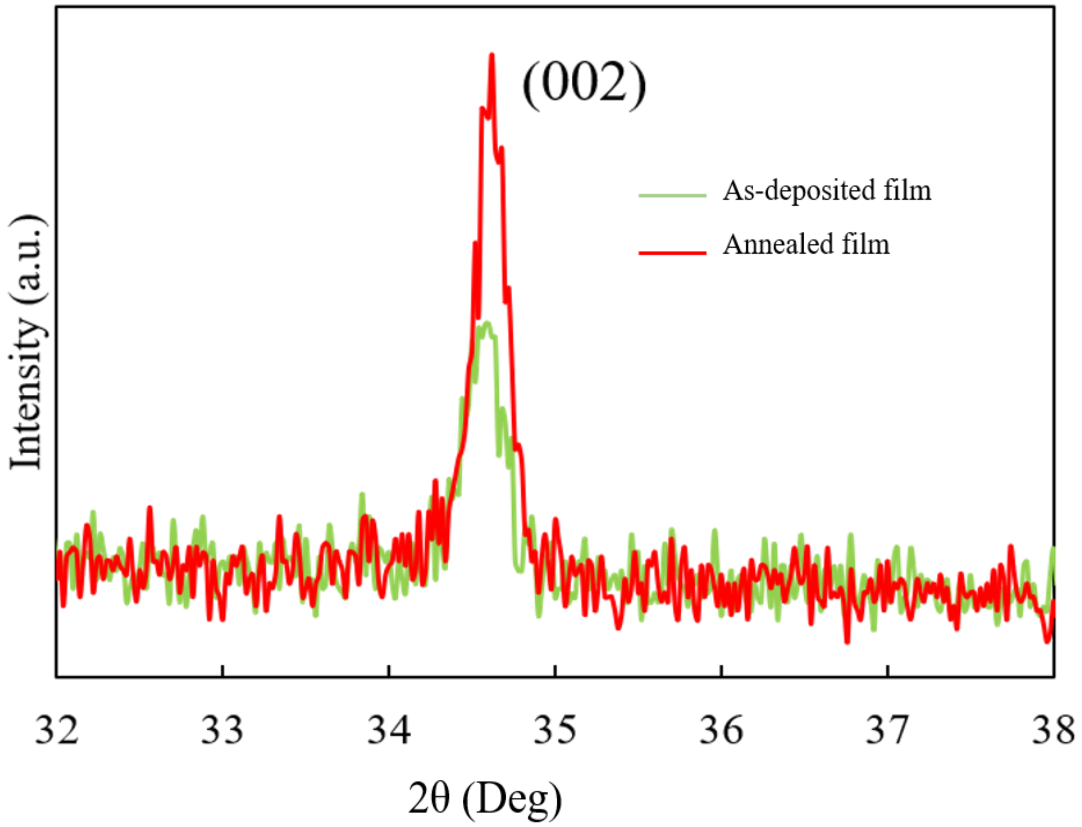

Fig. 3.6 2 theta patterns of as-deposited ZnO film and annealed ZnO film with 300 nm thickness.

Fig. 3.7 illustrates the Raman spectra of both as-deposited ZnO film and annealed ZnO film, both deposited through the mist CVD method. Distinct peaks at 580 cm$^{-1}$ and 720 cm$^{-1}$ corresponding with the E1 (LO) mode and the secondary Raman peak of ZnO were found, respectively. Following the annealing process, a notable enhancement in the intensity of the Raman peak is evident. This enhancement indicates a considerable improvement in the crystallinity of the ZnO films, which had well agreement with the results obtained from XRD measurements.

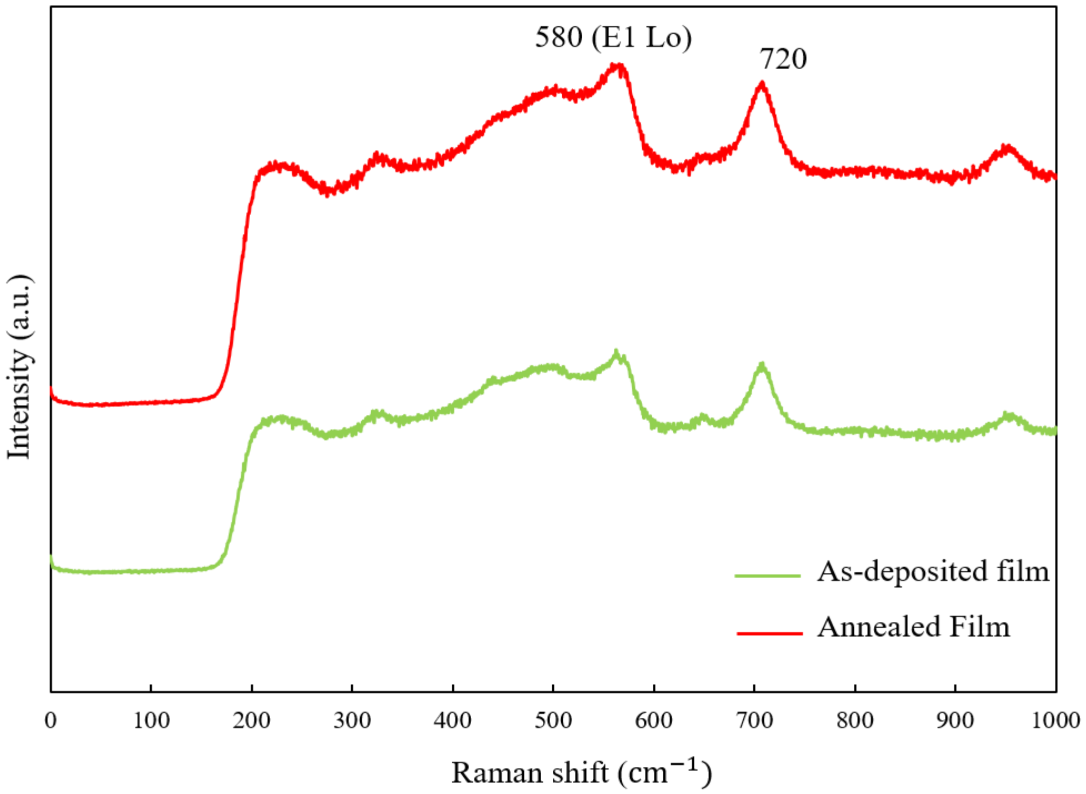

Fig. 3.7 Raman spectra of as-deposited ZnO film and annealed ZnO film with 300 nm thickness.

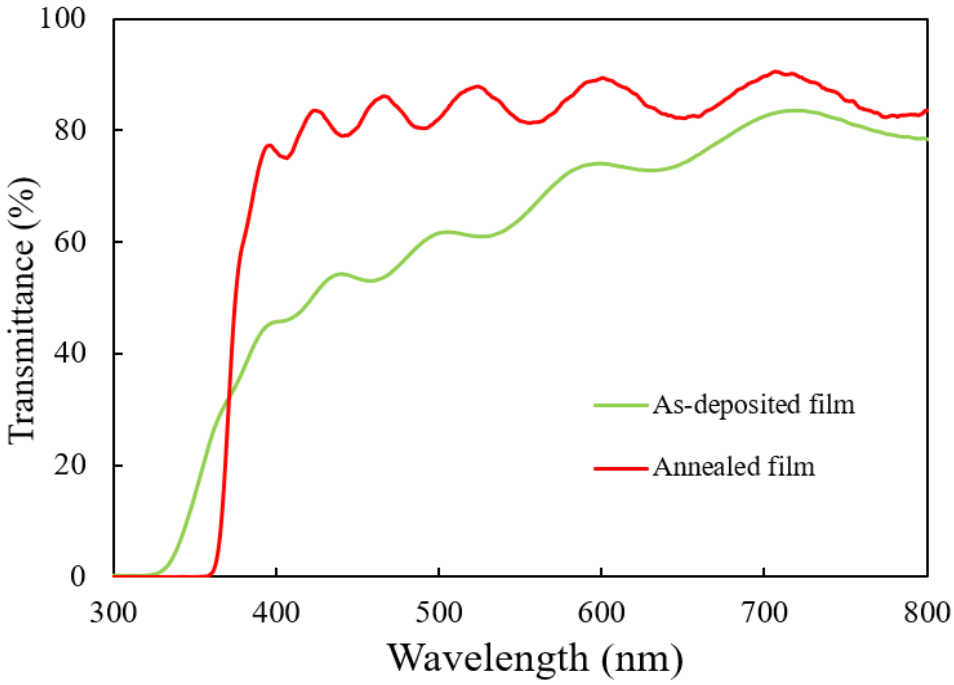

Fig. 3.8 Transmission spectra of as-deposited ZnO film and annealed ZnO film with 300 nm thickness.

The transmittance spectra of as-deposited ZnO film and annealed ZnO film deposited by mist CVD method are shown in Fig. 3.8. It was observed the transmittance was increased to over 80 % when ZnO film was annealed. The evaluated optical bandgap was decreased from 3.65 eV to 3.38 eV after annealed.

### 3.3.3 Conclusions

ZnO films were effectively deposited utilizing the mist CVD method. Subsequently, the effect of thermal annealing on these ZnO films was explored. Notably, all the films displayed wedge-like structures comprising ZnO nanosheets exhibiting high uniformity. After annealing process, the average grain size of ZnO film was increased. The dominant peak for both ZnO films was (002) peak, which was preferred to c-axis orientation growth along the (0001) crystal plane. The highest crystallinity, and smallest FWHM values were obtained at annealed ZnO film. The transmission spectra of as-deposited ZnO film were 70% in the visible region. After annealing, the transmittance was significantly increased to over 80%.

## 3.4 Influence of Al concentration ratios on the properties of AZO films

Upon irradiation, excitation of photogenerated charge carriers, diffusion, and subsequent surface transfer of generated electron-hole pairs can primarily determine the photodegradation efficiency of ZnO [10]. Nevertheless, the rapid recombination charge carriers can diminish the overall degradation efficiency of ZnO [11]. Decreasing the recombining effects of these charge carriers can be achieved through surface modification, introducing defects, or incorporating transition metals into the ZnO [12,13]. Among these strategies, incorporating Al is expected to be particularly effective in reducing the recombination rate of electron-hole pairs in ZnO [14-17].

In this section, we applied the mist CVD technique to deposit AZO thin films. The focus of this study was to explore the influence of different Al doping ratios on the properties of the resultant AZO films. Additionally, we examined the photodegradation performance, which contributed to a comprehensive understanding of their potential in photocatalytic applications.

### 3.4.1 Experiment conditions

Utilizing the mist CVD technique, 300 nm-thick AZO films were synthesized upon glass substrates. To initiate this procedure, a precursor solution was prepared by mixing ZA (0.04 mol/L) and aluminum acetylacetonate (AA) in a solvent mixture consisting of water and methanol, with a ratio of 90 mL of water to 10 ml of methanol. Subsequently, an ultrasonic transducer at a frequency of 2.4 MHz was employed to generate mist droplets from the precursor solution within the solution chamber. These droplets were then transported to the reaction chamber, facilitated by nitrogen gas which served the dual purpose of carrier gas (flow rate: 2.5 L/min) and dilution gas (flow rate: 4.5 L/min).

Within the reaction chamber, the substrate was strategically positioned within the FC reactor. This substrate was consistently maintained at a temperature of 400°C during the mist CVD process. The effect of varying Al doping ratios on the structural and optical characteristics of AZO films was examined. A comprehensive summary of the deposition conditions of AZO films is described in Table 3.2.

Table 3.2 Deposition conditions of AZO films by mist CVD method

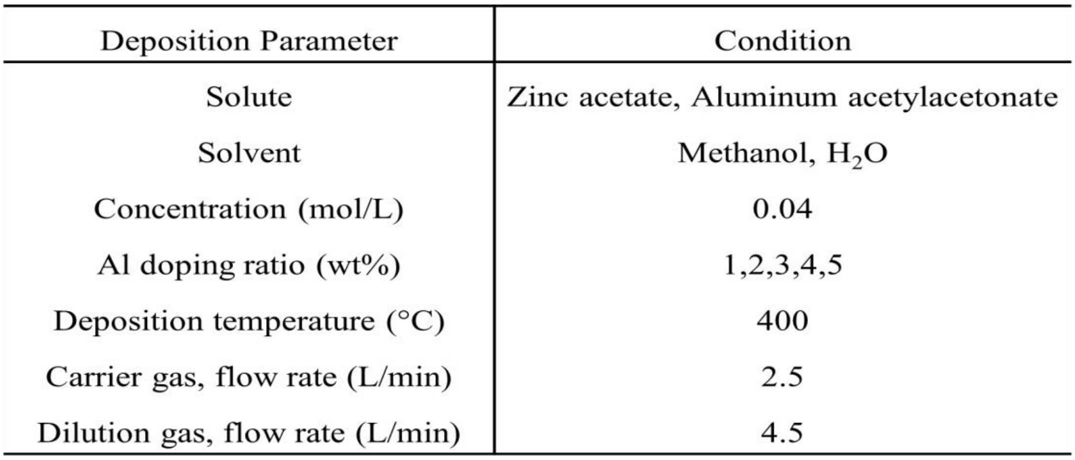

| Deposition Parameter | Condition |
|---|---|
| Solute | Zinc acetate, Aluminum acetylacetonate |
| Solvent | Methanol, $H_2O$ |
| Concentration (mol/L) | 0.04 |
| Al doping ratio (wt%) | 1,2,3,4,5 |
| Deposition temperature (°C) | 400 |
| Carrier gas, flow rate (L/min) | 2.5 |
| Dilution gas, flow rate (L/min) | 4.5 |

The photodegradation process of the deposited AZO films was performed within a glass beaker during the degradation process, which conducted at ambient room temperature. A solution of MR dyes with a concentration of $1\times10^{-5}$ mol/L was dissolved in the water with the concentration of 70 ml. Before photocatalytic experiment, the mixed solution was enveloped in Al sheet to avoid light exposure for half hour. Following this stage, the solution was adequately stirred prior to irradiation.

Once the stirring process was completed, the prepared AZO film samples were individually submerged into the precursor solution. Subsequently, the entire setup was subjected under UV light irradiation (254 nm) for 5 hours. The irradiated solution was collected at one-hour intervals throughout the experiment to examine the degradation rate with the varying of Al doping ratios.

### 3.4.2 Results and Discussion

Fig. 3.9 displays AFM images of the AZO films deposited using the mist CVD technique, with varying Al doping ratios. The scanned area for each image was 5 μm × 5 μm. When the Al ratio increases from 1 wt% to 2 wt%, a fascinating fact is that the root mean square (RMS) value of the AZO film decreases from 6.41 nm to 3.78 nm. Subsequently, as the Al ratios increase to 5 wt%, the RMS values experienced a rise to 9.72 nm. Among these, 2 wt% Al doped ZnO film showed the smallest RMS value. A comprehensive overview of the calculated RMS values is shown in Table 3.3.

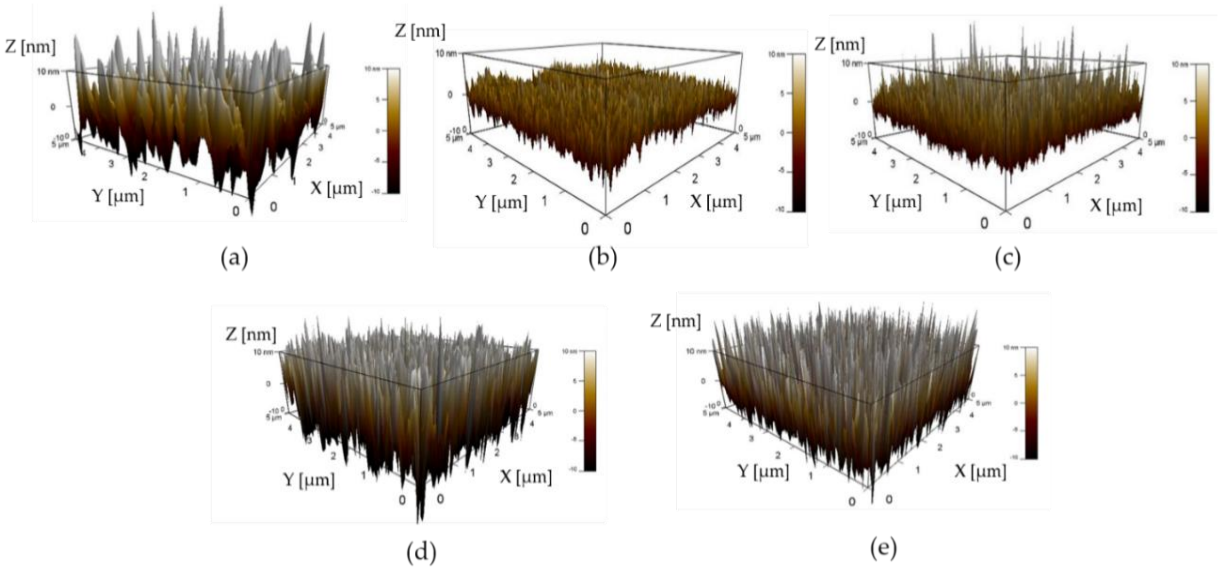

Fig 3.9 AFM images of deposited AZO films with varied Al doping ratios(a) 1% Al, (b) 2% Al, (c) 3% Al, (d) 4% Al, and (e) 5% Al.

Table 3.3. The AFM analysis data of AZO films

| **Al doping ratio (wt%)** | **RMS roughness (nm)** |
|---|---|
| **1** | 6.4 |
| **2** | 3.7 |
| **3** | 4.6 |
| **4** | 8.8 |
| **5** | 9.7 |

Fig. 3.10 illustrates the XRD patterns of deposited AZO films with varied Al doping ratios. For AZO films doped with 1 wt%, three diffraction peaks of (100), (002), and (101) were found. With an increase in Al doping to 2 wt%, the (100) and (002) peaks exhibit a diminishing intensity, then appeared dominant (101) peak upon further increasing the Al doping ratio to 3 wt%. This observation confirms that the growth of the AZO film predominantly aligns with a highly preferred orientation along the (101) crystal plane. When the Al doping ratios reached to 4 wt% and 5 wt%, no diffraction peaks can be observed, suggesting the formation of amorphous film.

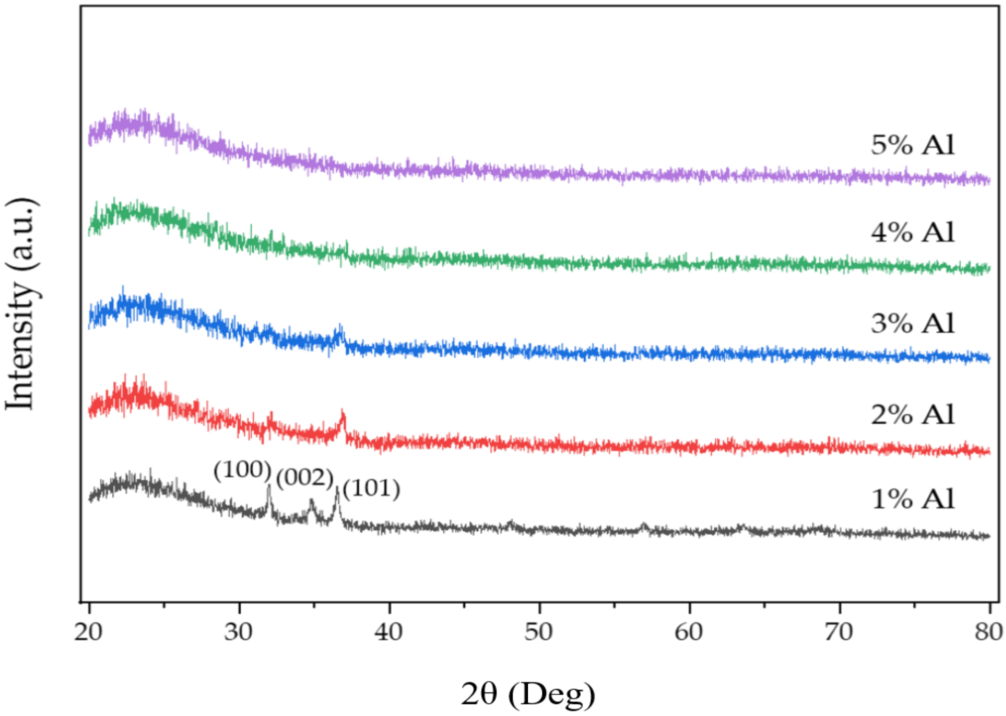

Fig. 3.10 2 theta patterns of deposited AZO films with varied Al doping ratios

Table 3.4 Texture coefficient values of AZO films deposited with varied Al ratios.

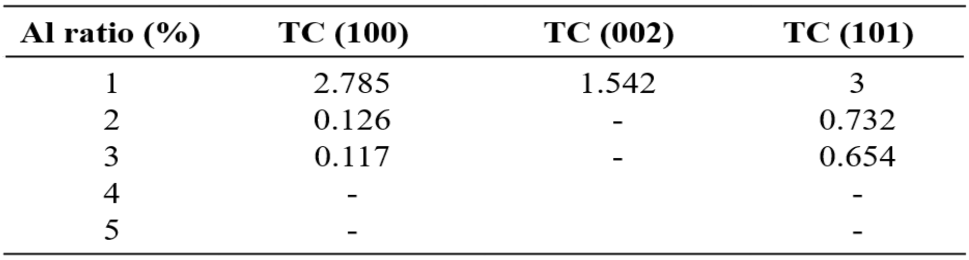

| Al ratio (%) | TC (100) | TC (002) | TC (101) |
|---|---|---|---|
| 1 | 2.785 | 1.542 | 3 |
| 2 | 0.126 | - | 0.732 |
| 3 | 0.117 | - | 0.654 |
| 4 | - |  | - |
| 5 | - |  | - |

Moreover, when calculating the average crystallite size of AZO film obtained using the Debye-Scherrer's principle [18], it can be observed that the calculated crystallite size decreased from 31.85 nm to 13.57 nm as Al doping ratios increased from 1 wt% to 3 wt%.

By using texture coefficient (TC) formula for the (h k l) plane [19], the preferred growth direction along various crystallographic planes, denoted as (h k l), can be measured. With the increasing Al doping ratios ranging from 1 wt% to 3 wt%, the obtained TC values derived from the XRD analysis data are presented in Table 3.4. Analysis of these TC values confirms that the (002) peak was exclusively presented at 1 wt% Al doped ZnO film. Furthermore, a significant reduction in the TC value of the (100) peak corresponded to the increase of the Al ratio from 1 wt% to 3 wt%. Among three diffraction peaks, highest TC value was obtained from (101) crystal plane, which was indicated that the preferred growth of AZO films predominantly aligns with the (101) crystal plane.

Fig. 3.11 presents SEM images of AZO films deposited using the mist CVD method. It can be observed distinct surface morphologies resulting from different Al doping ratios. Notably, significant transformations in surface features are observed when the Al doping ratios was increased. Specifically, the intertwined nanosheets structure was obtained from Al doping ratios of 1 wt% and 2 wt%. However, when Al ratios increased from 3 wt% to 5 wt%, this nanosheet structure undergoes a substantial reduction in length, eventually transitioning into uniform particles. This structural evolution is likely attributed that the incorporation of varied Al caused the shifts in the lattice structures of ZnO films. When the Al doping ratios increased, the higher concentration of $Al^{3+}$ ions (with an ionic radius of 0.53 Å), substituting $Zn^{2+}$ ions (with an ionic radius of 0.74 Å) within the ZnO film [20]. This substitution, driven by the different ionic radii, introduces structural distortion, contributing to the changes in the morphology of obtained AZO films.

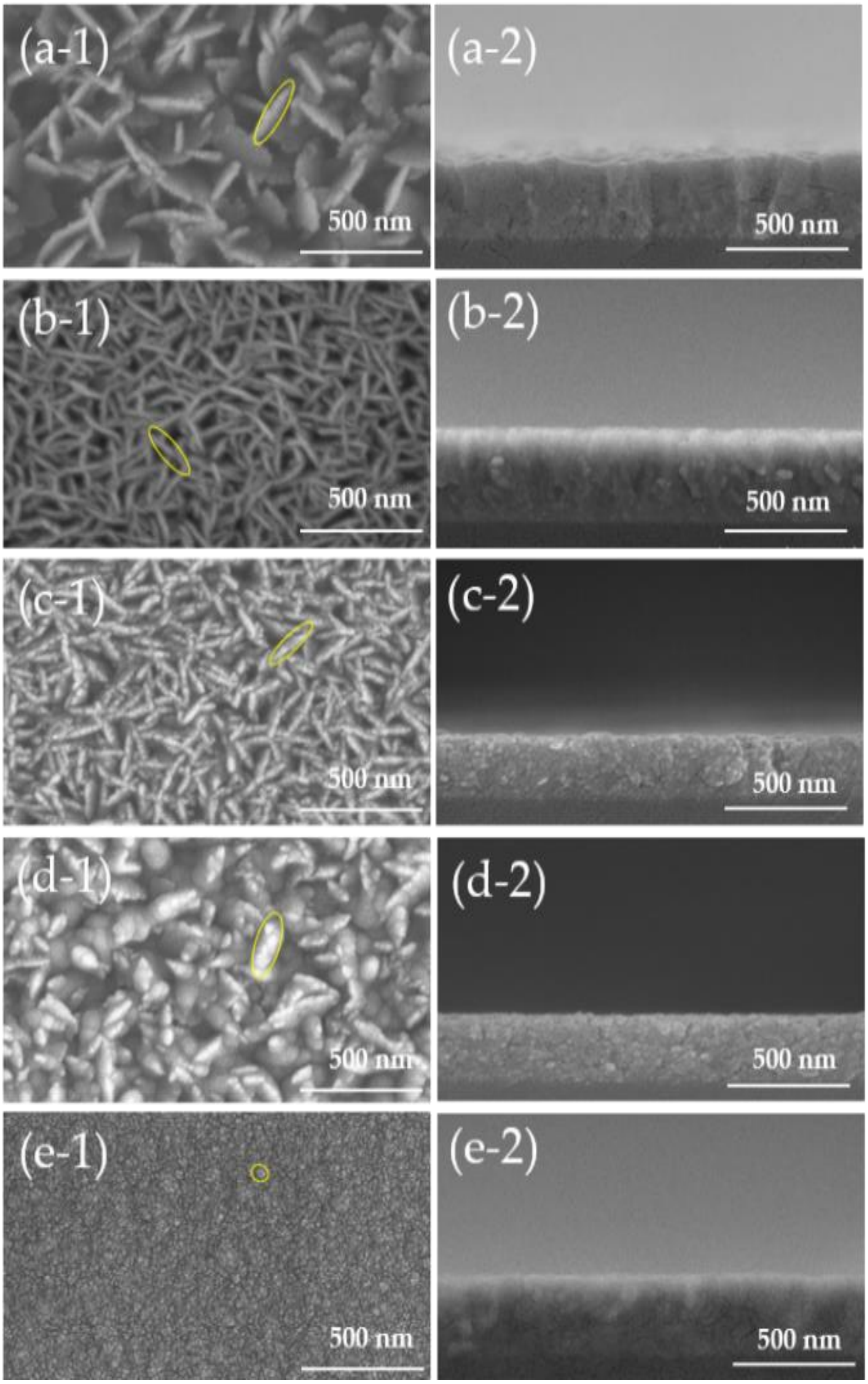

Fig. 3.11 SEM images of deposited AZO films with varied Al doping ratios. ((a) 1% Al, (b) 2% Al, (c) 3% Al, (d) 4% Al, and (e) 5% Al: (1) top view, and (2) cross-section view).

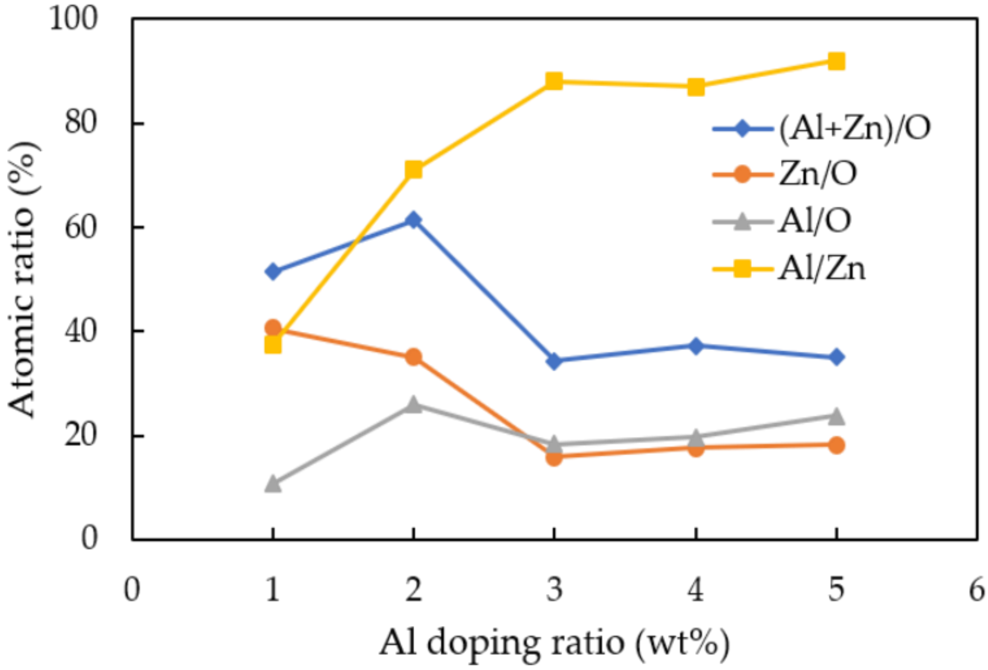

Fig 3.12 Atomic ratios variations of Zn, Al, and O calculated from EDX analysis from deposited AZO films with varied Al doping ratios.

To study the atomic variations of the AZO films with different Al doping ratios, EDX measurement was performed. The atomic variations of Zn, Al and O are graphically presented in Fig. 3.12. When the Al ratios increased from 1 wt% to 5 wt%, a high concentration of Al ions was incorporated into the ZnO structure, then the atomic ratio of Al/Zn was significantly increased, wherein the maximum ratio Al/Zn was attained at 3 wt% Al doping ratios. Conversely, the atomic ratios of Al/O and (Al+Zn)/O exhibit slight increases when the Al ratios was up to 5 wt%. Notably, the atomic ratios of Zn/O exceed ratio of Al/O when the Al ratios was increased from 1 wt% to 2 wt%, which highlighted the predominant formation of Zn-O bonds in generating ZnO.

However, when Al ratios exceed 3 wt%, the atomic ratio of Al/O was greater than the atomic ratio of Al/O, which suggested that $Al^{3+}$ aided as the oxidizing agents, and substituting into Zn ions within oxygen ion sites, thereby giving rise to the formation of AZO and $Al_{1-x}O_x$ compounds. Nevertheless, the atomic ratio of (Al+Zn)/O exhibited distinct behavior. Initially, it displayed an upward direction, reaching the highest value at 2 wt%, then decreased and maintained a relatively steady level as the Al doping ratios increased to 5 wt%. It could be attributed to oxygen ion bonding saturation point within composition.

In Fig. 3.13, the growth mechanism underlying the deposition of AZO films with varying

Al doping ratios using the mist CVD. This growth process can be categorized into three steps: (a) generation of mist droplets, (b) decomposition and (c) growth process. In initial step, a precise mixture of ZA and AA precursors was poured within the prepared chamber. Subsequently, the ultrasonic transducer was used to change the mixed precursor into mist droplets. At decomposition process, both ZA and AA components in the form of mist droplets were travelled to the reactor using a carrier and dilution gas. Within the reaction chamber, a finely channeled substrate is preheated and maintained at a temperature of 400°C.

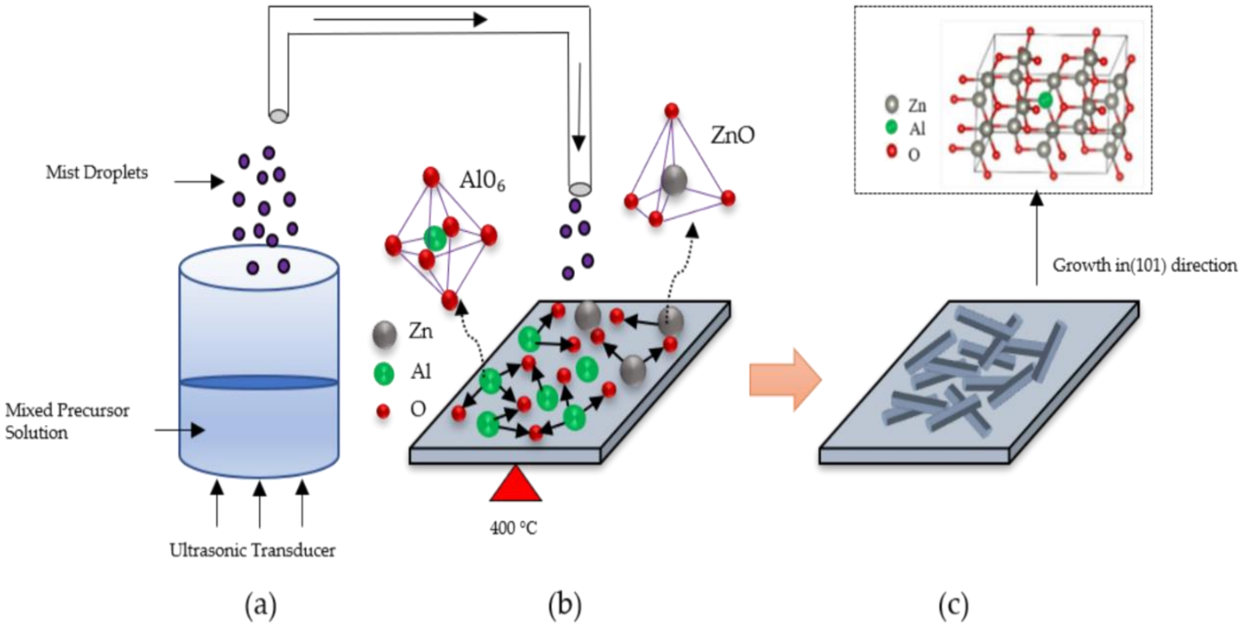

Fig. 3.13 The growth process of deposited AZO films with varied Al doping ratios:(a) generation of mist droplets, (b) decomposition, and (c) growth stage.

Continuously, when the substrate temperature (400°C) was over the decomposition temperature of ZA (237°C) and AA (193°C), dissociation of AA and ZA precursors led to the release of Al and Zn species. These liberated species then diffuse and adsorb onto the substrate surface, initiating the nucleation of AZO thin films. Owing to the comparatively lower decomposition temperature of AA, it is easy to promote the generation of decomposed Al ions. The decomposition of aluminum ions proved to be notably more facile than zinc ions, resulting in a greater propensity to form bonds with oxygen ions. This distinction can be attributed to the lower decomposition temperature of AA than that of ZA. Due to the lower decomposition temperature of AA than ZA, the generated Al ions exhibit an inherent tendency to bond with oxygen ions.

Furthermore, prior report [21] have indicated that when the deposition temperature is more significant than 350°C, the bonding mode of $AlO_6$ might be established during a mist deposition process. Consequently, under our experimental circumstances with the deposition temperature of 400°C, the formation of Al-O bonding becomes dominant, thus leading to the formation of $Al_{1-x}O_x$ compounds. The results were indicated that the nucleation of ZnO crystals was suppressed.

In the growth stage, the obtained AZO films exhibiting a preference for growth along the (101) orientation, possibly attributed to the faster growth rate than other growth directions [22]. As a result, the formation of intertwined nanosheet structures was observed as the Al doping ratios increased from 1 wt% to 3 wt%.

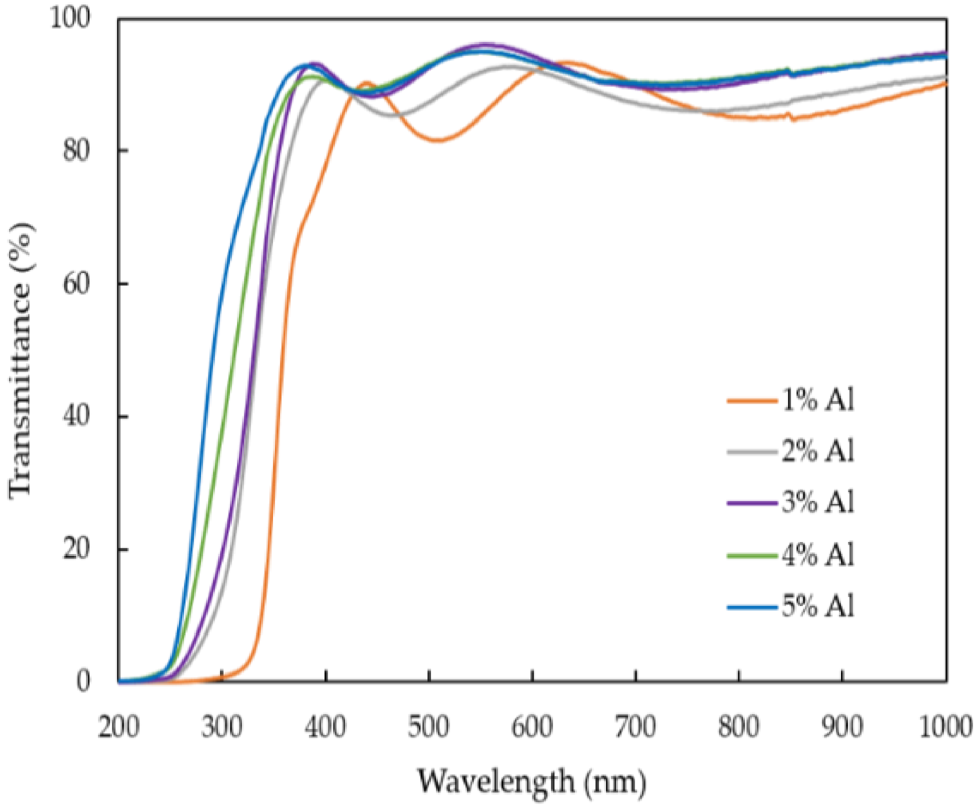

Fig. 3.14 Transmittance spectra of deposited AZO films with varied Al doping ratios by mist CVD method.

The transmittance spectra of obtained AZO films doped with varied Al ratios is shown in Fig.3.14. It is evident that all AZO films exhibit transmittance exceeding 80% within the visible region. Interestingly, when the Al ratios are raised to 5 wt%, a noticeable blue shift in the absorption edge is observed, indicating a slight increase in energy level gaps.

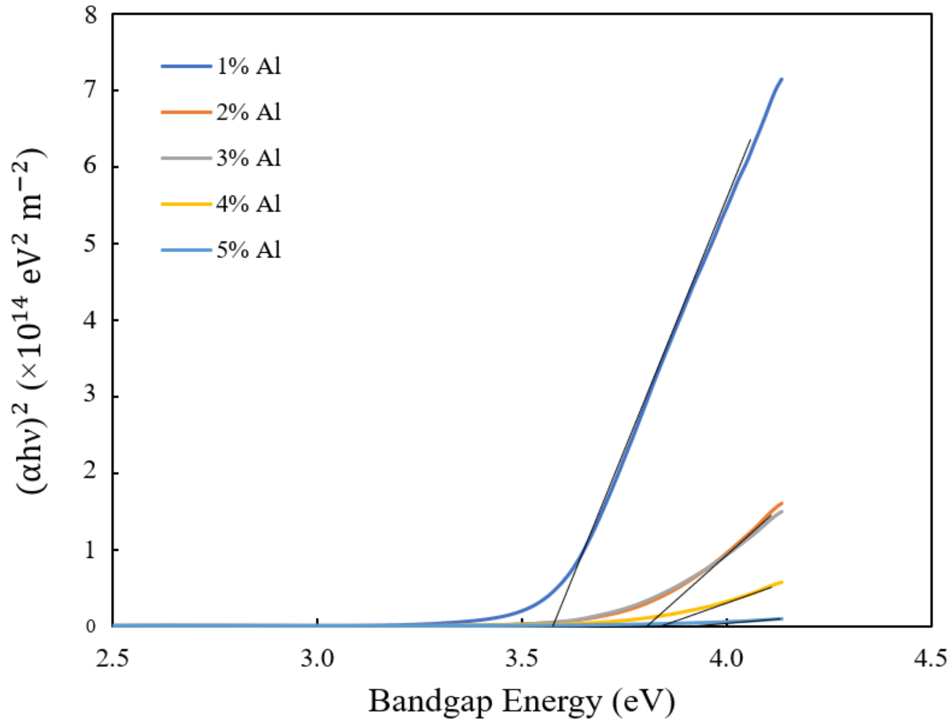

Fig. 3.15. Variation of (αhυ)$^2$ of the deposited AZO films with varied Al doping ratios as a function of the photon energy (hυ).

The variation of optical bandgap is depicted in Fig. 3.15, which is obtained from plotting (αhv$^{)2}$ against the photon (hv) for varied Al ratios. By using Tauc's plot equation [23], the calculated bandgaps exhibit an increase from 3.57 eV to 3.85 eV with the increasing of Al ratios.

The absorption spectra of MR solution corresponding to deposited AZO films using the mist CVD method with varying Al doping ratios are shown in Fig. 3.16. An obvious decrease in absorption intensities was observed within the 470 nm to 700 nm range when Al doping ratios increased from 1 wt% to 2 wt%, in contrast to the origin MR solution. These observations suggest achievement of photodegradation efficiency. When the doping ratios increased to 4 wt%, the absorption intensity was slightly increased. The most significant reduction in absorption intensity was observed at an Al doping ratio of 2 wt%. However, as the Al ratios were further raised to 5 wt%, the absorption spectra were greater than that of original MR solution, indicating an absence of photodegradation efficiency.

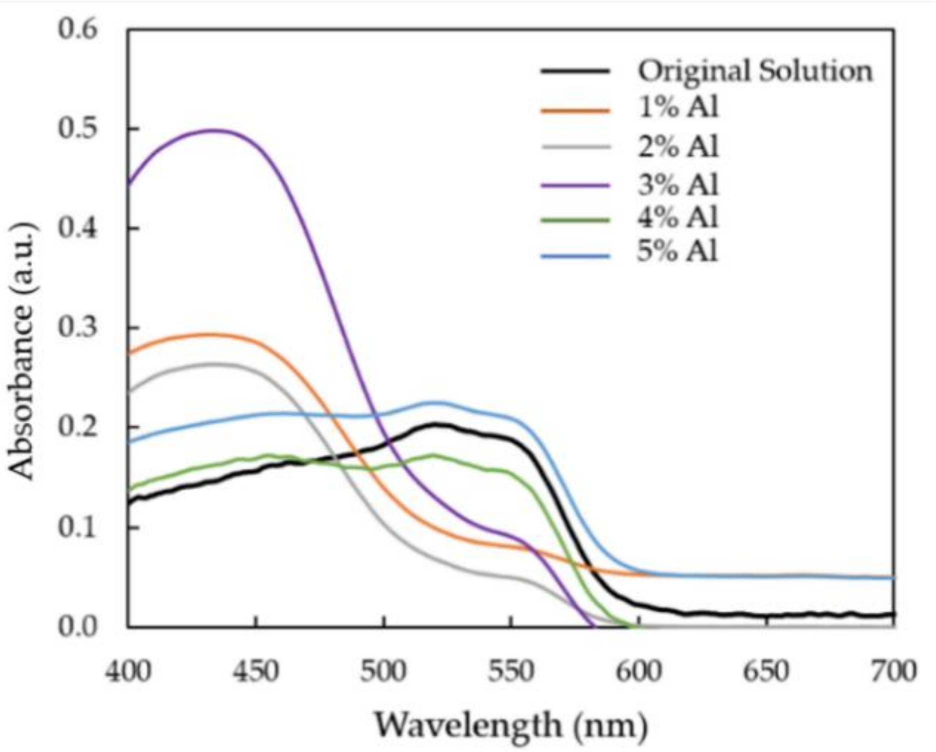

Fig. 3.16 The absorption spectra of MR solution for deposited AZO films with varied Al doping ratios.

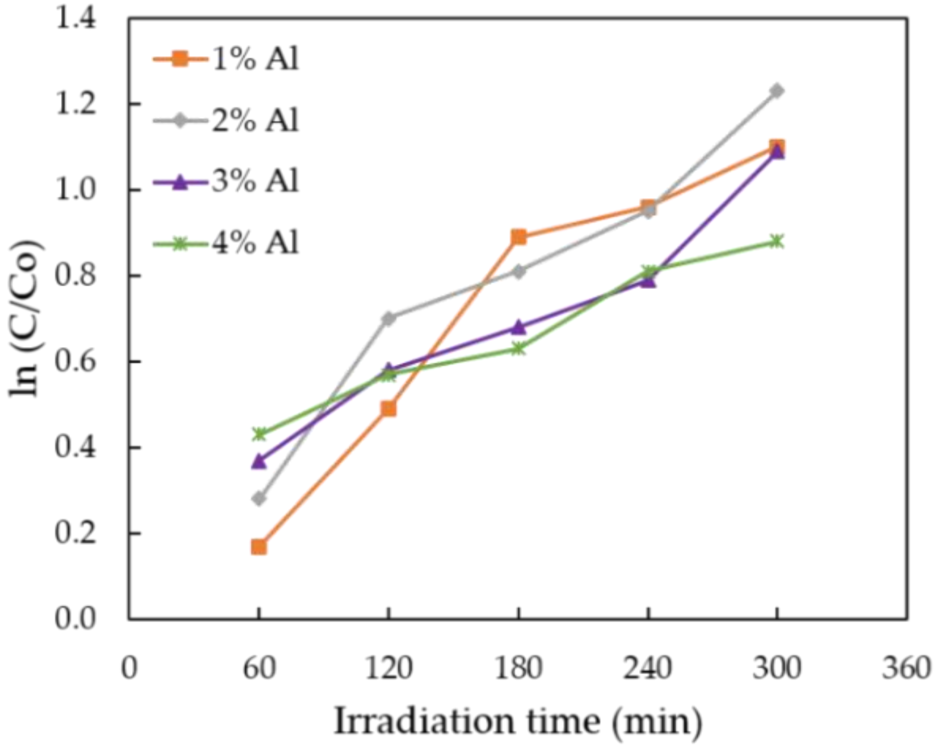

Fig. 3.17 Plot of ln (C/Co) with the irradiation times for deposited AZO films with varied Al doping ratios.

The MR absorption band at 520 nm was used for calculating the degradation rate of the obtained AZO films. The degradation kinetics of various organic dyes was characterized by employing the Langmuir–Hinshelwood (L–H) model [24]. This model describes the adsorption rate on the surface of photocatalytic materials with the overall ratios of adsorbed reactants. Eq. (2) was described the surface reaction rate (R) as follows [25-27]:

$$R = k_r\theta \tag{2}$$

Here, kr is the constant of reaction rate, and θ is the overall ratios of surface reactants. Based on adsorption theory, the capacity of adsorption and concentration of reactants are related to the overall ratio of the reactant.

For pseudo-first-order reaction, based on the Eq. (2), Eq. (3) is derived as follows.

$$kt = \ln\left(\frac{C}{Co}\right) \tag{3}$$

where k is the constant first-order degradation reaction rate.

The graph of ln(C/Co) with irradiation time, wherein the degradation of the MR solution for AZO films was illustrated in Fig.3.17. A higher value of the first-order degradation rate indicates superior photodegradation efficiency. In order to determine first order degradation reaction rate k, Eq. (4) is derived be from Eq. (3).

$$k = \frac{\ln\left(\frac{C}{Co}\right)}{t} \tag{4}$$

The calculated degradation reaction rate was enhanced from 0.0031 $\text{min}^{-1}$ to 0.0040 $\text{min}^{-1}$ with increasing of Al doping ratios. Subsequently, a reduction from 0.00054 $\text{min}^{-1}$ to 0.00038 $\text{min}^{-1}$ was observed while the Al doping ratios increased from 3 wt% to 4 wt%. Notably, the AZO film exhibited a high reaction rate with an Al doping ratio of 2 wt%.

### 3.4.3 Conclusions

The mist CVD method was successfully employed to deposit AZO films with varying Al ratios. The investigation revealed a substantial influence of the Al ratios on the properties of AZO films. An enhanced preferred orientation along (101) crystal planes was observed with the increasing of Al ratios to 3 wt%. Among varied Al doping ratios, 2 wt% Al doping ratios exhibited high crystallinity and low surface roughness. With the increasing of Al doping ratios, the intertwined nanosheets structure was transformed to uniform particles structure. A strengthening of Al and O bonds, and suppressing Zn and O bonds, as the Al doping ratios increased, which was revealed the growth mechanism of AZO film at a deposition temperature of 400°C. All AZO films showed a high transmittance exceeding 85% within the visible range. Remarkably, the highest value of first-order reaction rate and high degradation efficiency were achieved at 2 wt% Al doped ZnO film, which are expecting it to be a promising candidate for potential photocatalytic applications.

## 3.5 Influence of thermal annealing on the properties of AZO film

### 3.5.1 Experiment conditions

Firstly, AZO film with 300 nm thickness was fabricated by mist CVD method. The deposition condition of AZO film was described in Table 3.2. Following the deposition, the obtained AZO films were vacuum annealed at 700 °C for 1 hour in the conventional furnace.

The photodegradation measurement of annealed AZO film was carried out. The condition of degradation measurement was described in section 3.4.1 in detail. The structural, optical, and photocatalytic properties of AZO films were investigated.

### 3.5.2 Results and Discussion

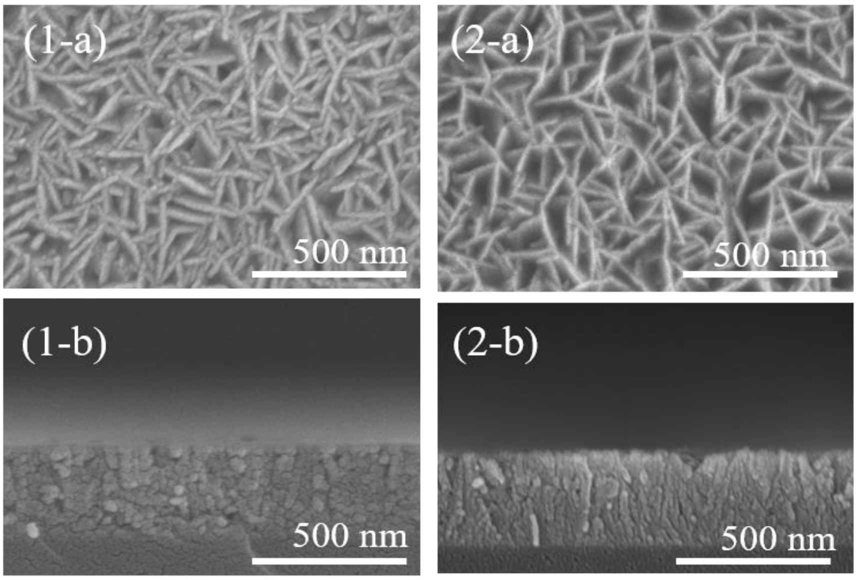

Fig. 3.18. SEM images of (1) as-deposited AZO film and (2) annealed AZO film with 300 nm thickness :(a) top view and (b) cross-section view.

Fig. 3.18 shows the SEM images of AZO films before annealing and after annealing process. It can be seen that the intertwined nanosheet structure was not changed after the annealing process. The aspect ratio of AZO nanosheets was changed from 3.77% to 7.31 % due to the increased length and the decreased width. Highest aspect ratio of nanosheets and most columnar structure were obtained at annealed AZO films. The results indicated that the crystallinity of AZO films was improved after the annealing process.

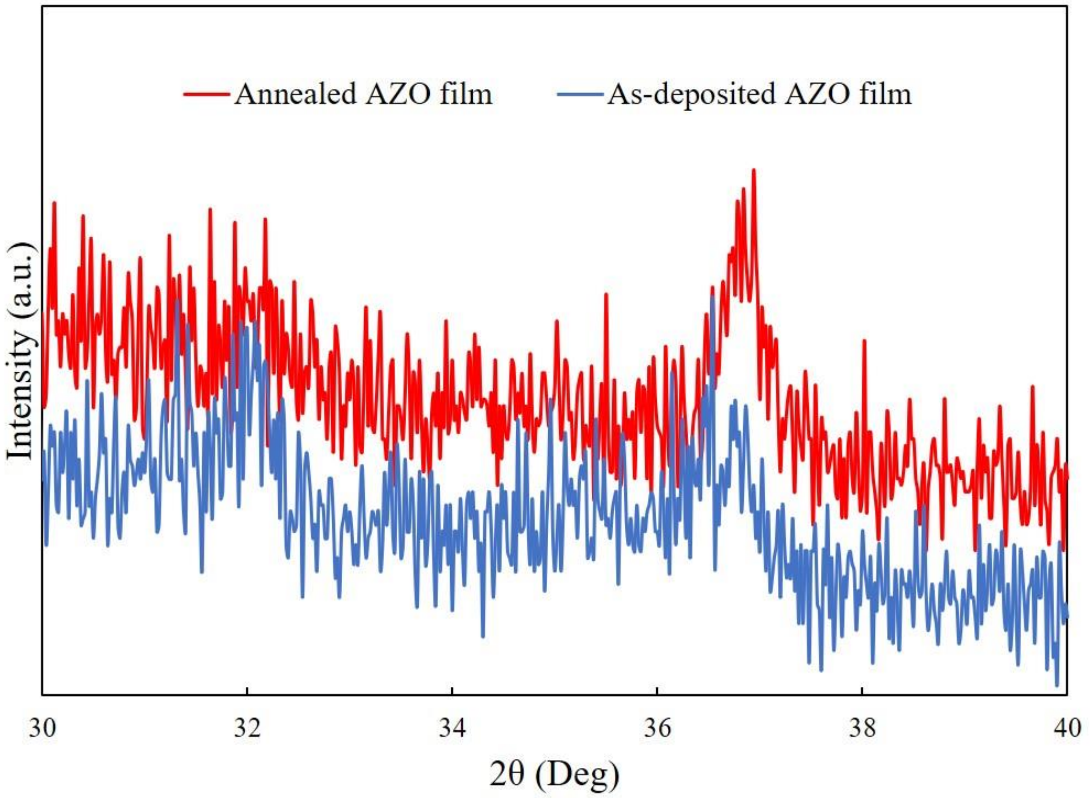

Fig. 3.19**.** 2 theta patterns of as-deposited and annealed AZO films with 300 nm thickness

Fig. 3.19 illustrates the XRD patterns of obtained AZO films before and after the annealing process. The diffraction patterns reveal distinct peaks corresponding to the (100) and (101) crystal planes. Notably, the (101) peak is the dominant peak in both AZO films, indicating a strong preference for growth along the (101) crystal plane. Following the annealing process, a obvious enhancement in the intensity of the (101) peak is observed, suggesting a significant improvement in the crystallinity of the AZO films after annealing.

Fig. 3.20 shows the Raman spectra of AZO films before annealing and after annealing process. There was a single dominant peak at around 440 cm$^{-1,}$ which corresponds to the standard peak of ZnO. The E2 peak of annealed AZO film was doublet of the as-deposited AZO film, which meant that the enhanced crystallinity of AZO films was achieved after the annealing process, which is consistent with XRD results.

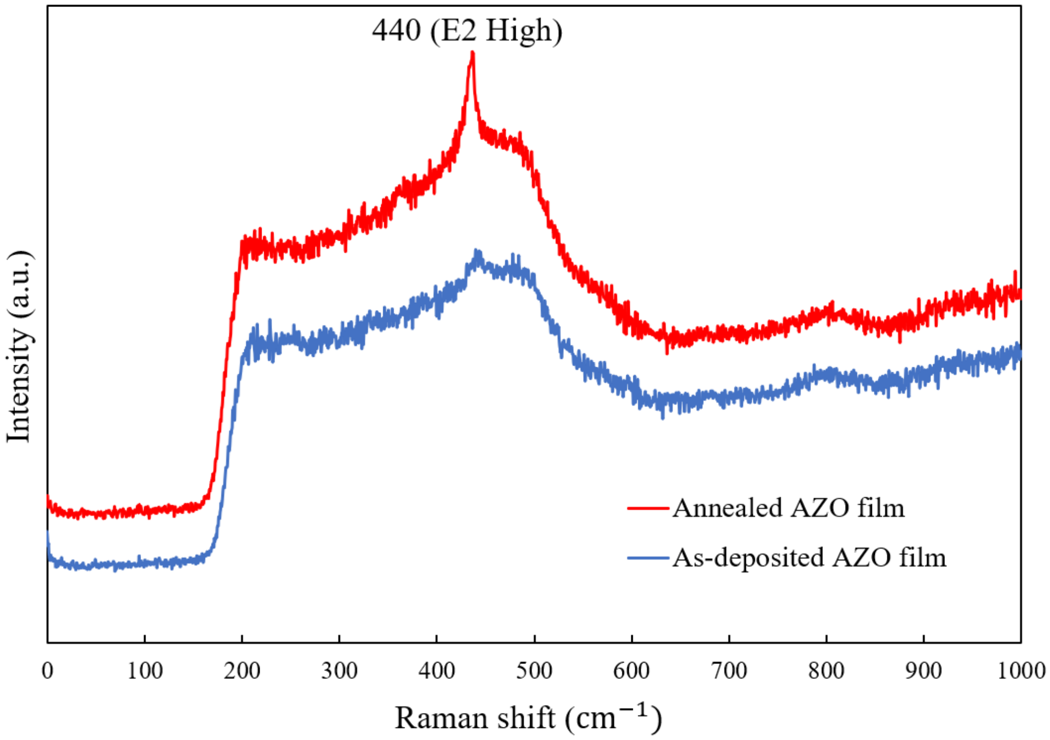

Fig. 3.20. Raman spectra of as-deposited and annealed AZO films with 300 nm thickness.

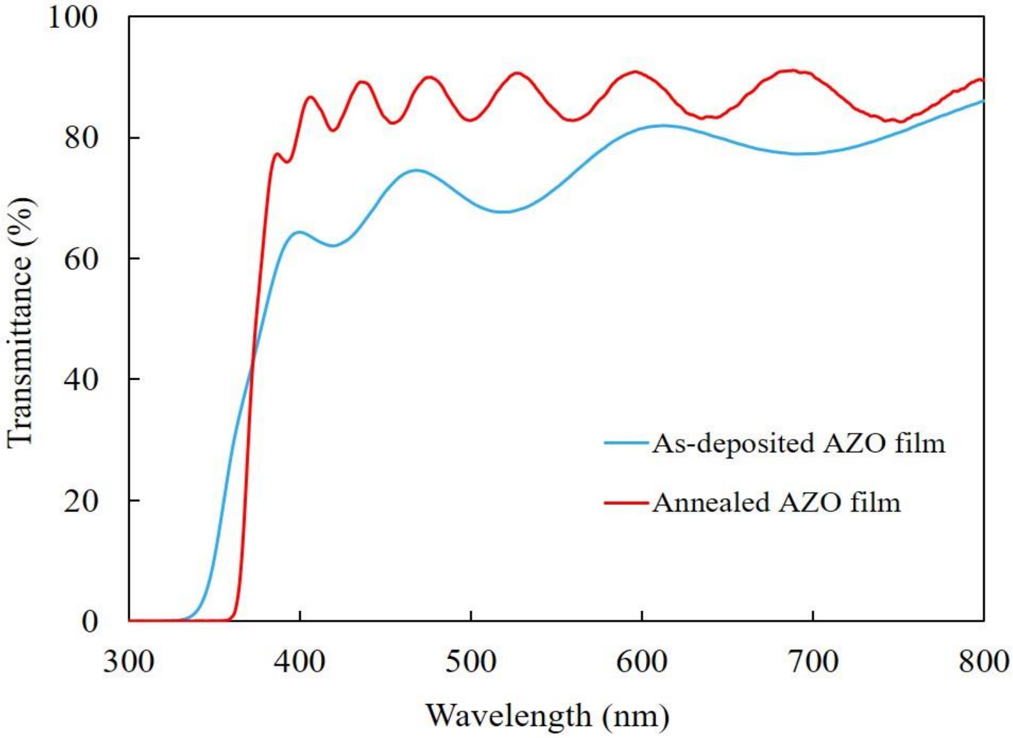

Fig. 3.21. Transmission spectra of as-deposited and annealed AZO films with 300 nm thickness.

The optical transmittance of as-deposited AZO film and annealed AZO film are shown in Fig. 3.21. The high transmittance of around 80% was obtained for all AZO films in the visible region. After annealing process, transmittance of AZO film was increased from 71 to 83%.

### 3.5.3 Conclusions

The effect of thermal annealing on the properties of AZO film was investigated, the photocatalytic property was investigated as well. The length and width of the intertwined nanosheet structure were changed after the annealing process. The most columnar structure of AZO film was obtained at annealed AZO film. The intensity of the (101) peak was increased at annealed AZO film, which was pointed that the enhancement of crystallinity after the thermal annealing process. The transmission spectra of AZO film were significantly increased to around 80% after the annealing process. The highest photodegradation efficiency was obtained at annealed AZO film and the highest degradation rate was 0.0041 $\mathrm{min}^{-1}$.

## 3.6 References

[1] D.S. Bhatkhande, V.G. Pangarkar, A.A.C.M. Beenackers. J. Chem. Technol. Biotechnol. 77 (2001) 102.

[2] C. Minero, E. Pelizzatti, M. Sega, S.E. Friberg, J. Sjoblom. J. Dispersion. Sci. Technol. 20 (1999) 643.

[3] M. Kanemoto, T. Shiragami, C. Pac, S. Yanagida, M. Kanemoto, T. Shiragami, C. Pac. J. Phys. Chem. 96 (1992) 3521.

[4] K. Vanheusden, W.L. Warren, C.H. Seager, D.R. Tallant, J.A. Voigt, B.E. Gnade. J. Appl. Phys. 79 (1996) 7983.

[5] C. Baratto, E. Comini, M. Ferroni, G. Faglia, G. Sberveglieri. Crystengcomm. 15 (2013) 7981.

[6] D. Gaspar, L. Pereira, K. Gehrke, B. Galler, E. Fortunato, R. Martins. Sol. Energy. Mat. Sol. C. 163 (2017) 255.

[7] B.K. Meyer, H. Alves, D.M. Hofmann, W. Kriegseis, D. Forster, F. Bertram, J. Christen, A. Hoffmann, M. Strassburg, M. Dworzak. Phys. Status. Solidi. 241 (2004) 231.

[8] S, Mukhopadhyay, P.P. Das, S. Maity, P. Ghosh, P.S. Devi. Appl. Catal. B-Environ. 615 (2015) 128.

[9] J. Tauc. Mater. Res. Bull. 3 (1968) 37.

[10] Y.S. Seo, S.G. Oh. Korean. J. Chem. Eng. 36 (2019) 2118.

[11] R. Ebrahimi, K. Hossienzadeh, A. Maleki, R. Ghanbari, R. Rezaee, M. Safari, B. Shahmoradi, H. Daraei, A. Jafari, K. Yetilmezsoy. J. Environ. Health Sci. Eng. 16 (2019) 479.

[12] F. Yu, B. Wang, H. Hu, H. Li, T. Song, B. Xu, L. He, H. Duan, S. Wang. Phys. Status Solidi. 216 (2019) 1900386.

[13] S. Mukhopadhyay, P. P. Das, S. Maity, P. Ghosh, P. S. Devi. Appl. Catal. B Environ. 165 (2015) 128.

[14] J.-K. Jeong, H.-J. Yun, S.-D. Yang, E.-Y. Eom, S.-W. Chea, J.-H. Park, H.-D. Lee, G.-W. Lee. Thin. Solid. Films. 638 (2017) 89.

[15] N. Kaneva, I. Stambolova, V. Blaskov, Y. Dimitriev, A. Bojinova, C. Dushkin. Surf. Coat. Technol. 207 (2011) 5.

[16] Y. Wang, X. Zhang, L. Bai, Q. Huang, C. Wei, Y. Zhao. Appl. Phys. Lett. 10 (2012) 263.

[17] S.H, Jeong, G.C. Park, J.H. Choi, C.M. Lee, S.M. Lee, T.Y. Seo, D.H. Choi, S.B. Jung,

J.H. Lim, J. Joo. J. Nanosci. Nanotechnol.16 (2016) 11272.

[18] T. P. Rao, M. C. Santhoshkumar. Appl. Surf. Sci. 255 (2009) 7212.

[19] A. L. Patterson. Phys. Rev. 56 (1939) 978.

[20] M. Ramya, T.K. Nideep, V.P.N. Nampoori, M. Kailasnath. Sci. Report. 11(2021) 6159.

[21] T. Kawaharamura, T. Uchida, M. Sanada, M. Furuta. AIP Adv. 3 (2013) 032135.

[22] M. Ramya, T. K. Nideep, V. P. N. Nampoori, M. Kailasnath. Sci. Rep. 11 (2021) 6159.

[23] T.P. Rao, M.C. Santhoshkumar. Appl. Surf. Sci. 225 (2009) 7212.

[24] I. Langmuir. J. Am. Chem. Soc. 38 (1916) 2221.

[25] S. B. Kim, S. C. Hong. Appl. Catal. B Environ. 35 (2002) 305.

[26] S. Loghambal, A. J. A. Catherine, S. V. Subash. Int. J. Math. Appl. 6 (2018) 903.

[27] M. Golshan, M. Zare, G. Goudarzi, M. Abtahi, A.A. Babaei. Mater. Res. Bull. 91 (2017) 59.

# Chapter 4

# Influence of AZO seeds layer on the control of growth and crystallinity of AZO films

## 4.1 Introduction

Regarding the fabrication of AZO thin films through the mist CVD method, a notable challenge remains in achieving AZO films with the high crystallinity and controllable growth direction. In our prior investigations, we successfully deposited AZO thin films with high crystallinity utilizing an RF magnetron sputtering system [1]. This approach is advantageous for generating reproducible and uniform AZO thin films on large-area substrates, even at lower deposition temperatures. The high-energy ejected species during the sputtering process enhance the crystalline quality of films [2-10]. Furthermore, we synthesized AZO films with a large surface area in the previous chapter utilizing an innovative mist CVD method. It had the advantages for film deposition, including large surface area, uniformity, reproducibility, simplicity, ease of control, and cost-effectiveness [10-14].

This chapter proposes a hybrid methodology combining mist CVD process with the RF magnetron sputtering method. This synergistic approach aims to achieve AZO films with high crystallinity and controllable growth direction. Simultaneously, we will explore the photodegradation efficiency, further enhancing their applicability in photocatalytic processes.

## 4.2 Influence of AZO seeds layer on the properties of AZO films

### 4.2.1 Experiment conditions

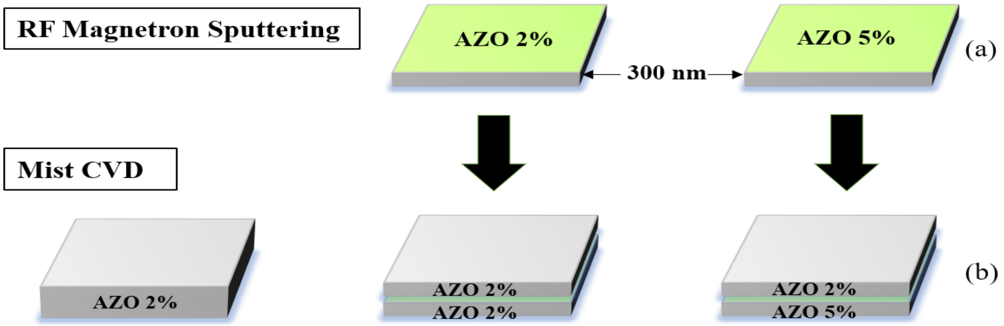

Fig. 4.1 Sketch of (a) as-deposited AZO films with varied Al ratios, and (b) deposition of double-layered AZO films on different substrates.

Fig. 4.1 (a) illustrates the process of depositing AZO thin films (300 nm-thick) onto glass substrates using an RF (13.56 MHz) magnetron sputtering process. The glass substrate was preheated at 150°C for a duration of 1 hour, prior to sputtering process. Pure argon (30 sccm) is served as the working gas, which was controlled by a mass controller during the deposition process. The deposition power and pressure are kept at 180 W and 7 Pa, respectively. The comparison is made between the AZO target with AZO-2wt% and AZO-5wt%.

After the deposition process, as-deposited AZO-2wt% and AZO-5wt% films are utilized as seed layers for the subsequent deposition of AZO films (300 nm-thick) using the mist CVD process, as depicted in Fig. 4.1 (b). To study the influence of the seed layer, 600 nm-thick AZO film is directly deposited onto bare glass using the mist CVD method. During the deposition process, the substrate is placed within the FC reactor and maintained at 400°C. The thicknesses of the three AZO films are equivalent to 600 nm. Detailed deposition parameters for the AZO films are comprehensively outlined in Table 4.1.

Table 4.1. Deposition conditions of double-layered AZO films by the mist CVD method.

| Solute | Zinc acetate, Aluminum acetylacetonate |
|---|---|
| Solvent | Methanol, $H_2$O |
| Concentration of zinc source(mol/L) | 0.04 |
| Concentration of aluminum source(mol/L) | 0.02 |
| Substrate | Glass, AZO 2 wt%, AZO 5 wt% |
| Deposition Temperature (°C) | 400 |
| Carrier gas, Flow rate (L/min) | Nitrogen , 2.5 |
| Dilution gas, Flow rate (L/min) | Nitrogen , 4.5 |

### 4.2.2 Results and Discussion

Fig. 4.2 shows the SEM images of the as-deposited AZO-2 wt% and AZO-5 wt%. The uniform surfaces of both AZO films were obtained. A spherical morphology was displayed for these as-deposited AZO films with average grain sizes of 74 nm for AZO-2wt% and 104 nm for AZO-5wt% films. Both as-deposited AZO films exhibited columnar structures that grew vertically to the glass substrates, which can be seen in cross-sectional view. The most columnar structure was found from the AZO-5wt% film.

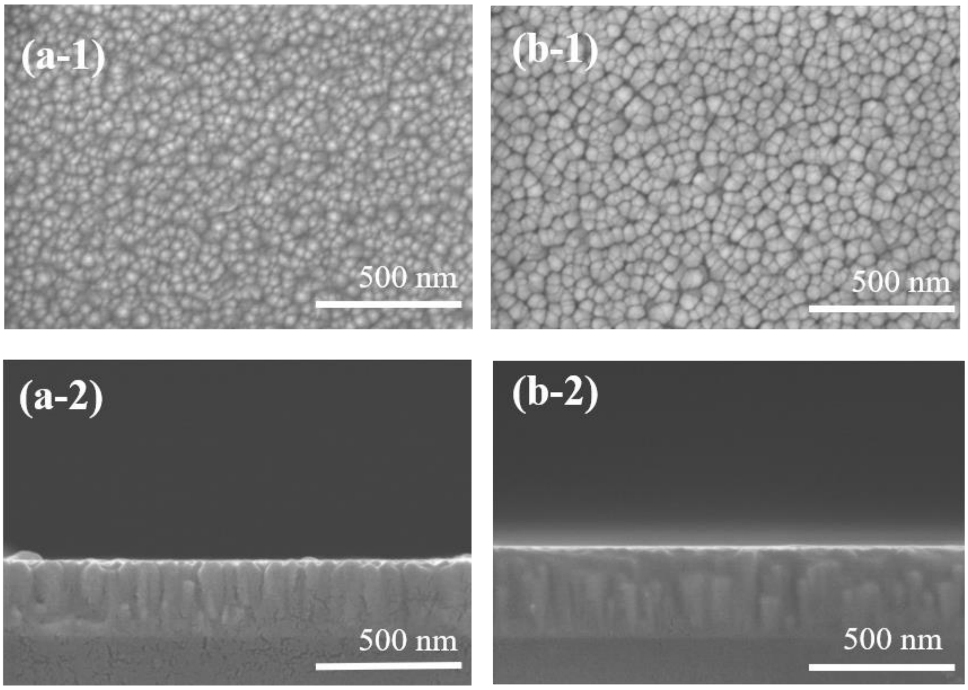

Fig.4.2 SEM images of as-deposited AZO films with varied Al doping ratios :(a) 2 wt% Al, and (b) 5 wt% Al; (1) top view, and (2) cross view.

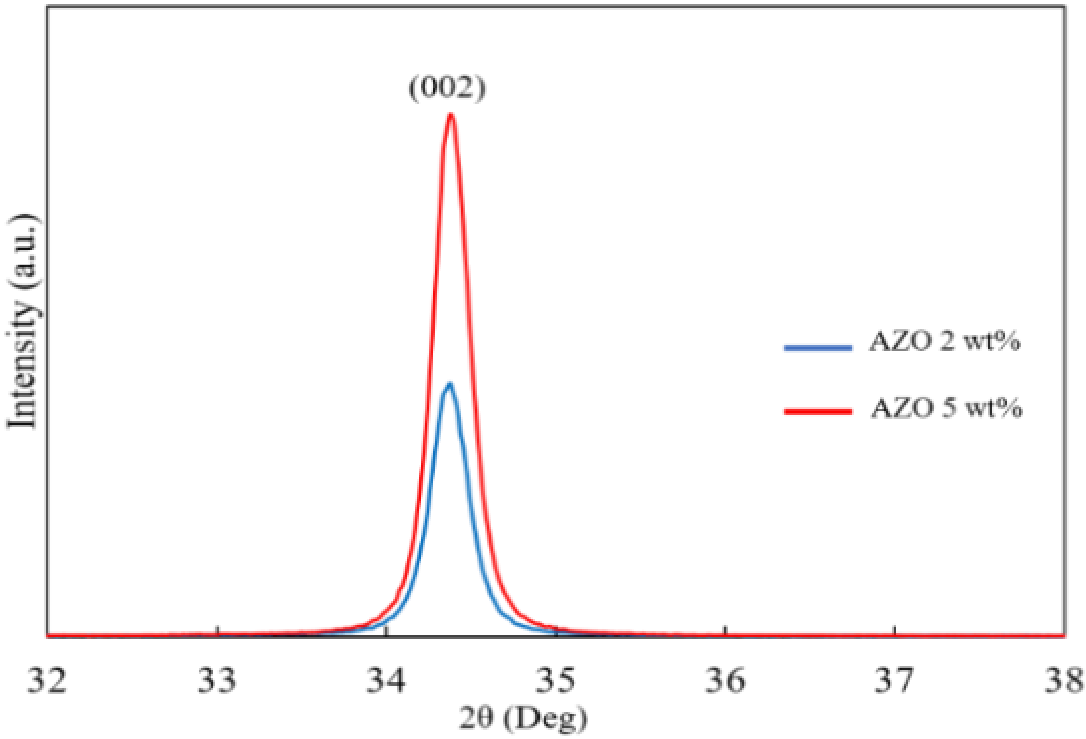

Fig.4.3 2 theta patterns of as-deposited AZO films with varied Al doping ratios.

The XRD patterns of the as-deposited AZO-2wt% and AZO-5wt% are presented in Fig. 4.3. It can be confirmed that both AZO films showed a single dominant peak corresponding to the (002) crystal plane. This finding indicates that the obtained as-deposited AZO films showed the preferred growth orientation of the AZO was (0001) crystal plane, which was perpendicular to the substrates. Furthermore, higher intensity of (002) peak with smaller FWHM of 0.24° were obtained at AZO-5wt% film. The calculated c-axis crystallite size of the AZO-5wt% film was determined to be 35.15 nm, which is notably greater than the 19.95 nm observed in the AZO-2wt%. Accordingly, the highest crystallinity was obtained at AZO-5wt% film.

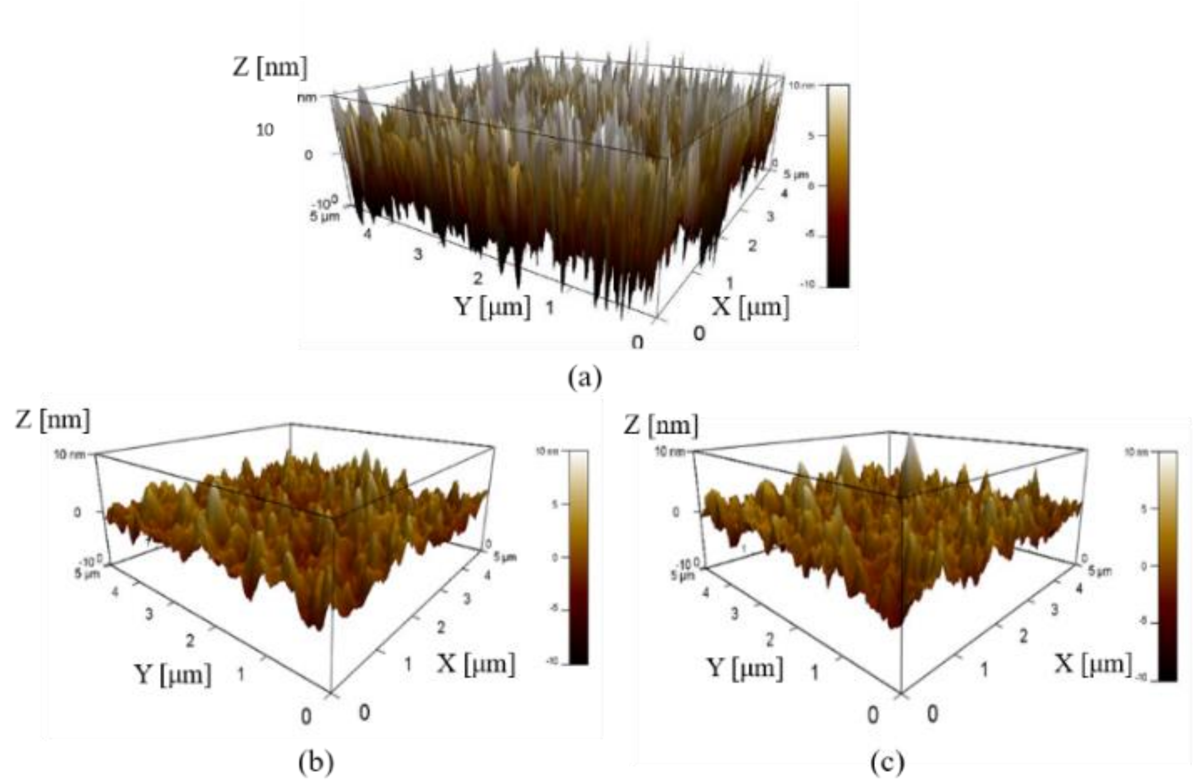

Fig. 4.4 AFM images of double-layered AZO films fabricated by mist CVD: (a) AZO/Glass, (b) AZO/AZO-2wt%, and (c) AZO/AZO-5 wt%.

In Fig. 4.4, the AFM images exhibit the AZO films deposited on different substrates using the mist CVD method. Remarkable differences emerged in the RMS surface roughness values for AZO films deposited employing distinct AZO seed layers. Specifically, the AZO/AZO-2wt% film obtained a significantly reduced value of 4.13 nm, while the AZO/AZO-5wt% film showed an even lower value of 3.76 nm. Furthermore, calculating the surface area, the AZO/AZO-5wt% film measured at 23.5 m²/g, surpassing that of the AZO/AZO-2wt% film at 11.2 m²/g. These findings underscored that the AZO/AZO-5wt% films achieved the large surface area and smaller surface roughness.

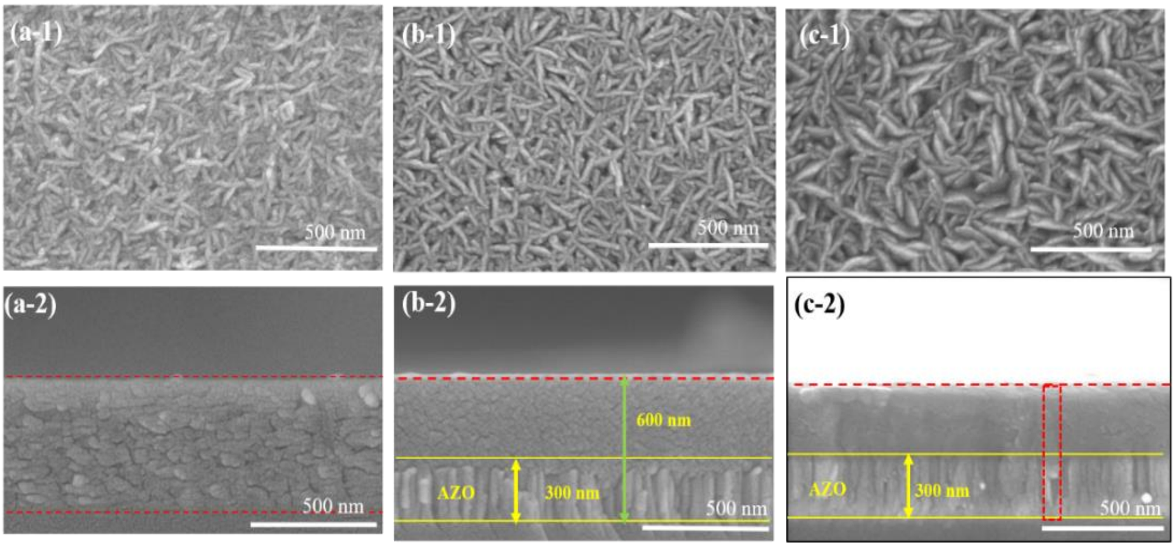

Fig. 4.5 SEM images of double-layered AZO films fabricated by mist CVD: ((a) AZO/Glass, (b) AZO/AZO-2 wt%, (c) AZO/AZO-5 wt%, (1) top view, and (2) cross-section view)

Fig. 4.5 shows SEM images of AZO films deposited on different substrates through the mist CVD method. When viewed from the top, the images reveal well-defined intertwined nanosheet structures that exhibit remarkable uniformity across all substrates. The average diameters of these AZO nanosheets were measured at 16 nm, 27 nm, and 51 nm, for the sequence of AZO/glass film, AZO/AZO-2 wt% film and AZO/AZO-5wt% film.

In the cross-sectional view of Fig. 4.5 (a-2), a randomly growth was appeared on the glass substrate. Nevertheless, a distinct alteration in the growth direction of the nanosheets was observed when deposited on the AZO substrates. Notably, the most columnar structure was achieved from the AZO/AZO-5wt% film.

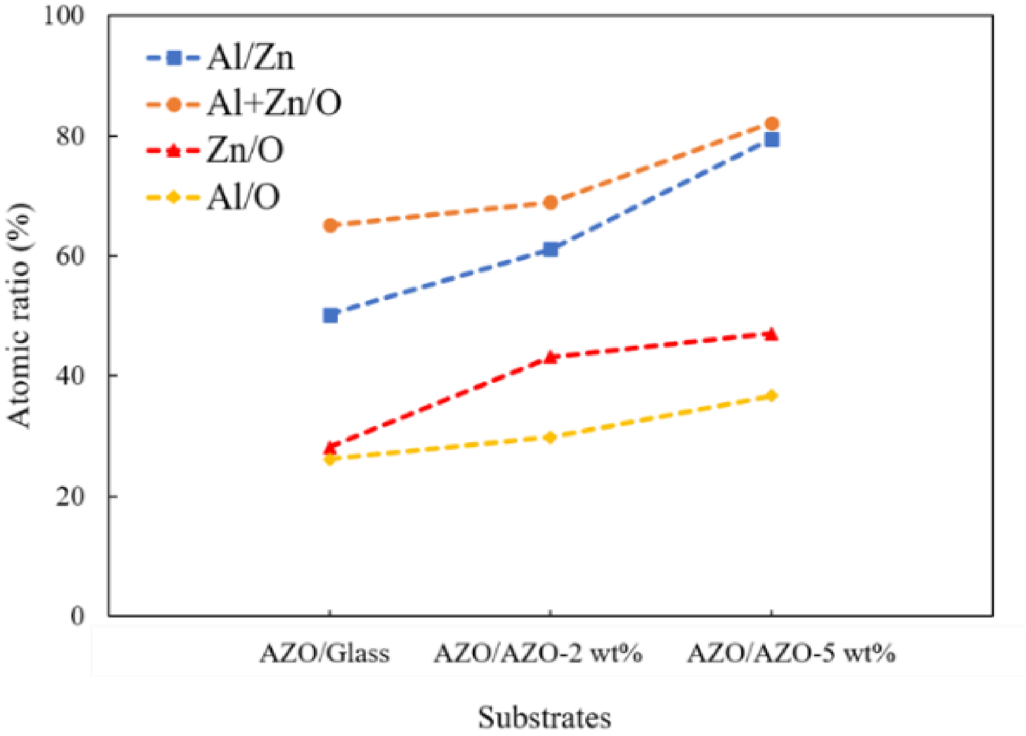

Fig. 4.6 Atomic ratios variation of Zn, Al, and O calculated from EDX measurements for double-layered AZO films fabricated by mist CVD.

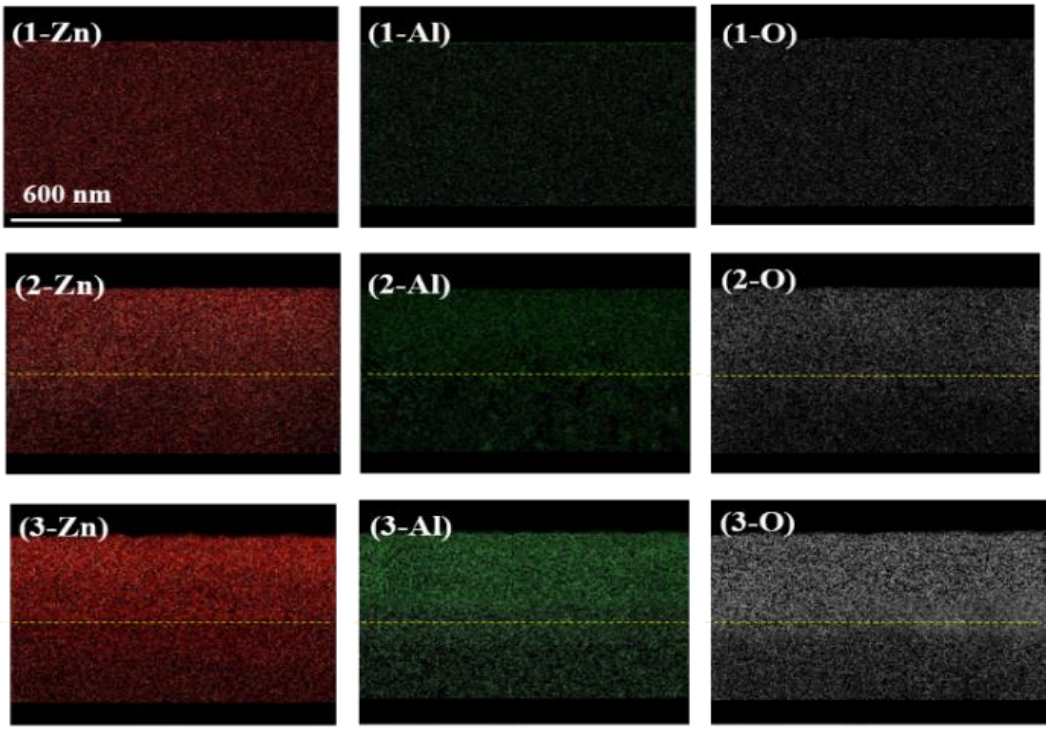

Fig. 4.7 EDS mapping analyses of the double-layered AZO films fabricated by mist CVD; (1) AZO/Glass, (2) AZO/AZO-2wt%, (3) AZO/AZO-5wt%.

Fig. 4.6 describes EDX measurements of deposited AZO films after the mist CVD process, which was highlighting the atomic variations of Zn, Al, and O. Remarkably, the deposited AZO films on the AZO seed layers displayed increased atomic ratios of Al/Zn, indicative of increased incorporation of Al into the AZO films. This trend was indicated by the substantial 80% difference in the atomic ratios of Al/Zn for the AZO/AZO-5wt% film compared to 60% for the AZO/AZO-2wt% film. EDX mapping supported these findings, illustrating the high concentrations of Zn, Al, and O in instances where AZO seed layers were applied as substrates.

From Fig. 4.7 (2) and (3), during the mist CVD process, increased Al doping in ZnO films enhanced the concentration of each element progressively from the bottom side to the top side. This observation was aligned with the results presented in Fig. 4.6, emphasizing that AZO films deposited on AZO seed layers exhibited significant increase in atomic ratios of (Al+Zn)/O compared to those on glass. The increasing atomic ratios indicated the improvement in crystalline quality facilitated by utilizing AZO seed layers.

Moreover, in direct comparison with the AZO/AZO-2wt% film, the AZO/AZO-5wt% film exhibited increased atomic ratios of Zn/O and Al/O. Notably, the atomic ratio of Zn/O was predominant in the AZO/AZO-5wt% film, signifying high crystallinity compared with AZO/AZO-2wt% film.

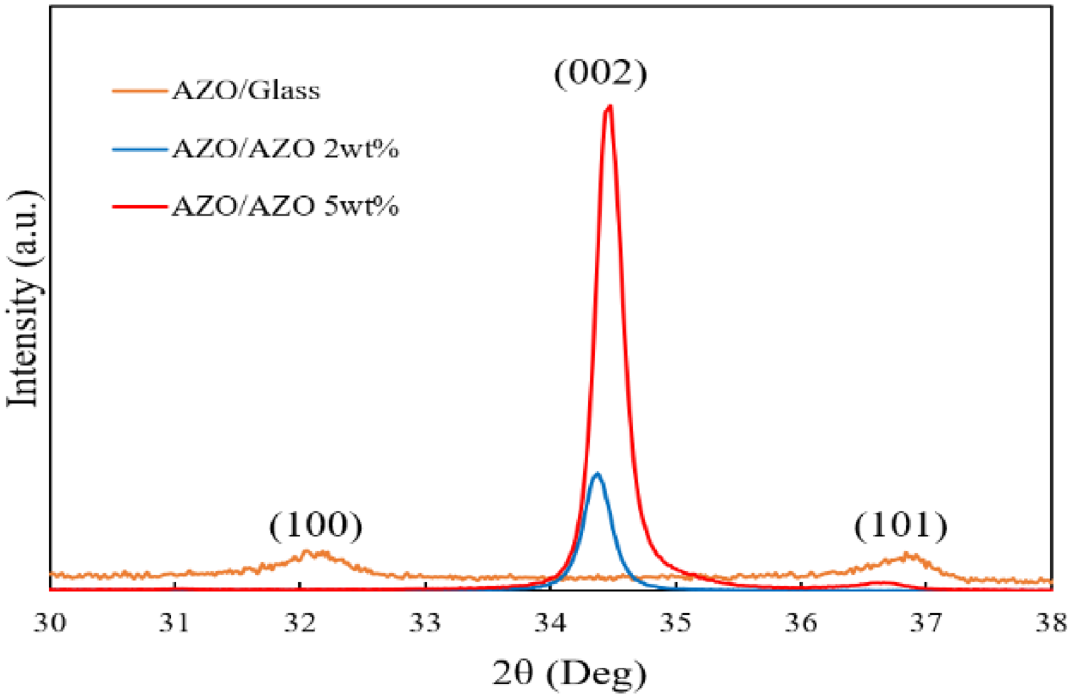

Fig. 4.8 2 theta patterns of the double-layered AZO films fabricated by mist CVD.

Fig. 4.8 shows the XRD patterns of AZO films deposited on different substrates following the mist CVD method. Both AZO/AZO-2wt% and AZO/AZO-5wt% films exhibited distinct (002) and (101) diffraction peaks. It was indicated that the dominant diffraction (002) peak was corresponded to a preferred orientation along the (0001) crystal plane for both obtained AZO films. Notably, the intensity of the (002) peak at AZO/AZO-5wt% film was considerably higher than AZO/AZO-2wt% film. Calculation of the crystallite size along the c-axis revealed that the large crystallite size (37.28 nm) was achieved at AZO/AZO-5wt% films when compared with AZO/AZO-2wt% film (22.15 nm). The enhanced crystallinity observed in the AZO/AZO-5 wt% film, indicated significant influence of seed layer crystallinity on the resulting crystalline quality of deposited AZO films.

Importantly, no (002) diffraction peak was observed from the deposited AZO/Glass. This observation meant during the mist CVD process, AZO seeds layers could effectively control the growth orientation of AZO films. To explore influence of crystallinity on the AZO seed layer, the calculated lattice mismatch [15] between the as-deposited AZO-5wt% film and the AZO/AZO-5wt% film was determined to be 0.07%, a value lower than the lattice mismatch between the as-deposited AZO-2wt% film and the AZO/AZO-2wt% film (0.13%). These findings imply that the AZO/AZO-5wt% film maintained the similar orientation as the AZO-5wt% seeds layer, highlighting improved crystallinity within the seed layer could be contributed to the growth orientation of the subsequent AZO films.

The dislocation density ($\delta$) [16] was evaluated the density of defect states from the obtained AZO/AZO-2 wt% and AZO/AZO-5wt% films, which are expressed in Eq. (1).

$$\delta = 1/D \tag{1}$$

As Al doping concentration increased, the calculated dislocation density decreased, indicating a reduction in lattice imperfections and increased crystallite sizes, which attributed to enhanced crystallinity in the AZO films.

Furthermore, referring to Table 4.2, the peak position (002) of AZO/AZO-2wt% shifted from 34.21° to 34.42°, and for AZO/AZO-5wt% films, the shift was from 34.27° to 34.48°. This shift showed that during mist CVD process, higher concentration of Al from underneath AZO seed layer was incorporated into the AZO film. The substitution of Al$^{3+}$ ions for Zn$^{2+}$ ions in the ZnO lattice site leads to changes in peak position due to the differing ionic radii of Al$^{3+}$ (0.053 nm) and Zn$^{2+}$ (0.075 nm) [17].

Table 4.2. XRD analysis data of double layered AZO films fabricated by mist CVD method

| AZO Films | Peak Position (Deg) | (hkl) | d (nm) | Lattice Parameters (nm) | | Stress (GPa) | C-axis crystallite size (nm) |
|---|---|---|---|---|---|---|---|
| | | | | a | c | | |
| AZO (2wt%) | 34.21 | (002) | 2.6224 | 0.3231 | 0.5229 | -3.3807 | 19.92 |
| AZO/AZO (2wt%) | 34.43 | (002) | 2.6019 | 0.3246 | 0.5216 | 0.1934 | 22.15 |
| AZO (5wt%) | 34.28 | (002) | 2.6125 | 0.3234 | 0.5211 | -1.6555 | 35.14 |
| AZO/AZO (5wt%) | 34.49 | (002) | 2.5966 | 0.3253 | 0.5204 | 1.1152 | 37.28 |

In order to explore the influence of the AZO seed layer on the growth of AZO films during the mist CVD process, the lattice mismatch between the AZO film and the underlying AZO seed layer was conducted. The lattice mismatch calculations revealed that the mismatch between the as-deposited AZO-5wt% film and the AZO/AZO-5wt% film was remarkably low at 0.07%. This value was significantly smaller than the mismatch observed between the as-deposited AZO-2wt% film and the AZO/AZO-2wt% film (0.13%), which indicated that, as the Al concentration increased, the lattice constants closely approached those of bulk ZnO. The results suggested that the AZO/AZO-5wt% film achieved a low lattice mismatch, indicating that preferred orientation during the AZO deposition in the mist CVD process was consistent with that of the AZO-5wt% seed layer.

The observation further confirms that using AZO seed layers contributes to improving growth orientation along the (0001) crystal plane of AZO films. Consequently, the result can attribute as a critical factor for attaining the columnar structure and improved crystallinity for the AZO/AZO-5wt% film. Considering the growth direction of the as-deposited AZO thin films deposited by the RF magnetron sputtering process, it was evident that ZnO crystal growth strongly preferred the (0001) direction due to its lower bonding energy compared to other growth directions [18]. In the mist CVD process, according to the following equations;

$$Zn\,(CH_3COO)_{2(g)} \xrightarrow[\blacktriangle]{400^{\circ}C} Zn_{(s^*)} + 2CH_3COO_{(g)} \tag{2}$$

$$H_2O_{(g)} \rightarrow 2H_{(s^*)} + O_{(s^*)} \tag{3}$$

$$CH_3COO_{(s^*)} + H_{(s^*)} \rightarrow CH_3COOH_{(g)} \tag{4}$$

$$Zn_{(s^*)} + O_{(s^*)} \rightarrow ZnO_{(s)} \tag{5}$$

The mist CVD process involved the generation of mist droplets from a mixed precursor solution containing ZA and AA. These mist droplets were subsequently directed into the reactor, where the preferred substrate was maintained at 400°C. During the deposition process, the decomposition temperature of ZA exceeded 237°C, leading to the release of zinc ions through the mist droplets.

Under the mist CVD process, the decomposed Zn ions in the mist droplets on the surface of the AZO seed layer engaged in a reaction with the oxygen atoms at ZnO nuclei sites. This interaction resulted in the growth orientation of the newly formed ZnO crystals aligning with the (0001) crystal plane of the underlying AZO seed layer. This phenomenon facilitated the promotion of better crystallinity and enhanced growth orientation within the resulting AZO film.

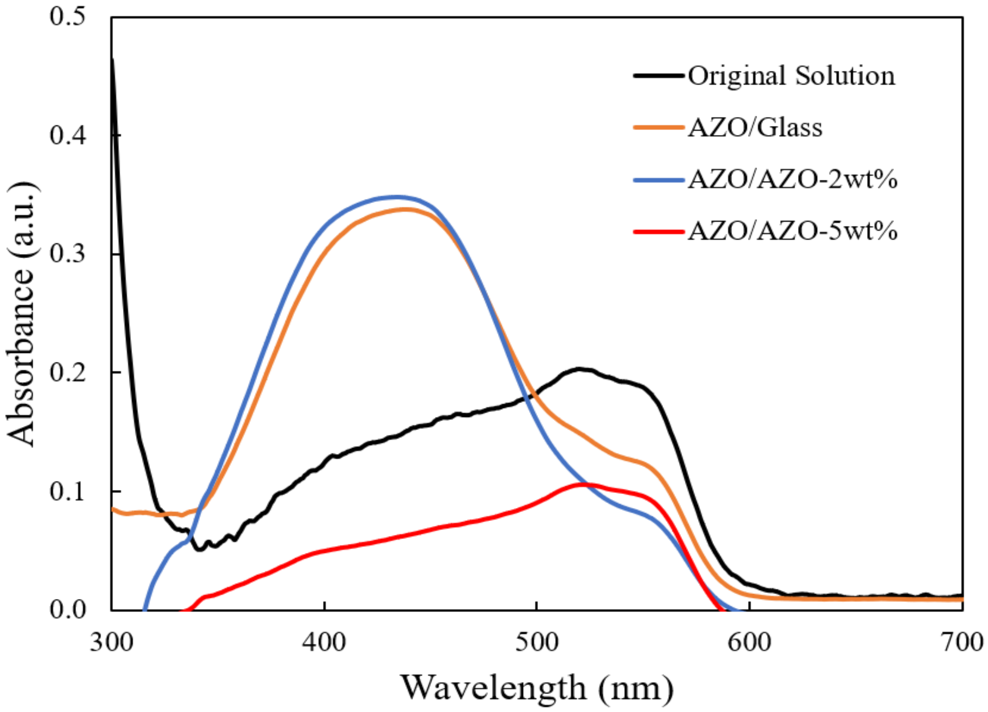

Fig.4.9 The absorption spectra of MR solution for the double-layered AZO films fabricated by mist CVD.

Fig. 4.9 illustrated the absorption spectra of the MR solution for deposited AZO films on different substrates. Original MR solution exhibited a decrease in absorption intensity with irradiation time, where a lower absorption intensity correlated with higher photocatalytic efficiency. Notably, the absorption intensities of AZO films deposited on the glass substrates were greater than those deposited on AZO seeds layers, indicating a significant influence of the AZO seed layer on the photocatalytic performance of the AZO film.

Comparing the AZO/AZO-2wt% film, the decreased absorption intensity of AZO/AZO-5wt% film exhibited a slight decrease, suggesting an enhancement in photocatalytic efficiency. The lowest absorption intensity was observed at AZO/AZO-5wt%, indicating high photocatalytic efficiency, which was shielded a range from 340nm to 700nm, indicating improved photodegradation efficiency in the ultraviolet and visible regions.

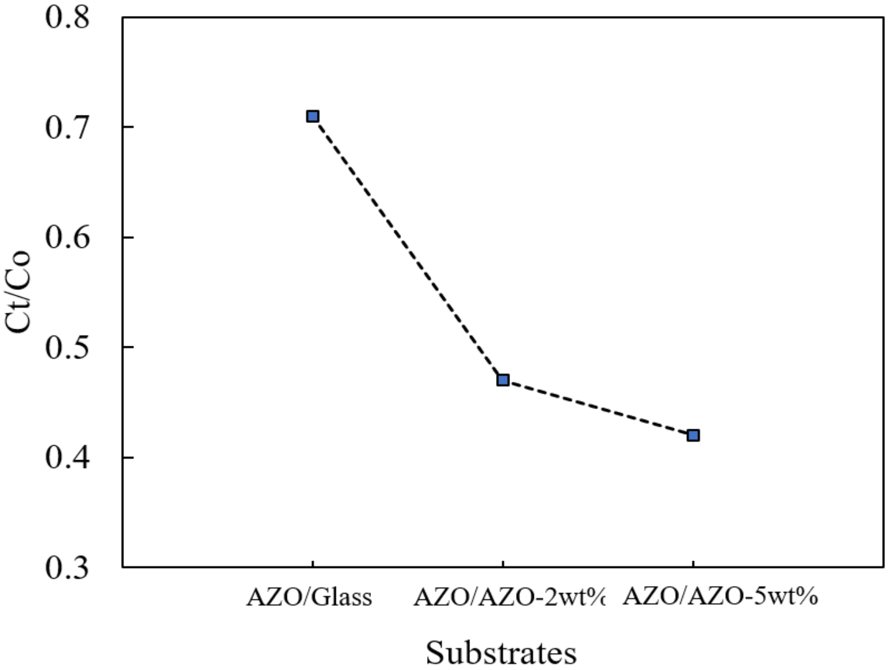

Fig. 4.10 Plot of $C_t$/Co versus the different substrates for the double-layered AZO films fabricated by mist CVD.

In Fig. 4.10, the plot of Ct/Co is illustrated, showing the concentration variation over the course of MR solution degradation. After photodegradation process, a decrease concentration in MR solution signifies higher photocatalytic efficiency. Notably, the deposited AZO films on AZO seed layers achieved lower MR solution concentrations in comparison to those on glass substrates. Among them, the AZO/AZO-5wt% film demonstrated most notable reduction in MR solution concentration, highlighting its exceptional photocatalytic performance.

Based on the L-H model [19], the calculated degradation reaction rates for the AZO/Glass was 0.0015 $\text{min}^{-1}$. Particularly, these rates increased to 0.0041 $\text{min}^{-1}$ for the AZO/AZO-2wt% film and further to 0.0043 $\text{min}^{-1}$ for the AZO/AZO-5wt% film. Remarkably, the highest first-order degradation reaction rate was achieved at AZO/AZO-5wt% film, which signifying its superior photocatalytic performance.

### 4.2.3 Conclusions

During the mist CVD process, the utilization of as-deposited AZO seed layers proved effective in controlling the growth and crystallinity of the subsequently deposited AZO films. The enhanced crystallinity in the AZO film fabricated via mist CVD was contributed by the crystallinity of underneath AZO seeds layer. The low lattice mismatch between the AZO film and seed layer facilitated the vertical alignment of the AZO film. Particularly noteworthy is exceptional performance of deposited AZO film on the as-deposited AZO-5wt% seed layer, showcasing high crystallinity and a substantial surface area. Additionally, a positive correlation between the aluminum doping ratio and AZO film crystallinity was observed. The growth mechanism underlying the AZO film on the AZO seed layer has been elucidated, highlighting the alignment of the deposited AZO film with the (0001) orientation of the underlying AZO seed layer.

## 4.3 References

[1] C. Li, M. Furuta, T. Matsuda, T. Hiramatsu, H. Furuta. T. Hirao. Thin Soli. Film. 517 (2009) 3265.

[2] M. Kanemoto, T. Shiragami, C. Pac, S. Yanagida, M. Kanemoto, T. Shiragami, C. Pac. J. Phys. Chem. 291 (1992) 3521–3526.

[3] D. Gaspar, L. Pereira, K. Gehrke, B. Galler, E. Fortunato, R. Martins. Sol. Energy Mat. Sol. C. 163 (2017) 255–262.

[4] J.C. De Almeida, M.T. Correa, R.H. Koga, D.M.S. Delduque, O.F. Lopes, G.T.S.T. Dasilva, C. Ribeiro, V.R.D. Mendonca. New. J. Chem. 42 (2020) 18216-18224.

[5] J.G. Mahy. L. Lejeune, T. Haynes, N. Body, S.D. Kreijger, B. Elias, R.H.M. Marcilli, C.A. Fustin, S. Hermans. Catalysts. 11 (2021) 1182-1199.

[6] B.K. Meyer, H. Alves, D.M. Hofmann, W. Kriegseis, D. Forster, F. Bertram, J. Christen, A. Hoffmann, M. Strassburg, M. Dworzak. Phys. Status Solidi. 241 (2004) 231–260.

[7] N. Ahammed, M.S. Hassan, M. Hassan. Mater. Sci. 36 (2018) 419–426.

[8] T. Zhang, F. Meng, Y. Cheng, N. Dewangan, G.W. Ho, S. Kawi, S. Z. Applied. Catal. B. Environ. 286 (2021) 119853-119866.

[9] T. Zhang, F. Meng, M. Gao, W.L. Ong, K.G. Haw, T. Ding, G.W. Ho, S. Kawi. Ecomat. 3(2021) e12152-e12166.

[10] T. Kawaharamura. J. Appl. Phys. 53 (2014) 05FF08-05FF15.

[11] K.J. Chen, T.H. Fang, F.Y. Hung, L.W. Ji, S.J. Chang, S.J. Young, Y.J. Hsiao. Applied. Surf. Sci. 254 (2008) 5791-5795.

[12] R.I. Muhammad, R. Mukhlasur, S.F.U. Farhad, J. Podder. Surf. Interfaces. 16 (2019) 120-126.

[13] H.S. Wai. C. Li. Nanomaterials. 12 (2022) 195-210.

[14] S. Hou. C. Li. Thin. Soli. Films. 605 (2016) 37-43.

[15] T.P. Rao, M.C. Santhoshkumar. Appl. Surf. Sci. 255 (2009) 7212–7221.

[16] P.F. Fewster. Rep. Prog. Phys. 59 (1996) 1339-1407.

[17] X. Yang, J. Tian. Y. Guo, M. Teng, H. Liu, T. Li, P. Lv, X. Wang. Nanomaterials. 11 (2021) 522-529.

[18] Z. L. Wang. J. Phys. Condens. Matter. 16 (2004) R829-R835.

[19] S. Loghambal, A.J.A. Catherine, S.V. Subash. Int. J. Math. Appl. 6 (2018) 903–913.

# Chapter 5

# Synthesis and characterization of ZnO nanorods and AZO/ZnO core-shells nanorods by mist CVD method

## 5.1 Introduction

In recent times, nanostructures related with ZnO have garnered attention as effective photocatalysts for efficiently breaking down the dye pollutants in water purification processes [1-4]. Moreover, many studies have underscored the pivotal role of surface morphology and several modifications in ZnO nanostructures (spheres, rods, tubes, needles, etc.) in enhancing photocatalytic performance [5-8]. Among these, one-dimensional ZnO nanorods stand out for their superior organic dye adsorption and enhanced photocatalytic activity, owing to their high surface-to-volume ratio [9-13]. The exposed surface facets of ZnO nanorod and its photodegradation efficiency has been extensively documented [14,15]. An increased proportion of exposed polar surfaces could be enhanced the photodegradation, which attributed tendency of the (0001)-Zn polar surface to adsorb $OH^-$ ions, thus facilitating the formation of ROS species upon interaction with hydroxyl radicals, which in turn, facilitate the degradation of organic contaminants and microbial damage [16-24]. Furthermore, light absorption can be enhanced by the substantial surface area of well-aligned ZnO rods, leading an increase in production of charged carriers on the catalyst surface and consequently, an improvement in ROS species.

Based on several techniques, CBD process is an attractive method for synthesizing well-aligned ZnO nanorods due to its simplicity, cost-effectiveness, scalability, and low-temperature processing [25-28]. Notably, our earlier work has demonstrated that choosing substrates significantly impacts the controlled growth of well-aligned ZnO nanorods. Among transparent conductive oxide substrates, the vertical alignment of ZnO nanorods can be achieved by the AZO film.

Building on our prior research experience, we have successfully fabricated conductive AZO films using an RF magnetron sputtering system and fabricated well-aligned ZnO nanorods on AZO films through the CBD method [29]. However, achieving precise control over the vertically well-aligned ZnO nanorods remains a challenge. This section introduces an innovative hybrid method, utilizing sputtered AZO seed layers to grow well-aligned ZnO nanorods with the CBD technique. In order to analyze the effect of reaction times on ZnO nanorods, the structural, optical, and photocatalytic properties were investigated

## 5.2 Influence of reaction times on the properties of ZnO nanorods by CBD method

### 5.2.1 Experiment conditions

A 300 nm-thick film of Aluminum-doped Zinc Oxide (AZO) was successfully applied onto an Alkaline-free glass substrate known as Eagle XG. The deposition process employed an RF magnetron sputtering system operating at a frequency of 13.56 MHz. The sputtering utilized a 4-inch AZO target, where the composition ratio of ZnO to $Al_2O_3$ was 98:2 by weight. Prior to the sputtering process, the glass substrate was pre-heated at 150°C for a duration of 1 hour. Pure argon gas with a flow rate of 30 sccm was introduced into the chamber as the working gas. The gas flow was meticulously regulated by a mass controller to maintain consistency. Operating under controlled conditions, the pressure within the chamber was held at 1 Pa, while the temperature was consistently maintained at 150°C. Specific details of the deposition parameters can be found in Table 5.1.

Table 5.1. Deposition conditions of AZO films by RF magnetron sputtering

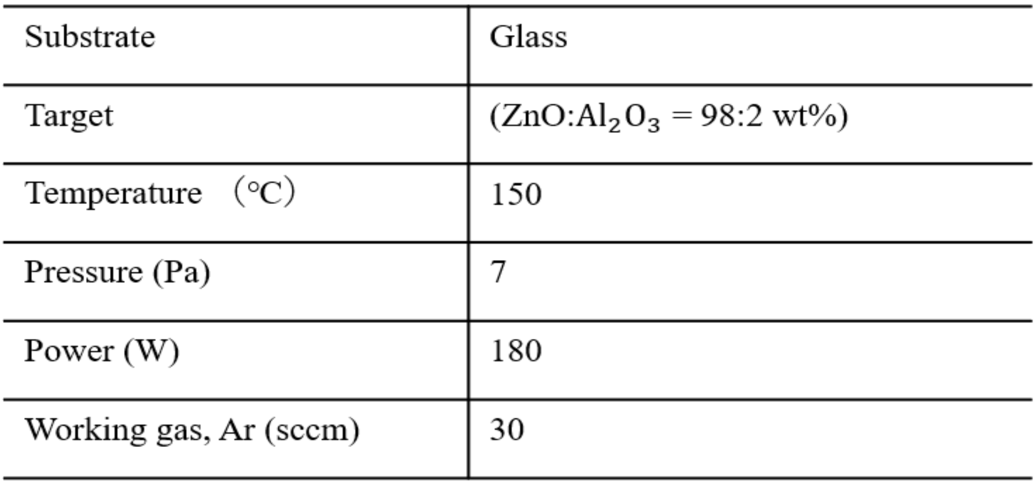

| Substrate | Glass |
|---|---|
| Target | ($ZnO:Al_2O_3$ = 98:2 wt%) |
| Temperature （°C） | 150 |
| Pressure (Pa) | 7 |
| Power (W) | 180 |
| Working gas, Ar (sccm) | 30 |

Following the sputtering procedure, the resultant AZO film, in its as-deposited state, was utilized as a substrate for cultivating ZnO nanorods using the CBD technique. A solution was prepared, combining Zn $(NO_3)_2 \cdot 6H_2O$ (0.015 mol/L) with hexamethylenetetramine (HMTA) (0.0075 mol/L). This mixed precursor solution was dissolved within 200 ml of ultrapure water, serving as the solvent. The solution was then introduced into a flask and maintained at a constant temperature of 95°C.

To examine the impact of varying growth reaction on the ZnO nanorods, the growth times were progressively altered, ranging from 1 hour to 5 hours. This controlled exploration required to clarify the relationship between reaction time and ZnO nanorod growth.

### 5.2.2. Results and Discussion

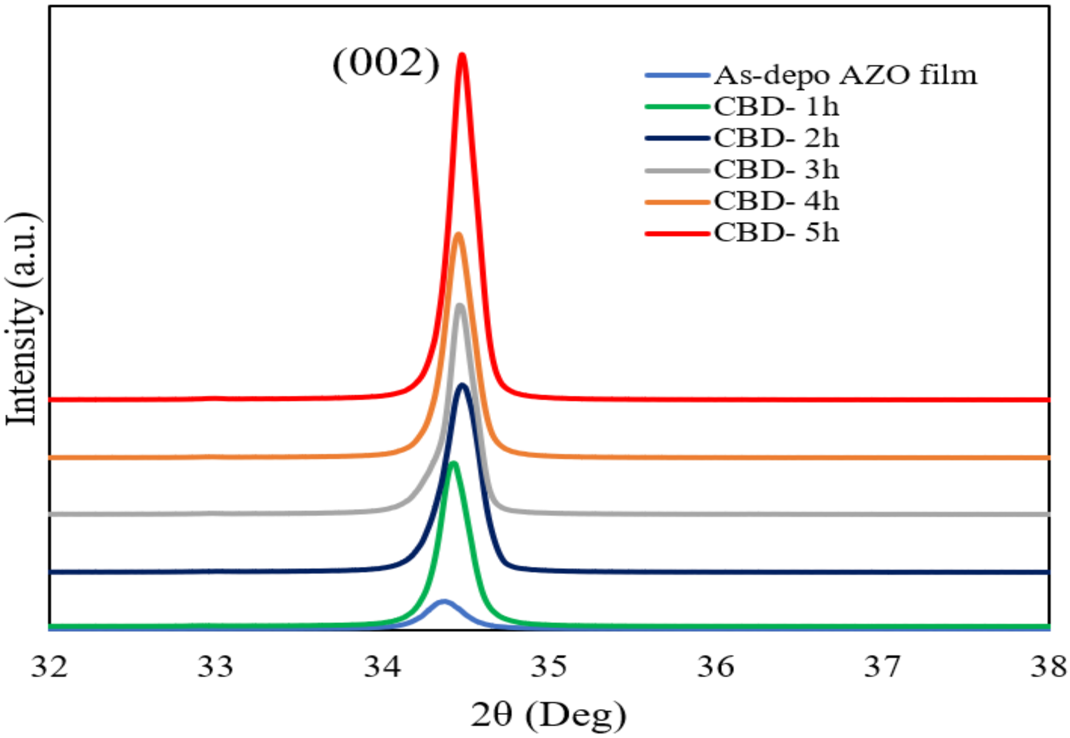

Fig 5.1 2 theta patterns of synthesized ZnO nanorods with different reaction times by CBD.

Fig. 5.1 displays the XRD patterns of both as-deposited AZO film and the synthesized ZnO nanorods, subjected to various reaction times during the CBD process. Evidently, both as-deposited AZO films and obtained ZnO nanorods showed a singular prominent diffraction peak at (002), which is preferred growth orientation along the c-axis orientation. In Table 5.2, it can be clearly observed that the intensity of the (002) peak experiences augmentation while FWHM reduces. Employing Debye-Scherrer's formula [30], while the growth reaction time was raised to 5 hours, the computed c-axis crystallite sizes of the ZnO nanorods expands to 39.47 nm. This expansion leads to the relaxed lattice constant of bulk ZnO (0.52 nm) by converging calculated lattice constant, c. The results imply an enhancement in the crystallinity of the ZnO nanorods as reaction time extends. Particularly noteworthy is the achievement of high crystallinity in ZnO nanorods grown for 5 hours.

Table 5.2. XRD analysis data of as-deposited AZO film and ZnO nanorods

| Samples | Peak position (Deg) | Intensity (cps) | FWHM (Deg) | d (nm) | C-axis crystallite size (nm) | Lattice constant, c (nm) | Compressive stress (GPa) |
|---|---|---|---|---|---|---|---|
| As-depo AZO film | 34.32 | 9821 | 0.384 | 2.6098 | 21.2 | 0.52 | -1.185 |
| CBD-1h | 34.36 | 21542 | 0.272 | 2.6085 | 30.2 | 0.52 | -0.95 |
| CBD-2h | 34.39 | 37403 | 0.258 | 2.6077 | 31.8 | 0.52 | -0.82 |
| CBD-3h | 34.41 | 40043 | 0.251 | 2.6051 | 32.7 | 0.52 | -0.37 |
| CBD-4h | 34.42 | 58367 | 0.242 | 2.6021 | 34.1 | 0.52 | 0.15 |
| CBD-5h | 34.45 | 81245 | 0.208 | 2.6003 | 39.5 | 0.52 | 0.47 |

For both the AZO film and ZnO nanorods, the compressive stress (σ) was cultivated under varying growth times, which can be mentioned by using the biaxial strain model [31] as follows:

$$\sigma = \frac{2C_{13}^2 - C_{33}(C_{11}+C_{12})}{2C_{13}} \times \frac{C_{film} - C_{bulk}}{C_{bulk}} \tag{1}$$

In this equation, Cij represents the elastic modulus of bulk ZnO films, and "c" denotes the lattice constant, with specific values of $C_{11}$ = 208.8 GPa, $C_{12}$ = 119.7 GPa, $C_{13}$ = 104.2 GPa, and $C_{33}$ = 213.8 GPa. The lattice constant "c" can also be deduced through an analysis of residual stress and XRD patterns.

The (002) peak position within the as-deposited AZO film at 34.32°, a gradual shift occurred to 34.36°, 34.39°, 34.41°, 34.42°, and eventually 34.45° for ZnO nanorods grown across distinct reaction times. Utilizing Eq. (1), the computed compressive stresses of ZnO nanorods were found to be -0.945 GPa, -0.818 GPa, -0.372 GPa, 0.151 GPa, and 0.468 GPa, respectively, with the growth time ranging from 1 hour to 5 hours. This analysis effectively revealed a relief in compressive stress within the ZnO nanorods fabricated through the CBD process. Furthermore, the lattice mismatching between the as-deposited AZO film and ZnO nanorods was reduced from 0.09% to 0.06% with an increasing of reaction time from 1 hour to 5 hours. This reduction indicated that growth direction between the as-deposited AZO film and ZnO nanorods became similar. Consequently, an enhancement in crystallinity was achieved with the increasing of reaction time. Synthesized ZnO nanorods on the AZO seed layer for a duration of 5 hours. The smallest lattice mismatch was observed from ZnO nanorods synthesized for 5 hours.

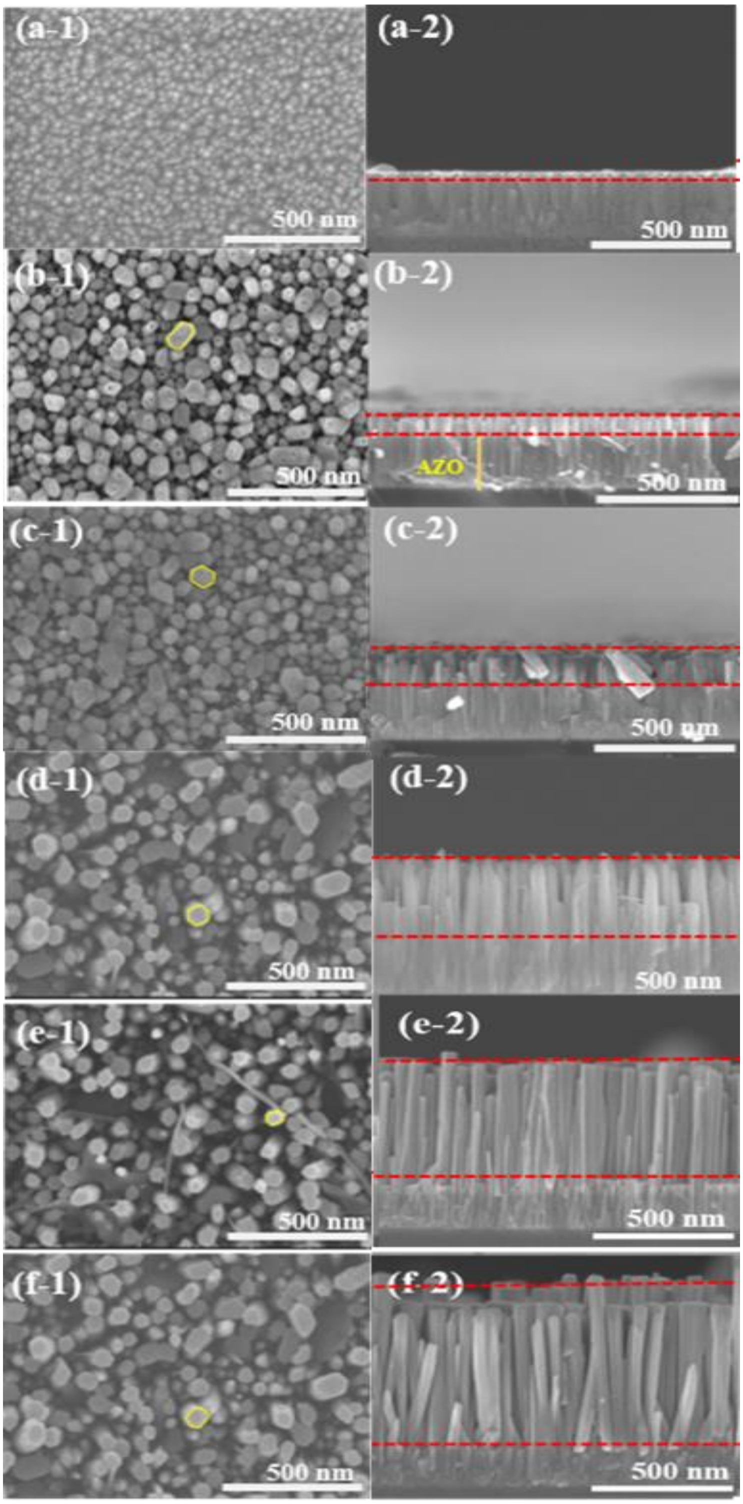

Fig. 5.2 SEM images of (a) as-deposited AZO film, and synthesized ZnO nanorods with diffraction reaction times: (b) 1 hour, (c) 2 hours, (d) 3 hours, (e) 4 hours, and (f) 5 hours; (1) top view, and (2) cross-section view.

Fig. 5.2 presents SEM images of as-deposited AZO film and ZnO nanorods synthesized on the AZO substrate through the CBD method with different reaction times. The top-view images show that the surface of the as-deposited AZO film is uniformly flat, exhibiting an average grain size of 53 nm. The resulting ZnO nanorods exhibit well-defined hexagonal facets after undergoing the CBD process, as illustrated in Fig. 5.2 (b-f). Notably, the average diameter of the ZnO nanorods was slightly increased, from 53 nm to 98 nm, when the reaction time was increased from 1 hour to 5 hours.

Conversely, the density of ZnO nanorods experiences a decrease, transitioning from 311/$\mu m^2$ to 87/$\mu m^2$ as the reaction time is extended from 1 hour to 5 hours. The average length of the ZnO nanorods displays a substantial increase, ranging from 145 nm to 1205 nm, in alignment with the increment in reaction times from 1 hour to 5 hours. The longest ZnO nanorods are observed in the AZO film grown with a 5-hour reaction time.

Under the CBD process, the growth mechanism underlying the formation of ZnO nanorods with varying reaction times can be elucidated as follows:

During the CBD process, the mixed precursor solution comprising $Zn(NO_3)_2 \cdot 6H_2O$ and HMTA is dissolved in water, thereby continually generating $Zn^{2+}$ and $OH^-$ ions, as described by the following reactions [32]:

$$Zn(NO_3)_2 \rightarrow Zn^{2+} + 2\,NO_3 \tag{2}$$

$$C_6H_{12}N_4 + H_2O \rightarrow 4\,NH_3 + 6HCHO \tag{3}$$

$$NH_3 + H_2O \leftrightarrow NH_4^+ + OH^- \tag{4}$$

$$Zn^{2+} + 2\,OH^- \rightarrow Zn(OH)_2 \tag{5}$$

$$Zn(OH)_2 \leftrightarrow ZnO + H_2O \tag{6}$$

As per the equations mentioned from (2) to (6), the $Zn^{2+}$ ions, arising from the dissolution of $Zn(NO_3)_2 \cdot 6H_2O$, undergo ionization and engage in a reaction with the $OH^-$ ions. These $OH^-$ ions are generated through the hydrolysis of HMTA, eventually leading to the formation of $Zn(OH)_2$. The obtained $Zn(OH)_2$ species undergoes dehydration, and transforming into ZnO. With the increasing of the reaction time, more ZnO was likely to be generated and subsequently stacked atop one another. This accumulation of ZnO contributes to the elongation of ZnO nanorods, thus leading to an increase in their overall length.

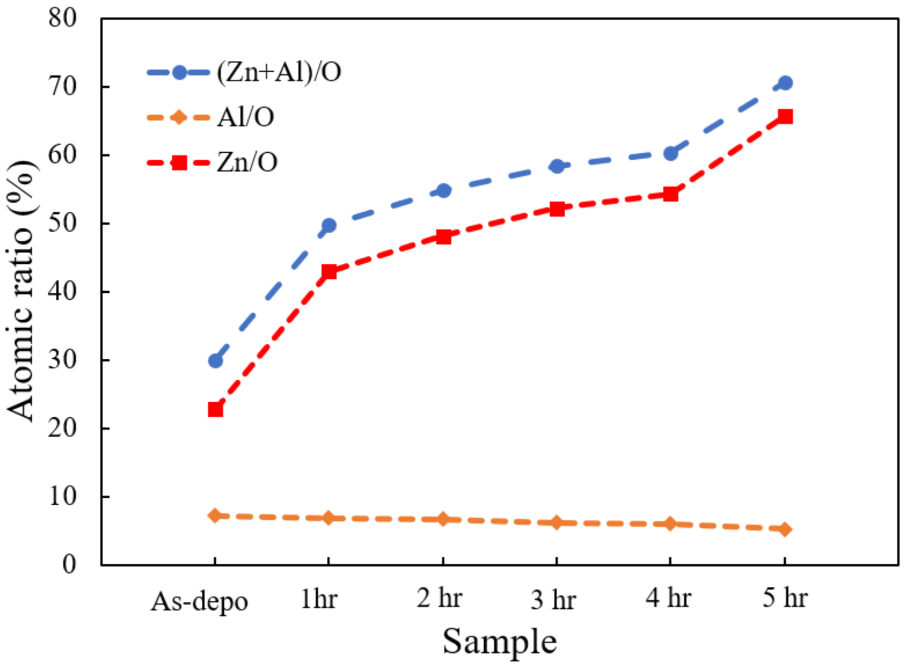

Fig. 5.3 Atomic ratios variations of Zn, Al, and O calculated from EDX analysis of as-deposited AZO film, and synthesized ZnO nanorods with different reaction times by CBD.

The elemental composition of the as-deposited AZO film and synthesized ZnO nanorods was carried out through EDX measurements. The plot depicting the variations in atomic ratios of Zn, Al, and O is displayed in Fig. 5.3. Notably, the atomic ratio of (Zn+Al)/O was significant increased with the increasing of reaction times from 1 hour to 5 hours. This result suggests a more significant number of Zn ions were incorporated into the formation of ZnO nanorods. Furthermore, the atomic ratios of Zn/O also exhibited a substantial increasing with the increasing of reaction times. However, the atomic ratio of Al/O remained relatively constant as the reaction time was increased, suggesting that the influence of aluminum on the ZnO nanorods was negligible.

Conversely, the atomic ratios of Zn/O exceeded those of Al/O with the increase in reaction time from 1 hour to 5 hours. This observation implies that a significantly more significant number of Zn ions were generated and subsequently transformed into ZnO, leading to their growth along the c-axis direction. The ZnO nanorods synthesized for 5hours showed the highest atomic ratio of Zn/O, which directly attributed to the increasing in the length of ZnO during the CBD process.

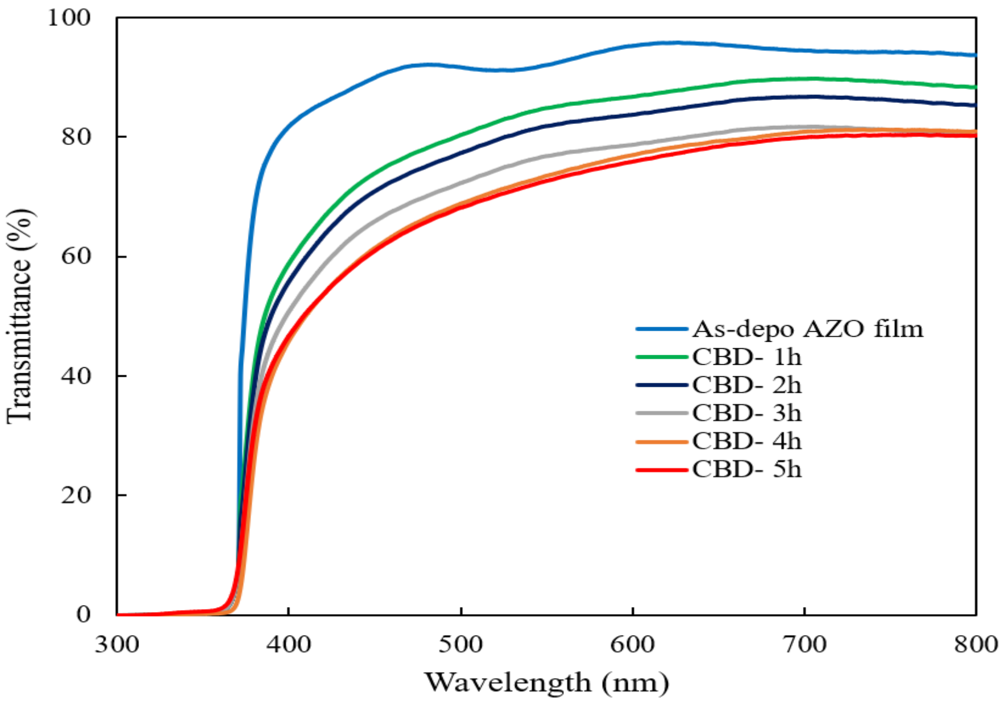

Fig. 5.4 Transmission spectra of synthesized ZnO nanorods with different reaction times by CBD.

Fig. 5.4 illustrates the optical transmittance spectra of the as-deposited AZO film and the ZnO nanorods with varying reaction times. Notably, the as-deposited AZO film displayed a high transmittance level of approximately 90%, and a comparable high transmittance of around 70% was observed for all ZnO nanorods in the visible region. It can be confirmed that changes in the reaction times during the CBD process had minimal impact on transmittance. This phenomenon may be attributed to the well-aligned vertical orientation of all ZnO nanorods on the as-deposited AZO film, further contributing to their high transmittance characteristics.

When the reaction time was increased from 1 hour to 5 hours, the calculated bandgap energy values of the synthesized ZnO nanorods exhibited a decrement from 3.32 eV to 3.22 eV, based on the Tauc’s plot equation. This alteration signifies that electrons originating from the valence band can now more readily undergo transitions to the conduction band within ZnO nanorods grown from 1 hour to 5 hours.

This high electron transition leads to an augmentation in the generation rate of active radicals during the degradation process [33]. As the bandgap energy narrows, a larger portion of the incident light spectrum becomes effective in generating charge carriers, facilitating a more efficient photodegradation mechanism. Therefore, the progressive decrease in bandgap energy of the ZnO nanorods, corresponding to the elongation of growth reaction time, bolsters the efficiency of photodegradation due to the increased availability of active charge carriers.

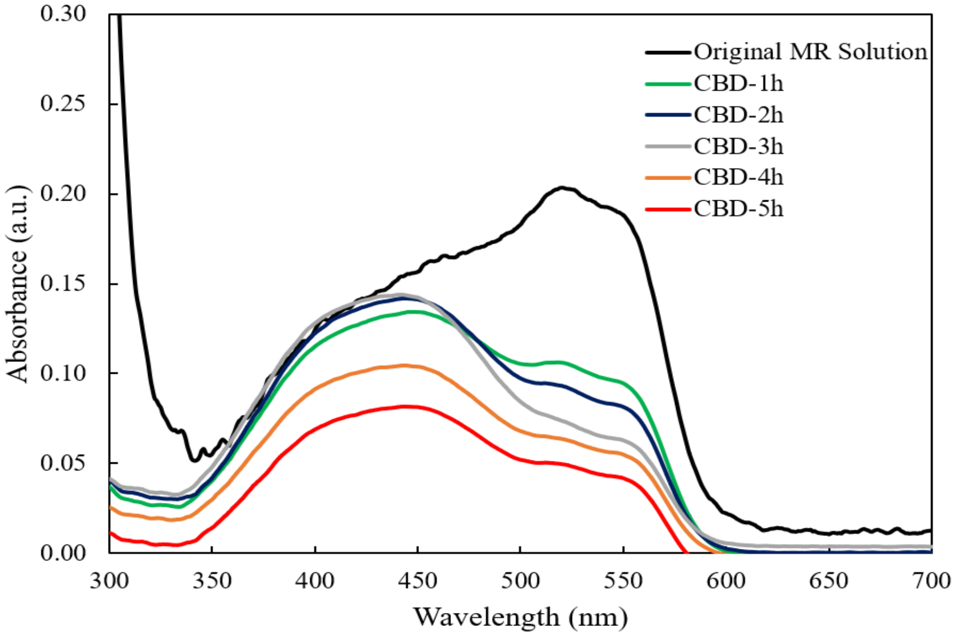

Fig. 5.5 The absorption spectra of MR solution for synthesized ZnO nanorods with different reaction times by CBD.

Fig. 5.5 presents the absorbance of the MR solution for ZnO nanorods grown using varied growth times by CBD method. It was found that when the reaction time was increased from 1 hour to 5 hours, the absorption intensities of ZnO nanorods were slightly decreased, in comparison with original MR solution. It can be confirmed that the photodegradation efficiency exhibited by all ZnO nanorods, with the ZnO nanorods grown over 5 hours achieving the lowest absorption intensity.

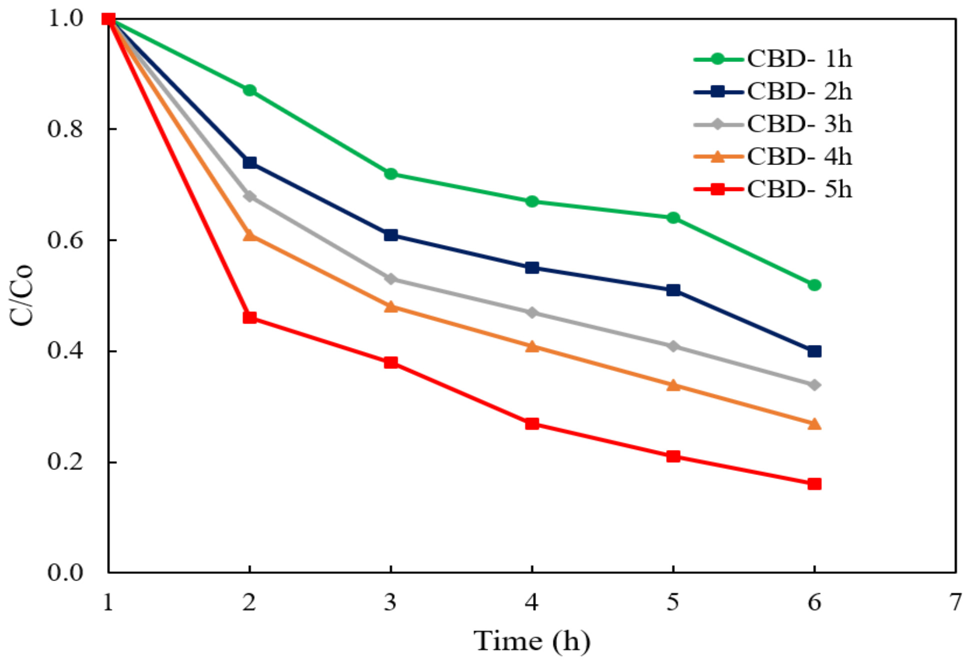

Fig. 5.6 Plot of C/Co with the irradiation times for synthesized ZnO nanorods with different reaction times by CBD.

Analyzing the absorption spectra of ZnO nanorods (Fig. 5.5), it becomes apparent that all absorption spectra fall within the wavelength range of 300 nm to 700 nm. The result suggests that photodegradation efficiency was exhibited for all synthesized ZnO nanorods under UV irradiation.

In order to understand the growth of ZnO nanorods during the CBD process, the mechanism was revealed. The concentration of Zn $(NO_3)_2{\cdot}6H_2O$ exceeded that of HMTA by two times, indicating a significantly higher incorporation of generated $Zn^{2+}$ ions relative to OH- ions. Consequently, the increased $Zn^{2+}$ ions may introduce zinc interstitial ($Zn_i$) defects into the ZnO nanorods during CBD growth. The $Zn_i$ defect could act as an intermediate energy level, facilitating electron excitation with less energy. This phenomenon enhances the photocatalytic efficiency of ZnO nanorods within the visible range.

Based on L-H model, the calculated rate constant (k) values for ZnO nanorods, was increased from 0.00214 $min^{-1}$ to 0.00572 $min^{-1}$ with an increase in CBD reaction time from 1 hour to 5 hours. The highest reaction rate is achieved with ZnO nanorods grown for 5 hours.

To further study the photocatalytic process of ZnO nanorods, the photodegradation mechanism is illustrated in Fig. 5.6. Under UV irradiation on ZnO nanorods, the generated electrons ($e^-$) from the valence band excited to the conduction band, thus forming holes ($h^+$) in the valence band. The photodegradation reaction of ZnO can be mentioned as follows:

$$e^- + O_2 \rightarrow .O_2^- \tag{7}$$

$$h^+ + H_2O \rightarrow OH^- + H^+ \tag{8}$$

$$.O_2^- + OH^- \rightarrow {}^{\circ}HO_2 \tag{9}$$

$${}^{\circ}HO_2 + H^+ \rightarrow H_2O_2 \tag{10}$$

$$H_2O_2 + e^- \rightarrow {}^{\circ}OH + OH^- \tag{11}$$

In Fig. 5.7 (a), the excited electrons ($e^-$) can be easily traverse surface of ZnO, subsequently oxidizing with atmospheric $O_2$ to generate superoxide radicals ($.O_2^-$). Concurrently, holes ($h^+$) interact with water molecules ($H_2O$) to yield $OH^-$ ions. The generated superoxide radicals ($.O_2^-$) continue to react with decomposed hydrogen ions originating from water molecules, ultimately resulting in the formation of $H_2O_2$. This sequence of reactions culminates in the creation of hydroxyl radicals (°OH), as governed by Eq. (7-11).

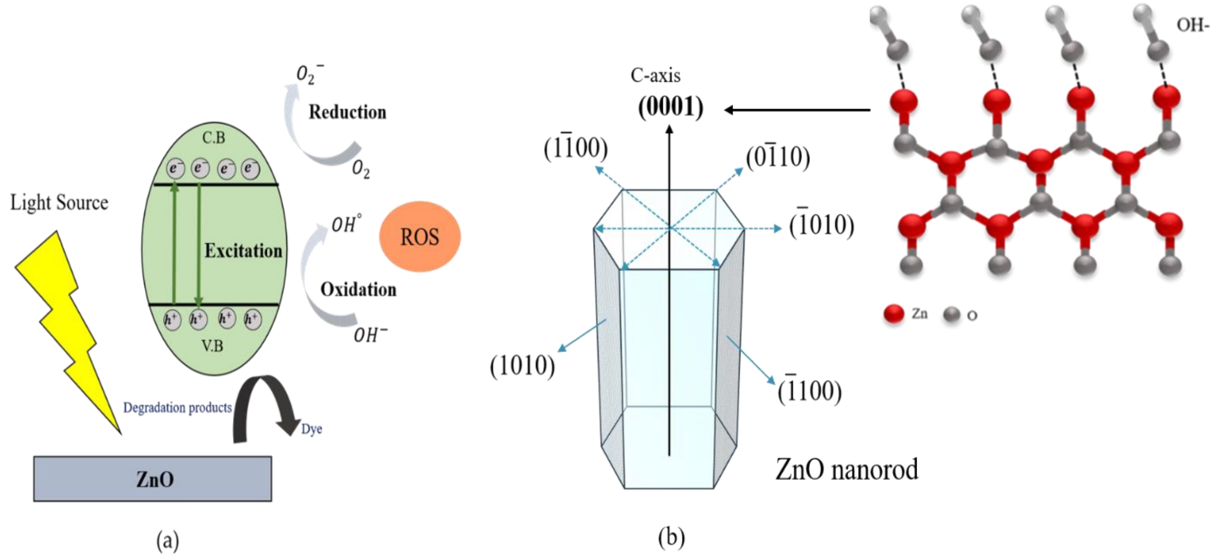

Fig. 5.7 (a)Schematic diagram of photocatalytic mechanism occurring in ZnO, and (b) (0001) plane of ZnO nanorod responsible for its improved photocatalytic efficiency.

To further enhance the photodegradation efficiency of ZnO, the active sites on the surface of ZnO nanorods could be supported the formation rate of ROS radicals. The (0001) facets possess large surface energy, giving rise to abundant reaction sites within the wurtzite structure of ZnO, as illustrated in Fig. 5.7 (b). The $OH^-$ ions can be attracted on (0001) surface of ZnO because of their inherent positive charge, leading to interactions with photogenerated holes ($h^+$) and giving rise to ROS species [34]. This mechanism reveals the photocatalytic efficiency. Most notably, the strong crystal facets in (0001) crystal plane were discovered in ZnO nanorods fabricated for 5 hours.

Moreover, ZnO nanorods with high crystallinity along the (0001) crystal plane could be significantly exhibited the direct band transitions within the ZnO nanorods. This high efficiency fosters the accelerated generation of electron and hole pairs, thus enhancing the formation of $.O_2^-$ and °OH radicals. Particularly, this study revealed an enhancement in ZnO nanorod crystallinity over the growth reaction ranging from 1 hour to 5 hours. The ZnO nanorods exhibited well alignment and having undergone 5 hours of growth, the highest crystallinity, predominantly along the (0001) growth direction. This enhanced crystallinity enabled the absorption of more significant OH- ions, thereby generating an increased quantity of hydroxyl radicals for MR solution degradation.

Furthermore, when growth reaction time increased to 5 hours, there was a significant increase in the volume of the resultant ZnO nanorods, involving both length and diameter. This growth implied the creation of more surface-active sites and increased the absorption capacity of the MR solution. It can be improved the absorption of a more significant number of incident photons and consequently generating more photogenerated charge carriers. Consequently, the degradation reaction rate improved, culminating in notable photocatalytic efficiency. Remarkably, the well-aligned ZnO nanorods fabricated for 5 hours achieved a high photodegradation efficiency with high degradation rate..

### 5.2.3 Conclusions

During the CBD process, the duration of the growth reaction played a pivotal role in shaping the morphology and crystallinity of synthesized well-arranged ZnO nanorods. Notably, the growth direction of the ZnO nanorods was significantly influenced on the growth direction of the underneath AZO seed layer. An obvious enhancement in the crystallinity of ZnO nanorods along the (0001) growth orientation were observed with the increasing of reaction times. The most impressive crystallinity was achieved in ZnO nanorods grown for 5 hours. This improved crystallinity was attributed to the increased generation and bonding of $Zn^{2+}$ ions with oxygen. Consequently, these resultant ZnO crystallites demonstrated a propensity to align along the c-axis (0001) growth direction, leading to an elongation in their length. It is worth highlighting that all the fabricated ZnO nanorods exhibited a notable light transmittance exceeding 70% within the visible spectrum. Notably, ZnO nanorods grown for 5 hours exhibited the most remarkable photodegradation efficiency, coupled with the high degradation reaction rate of 0.00572 $min^{-1}$.

## 5.3 Influence of AZO coating times on the properties of AZO/ZnO core-shells nanorods by mist CVD method

In upper section, we have succeeded in obtaining the well-aligned ZnO nanostructures on AZO substrate using CBD method. However, ZnO has a strong affinity for dye molecules and a high efficiency of electron injection, which leads to an increased recombination rate of electron-hole pairs. In order to overcome this issue, ZnO nanorods were coated with AZO to form AZO/ZnO core-shell nanostructures, which might be reduced the direct interaction between dye molecules and ZnO, and decreased the electron-hole recombination rate. However, the morphology of ZnO nanostructures still needed to be enlarged for the photocatalytic application. In this section, a novel mist CVD technique was firstly introduced to treat obtained ZnO nanostructures from CBD method. The effects of AZO coating times on the properties of obtained ZnO nanostructures were investigated.

### 5.3.1 Experiment conditions

AZO thin film, with a thickness of 300nm, was successfully deposited onto alkali-free glass sheets using an RF magnetron sputtering system. The deposition conditions for the AZO film were consistent with those outlined in Table 5.1, as detailed in section 5.2.1.

Following the sputtering process, well-aligned of ZnO nanorods were vertically grown on the AZO film utilizing the CBD method. Throughout the CBD process, a prepared mixed precursor solution was employed. This solution consisted of Zn $(NO_3)_2 \cdot 6H_2O$ with a concentration of 0.015 mol/L, along with HMTA at a concentration of 0.0075 mol/L, both of which were dissolved in 200 ml of ultrapure water acting as a solvent. The substrate samples were then immersed within this mixed precursor solution and held at a temperature of 95°C for a duration of 5 hours.

Following the successful fabrication of the ZnO nanorods, a subsequent coating of AZO was expertly applied through the mist CVD method. In order to examine the effects of AZO coating on the ZnO nanorods, the coating times were set at 5, 10, 15, 20 minutes, respectively. Deposition conditions for AZO coating process are given in Table 5.2.

Table 5.2. Deposition conditions of AZO/ZnO core-shells by mist CVD

| Solute | Zinc acetate, Aluminum acetylacetonate |
|---|---|
| Solvent | Methanol, $H_2O$ |
| Concentration (mol/L) | 0.04 |
| Al doping ratio (wt%) | 2 |
| Deposition temperature (°C) | 400 |
| Carrier gas, Flow rate (L/min) | Nitrogen , 2.5 |
| Dilution gas, Flow rate (L/min) | Nitrogen , 4.5 |
| AZO coating time (minutes) | 5, 10, 15, 20 |
| Substrate | ZnO nanorod |

## 5.3.2 Results and Discussion

Fig. 5.8 presents SEM images of both the as-deposited ZnO nanorods and AZO/ZnO core-shells nanorods by the mist CVD process. In the top-view, the as-deposited ZnO nanorods exhibited a hexagonal wurtzite structure prior to the AZO coating. Following a 5 minutes coating process, the hexagonal structure transformed into a circular shape. After 20 minutes of coating, it was observed that the AZO had completely covered the surface of the as-deposited ZnO nanorods. In a cross-sectional view, it was observed that the as-deposited ZnO nanorods exhibited a vertical growth orientation on the AZO substrates, with an average length of approximately 1206 nm. It was clearly evident that small AZO nanoparticles attached to the as-deposited ZnO nanorods after 5 minutes of coating, indicating that the coating process was gradually building up on the as-deposited ZnO nanorods. When the coating time reached 20 minutes, the entire ZnO nanorods were successfully coated with AZO, while the length of the ZnO nanorods remained unchanged after coating.

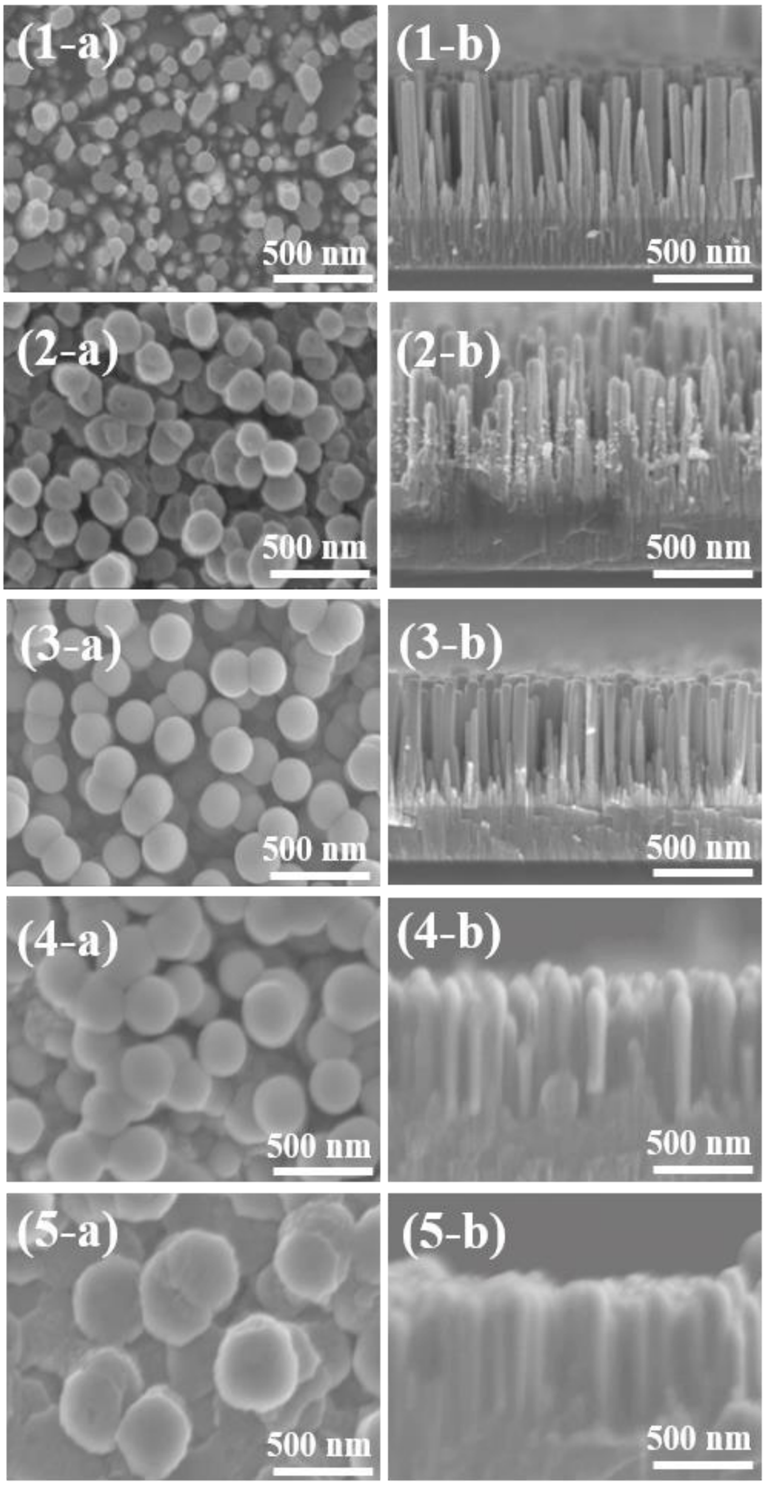

Fig. 5.8 SEM images of (1) as-deposited ZnO nanorods and AZO/ZnO core-shells with different coating times by mist CVD ((2) 5 min; (3) 10 min; (4) 15 min; (5) 20 min; (a) top view; (b) cross-section view).

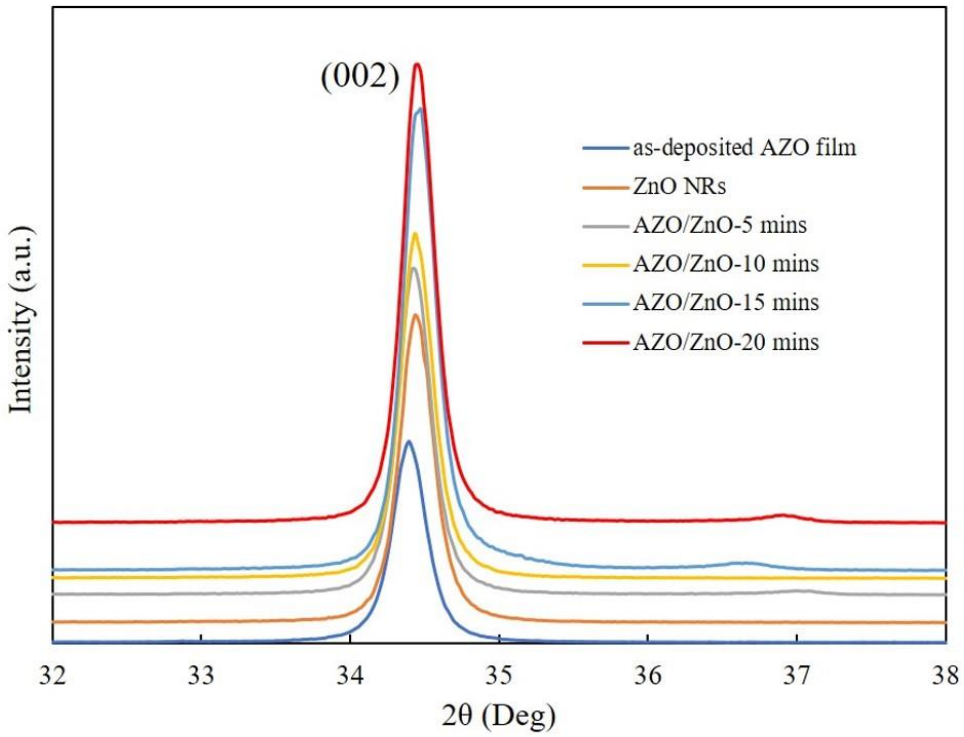

Fig. 5.9 2 theta pattern of as-deposited AZO film, as-deposited ZnO nanorods and AZO/ZnO core-shells with different coating times by mist CVD.

Fig. 5.9 shows the XRD pattern of as-deposited AZO film, as-deposited ZnO nanorods and ZnO nanorods coated with AZO by mist CVD method. It was found that there was a dominant (002) peak for as-deposited AZO film and as-deposited ZnO nanorods after CBD process, which meant that the obtained as-deposited AZO film and the fabricated ZnO nanorods were oriented along the c-axis orientation growth. After coating with AZO, the AZO/ZnO core-shell nanorods could be kept the same growth orientation along the (002) crystal plane. When the coating time increased from 5 minutes to 20 minutes, the intensity of (002) diffraction peak showed a trend of increased, which can be contributed to the annealing effect due to the coating temperature at 400°C during mist CVD process. The average crystallite size was enlarged from 41.2 nm to 78.6 nm when the coating time is increased from 5 minutes to 20 minutes after the mist CVD process. AZO/ZnO core-shell nanorods coated with AZO for 20 minutes achieved the highest crystallinity.

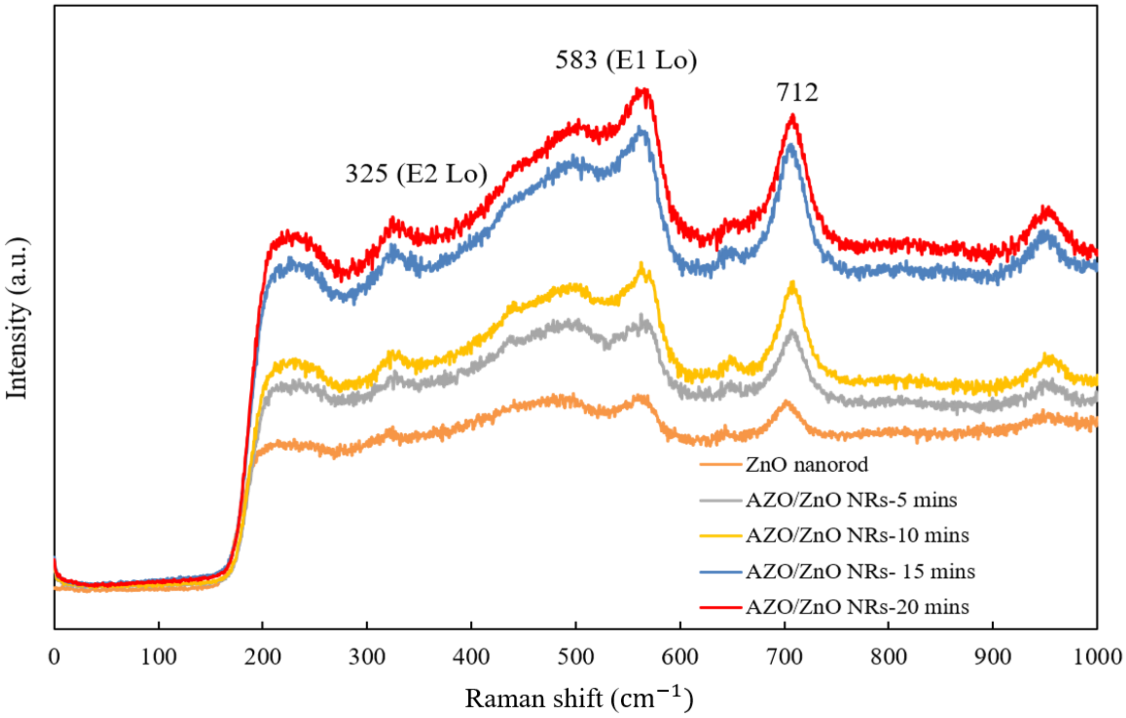

Fig. 5.10 Raman spectra of as-deposited ZnO nanorods and AZO/ZnO core-shells with different coating times by mist CVD.

Fig. 5.10 depicts the Raman spectra of both the as-deposited ZnO nanorods and the AZO/ZnO core-shells nanorods with different coating times. Three distinctive Raman peaks were prominently observed at 325 cm$^{-1}$, 583 cm$^{-1}$, and 715 cm$^{-1}$. These peaks could be corresponded to the E2 (LO) mode, E1 (LO) mode, and secondary Raman peak characteristic of standard ZnO [35], respectively. This observation strongly indicates the successful coating of AZO onto the ZnO nanorods. Notably, the intensities of Raman peaks were enhanced when the coating time was increased to 20 minutes. This enhancement in Raman peak intensities signifies an improvement in crystallinity with the prolongation of coating time. These findings are in alignment with the results obtained from EDS and GIXRD measurements.

Fig. 5.11 presents the transmission spectra of both the as-deposited ZnO nanorods and AZO/ZnO core-shells nanorods with different AZO coating times. The initial transmittance of the as-deposited ZnO nanorods stood at approximately 70% within the visible region. However, as the AZO coating time was extended from 5 minutes to 20 minutes, the transmittance gradually declined to approximately 55%. This reduction in transmittance can be attributed to the introduction of more defects into the AZO/ZnO core-shell nanorods during the mist CVD process. The optical bandgaps were enlarged from 3.52 eV to 3.65 eV when the coating time was increased to 20 minutes.

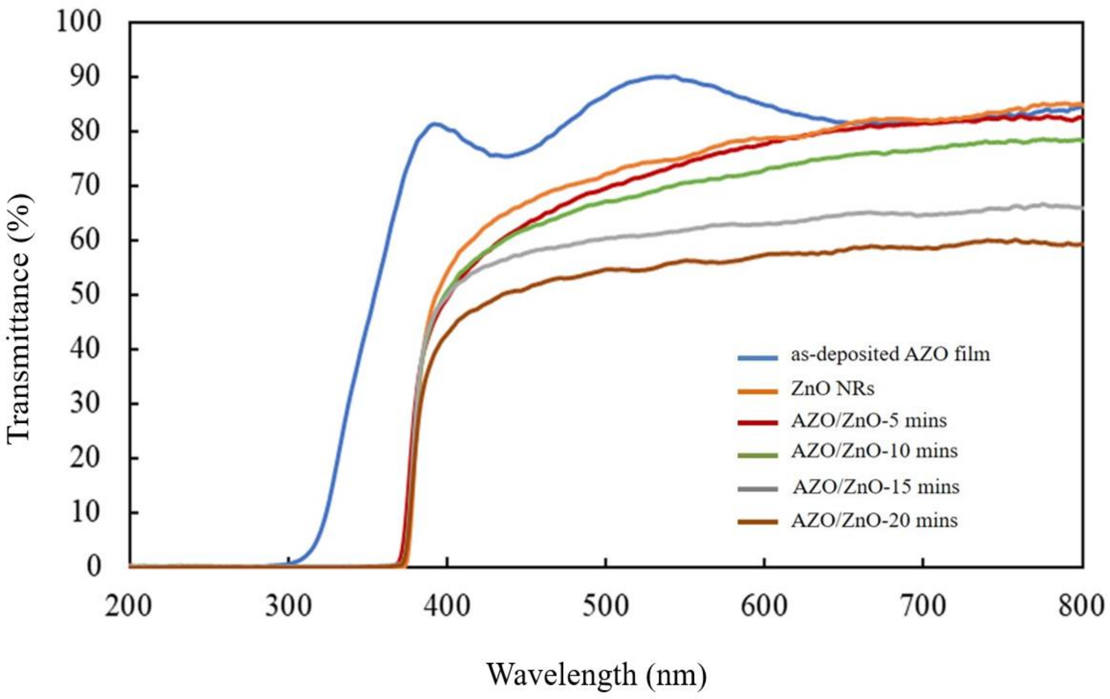

Fig. 5.11 Transmission spectra of as-deposited ZnO nanorods and AZO/ZnO core-shells with different coating times by mist CVD

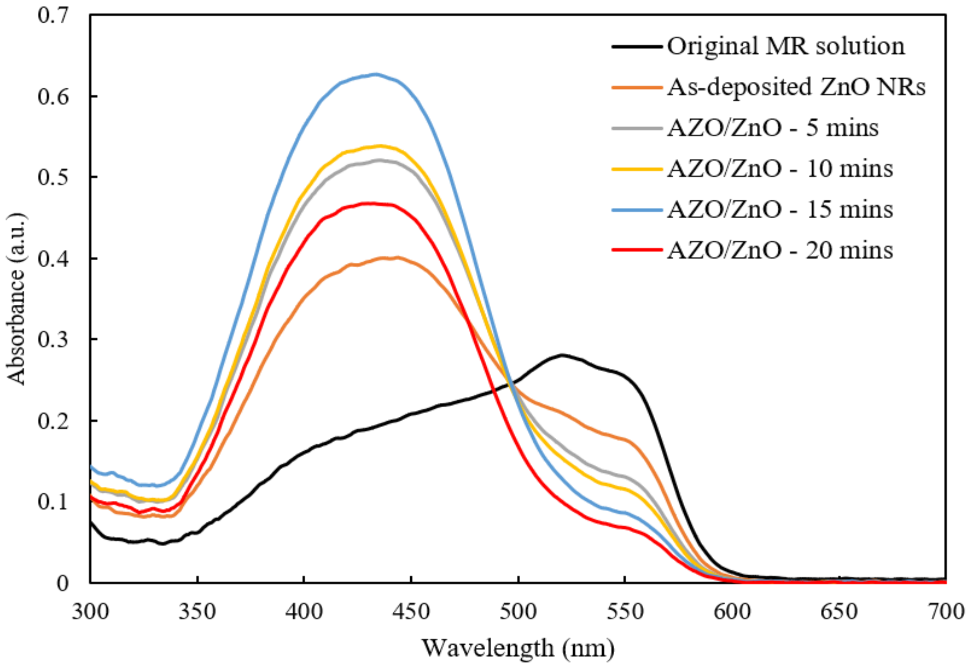

Fig. 5.12 Absorption spectra of MR solution of the as-deposited ZnO nanorods and AZO/ZnO core-shells with different coating times by mist CVD.

Fig. 5.12 illustrates the absorption spectra of the MR solution for both the as-deposited ZnO nanorods and AZO/ZnO core-shell nanorods with different AZO coating times by the mist CVD method. Evidently, for all AZO/ZnO core-shell nanorods with different AZO coating times, the absorption intensities of the MR solution exhibit a gradual reduction as the coating times increase from 5 minutes to 20 minutes, in comparison to the absorbance of the original MR solution. It can be indicated the achievement of photodegradation efficiency for all AZO/ZnO core-shell nanorods. Notably, the AZO/ZnO core-shell nanorods with a 20-minute coating time exhibit the lowest absorption intensity, signifying enhanced photodegradation efficiency.

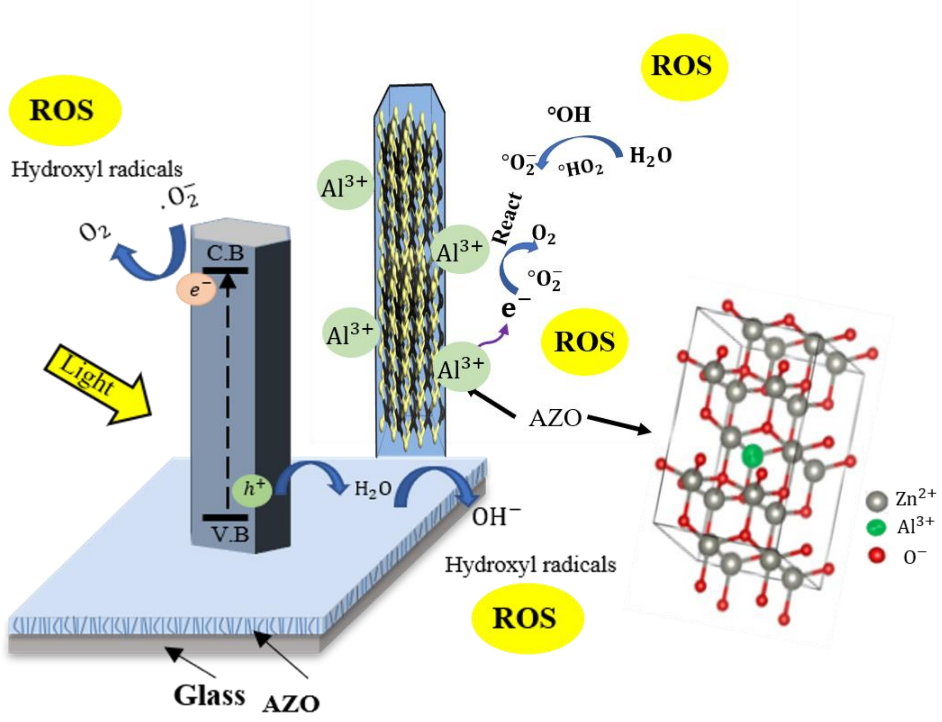

Fig. 5.13 Schematic diagram of photocatalytic mechanism of AZO/ZnO core-shells under UV irradiation.

In order to understand the photocatalytic mechanism of AZO/ZnO core-shell nanorods under UV light irradiation, the photocatalytic mechanism occurring in the AZO/ZnO core-shell nanorods is depicted in the schematic diagram shown in Fig. 5.13. The photocatalytic mechanism of ZnO nanostructures under UV light irradiation has been described extensively in the previous section. In our experiment, AZO was coated as a barrier to reduce the recombination rate of electron-hole pairs and prevent direct contact of ZnO with dye molecules. During the coating process, $Al^{3+}$ replaced $Zn^{2+}$ in its sites, the extra electron of Al migrated to the surface of AZO/ZnO core-shell and self-excitation process of the electron could occur during the degradation process. When the coating time increased, the high concentration of Al was entered to the ZnO and increased the amount of extra electron of Al, which might be contributed to improve the degradation efficiency. Moreover, the several defects could be introduced to AZO/ZnO core-shell, which act as electron traps and inhibit electron recombination, ultimately enhancing carrier separation and photodegradation efficiency of AZO/ZnO core-shell nanostructures.

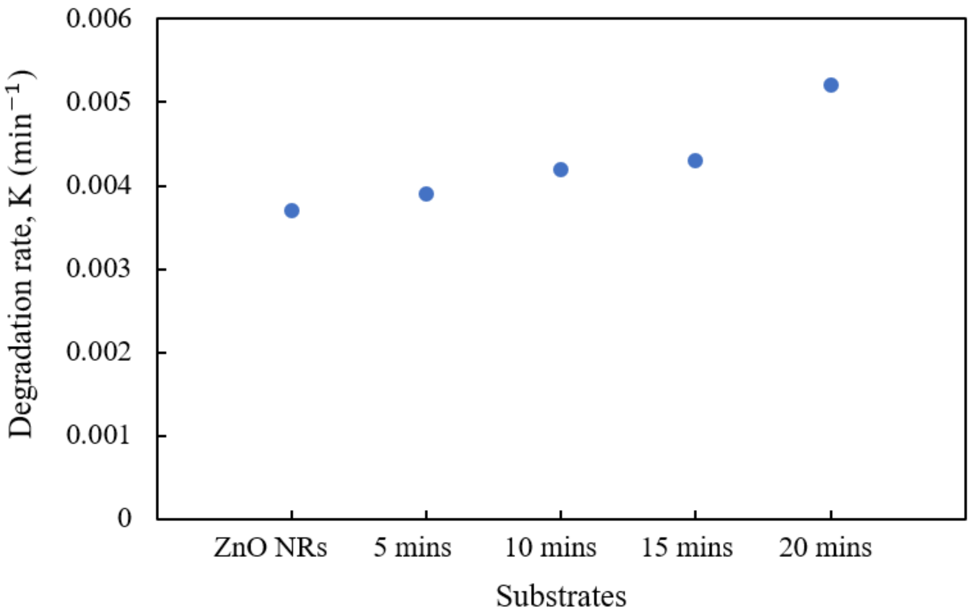

Fig. 5.14 Degradation rate of irradiated MR solution of the as-deposited ZnO nanorods and AZO/ZnO core-shells with different coating times by mist CVD.

The changes in the absorption spectra of MR solution provide understanding into the rates of photocatalytic degradation, as illustrated in Fig. 5.14. Based on L-H model [36], the rate of adsorption can be expressed through the coverage ratio of reactants adsorbed onto the surface of the photocatalyst. The kinetic rate of the degradation reaction, denoted as K, can be mathematically represented by the following equation:

$$k = \ln (C_t/C_o)/t \tag{1}$$

The observed first-order degradation reaction rate (k) is governed by the initial dye concentration (Co) and the dye concentration at a specific time (Ct). In accordance with the L-

H model, a higher first-order degradation reaction rate signifies an high photocatalytic efficiency. Upon subjecting the obtained samples to UV light during the photodegradation process, the calculated first-order degradation reaction rates for AZO/ZnO core-shell nanorods with a 5-minute AZO coating were 0.0039 min$^{-1}$. This rate progressively increased to 0.0042 min$^{-1}$, 0.0043 min$^{-1}$, and 0.0053 min$^{-1}$, respectively. Notably, the most pronounced enhancement in degradation rate was observed in AZO/ZnO core-shell nanorods with a 20-minute AZO coating time when exposed to UV light.

### 5.3.3 Conclusions

During the mist CVD process, the duration of the coating had a significant influence on the growth and crystalline quality of AZO/ZnO core-shell nanorods synthesized on the initially deposited AZO seed layer. These core-shell nanorods exhibited a vertical alignment that relatively followed the growth orientation of the underneath AZO seed layer. The crystallinity of AZO/ZnO core-shell nanorods along the (0001) crystal plane was improved as the coating time was extended from 5 minutes to 20 minutes. The high crystallinity was achieved in AZO/ZnO core-shell nanorods coated for 20 minutes. All the synthesized AZO/ZnO core-shell nanorods confirmed the optical transmittance of approximately 60% within the visible region. The AZO/ZnO core-shell nanorods coated for 20 minutes exhibited the highest photodegradation efficiency, with a corresponding degradation reaction rate of 0.0053 min$^{-1}$. The results could be suggested the efficient degradation capabilities of the ZnO nanorods towards MR dye solutions, highlighting their strong potential for application in effective photocatalysis.

## 5.4 References

[1] C. Minero, E. Pelizzatti, M. Sega, S.E. Friberg, J. Sjoblom. J. Dispersion. Sci.Technol. 1999, 20, 643–661.

[2] K. Pirkanniemi, M. Sillanpa. Chemosphere. 48 (2002) 1047–1060.

[3] K. Maeda, K. Domen. J. Phys. Chem. Lett. 1 (2010) 2655–2661.

[4] D. Chen, A.K. Ray. Chem. Eng. Sci. 56 (2001) 1561–1570.

[5] A. Mills, S. Lehunte. Chem. Soc. Rev. 22 (1997) 417–425.

[6] H. Gerischer. J. Electrochem. Soc. 113 (1966) 1174–1182.

[7] A. Mills, C. O'Rourke, K. Moore. J. Photochem. Photobiol. 310 (2015) 66–105.

[8] M. Kanemoto, T, Shiragami, C. Pac, S. Yanagida, M. Kanemoto, T. Shiragami, C. Pac. J. Phys. Chem. 96 (1992) 3521–3526.

[9] K. Hashimoto, H. Irie, A. Fujishima. J. Appl. Phys. 44 (2005) 8269-8285.

[10] A.O. Ibhadon, P. Fitzpatrick. Catal. 3 (2013) 189-218.

[11] W.Y. Teoh, R. Amal, J. Scott. J. Phys. Chem. Lett. 3 (2012) 629–639.

[12] D.S. Bhatkhande, V.G. Pangarkar, A.A.C.M. Beenackers. J. Chem. Technol. Biotechnol. 77 (2001) 102–116.

[13] X. Li, J. Wen, J. Low, Y. Fang, J. Yu. Sci. China Mater. 57 (2014) 70–100.

[14] P. Franco, O. Sacco, I. De Marco, V. Vaiano. Catal. 9 (2019) 355-387.

[15] K. Vanheusden, W.L. Warren, C.H. Seager, D.R. Tallant, J.A. Voigt, B.E. Gnade. J. Appl. Phys. 79 (1996) 7983–7990.

[16] C. Baratto, E. Comini, M. Ferroni, G. Faglia, G. Sberveglieri. Crystengcomm. 15 (2013) 7981–7986.

[17] Y.S. Seo, S.G. Oh. Korean J. Chem. Eng. 36 (2019) 2118 – 2124.

[18] D. Gaspar, L. Pereira, K. Gehrke, B. Galler, E. Fortunato, R. Martins. Sol. Energy Mat. Sol. C. 163 (2017) 255–262.

[19] B.K. Meyer, H. Alves, D.M. Hofmann, W. Kriegseis, D. Forster, F. Bertram, J. Christen, A. Hoffmann, M. Strassburg, M. Dworzak. Phys. Status Solidi. B. 241 (2004) 231–260.

[20] S. Mukhopadhyay, P.P. Das, S. Maity, P. Ghosh, P.S. Devi. Appl. Catal. B-Environ. 165 (2015) 128–138.

[21] E. Luevano-Hipolito, A. Martinez-de la Cruz, E.L. Cuellar. Sci. Pollut. Res. 24 (2016) 6361–6371.

[22] C.B. Ong, L.Y. Ng, A.W. Mohammad. Energ. Rev. 81 (2018) 536–551.

[23] E. Luevano-Hipolito, A. Martinez-de la Cruz, E.L. Cuellar. Sci. Pollut. Res. 24 (2016) 6361–6371.

[24] R. Ebrahimi, K. Hossienzadeh, A. Maleki, R. Ghanbari, R. Rezaee, M. Safari, B. Shahmoradi, H. Daraei, A. Jafari, K. Yetilmezsoy. J. Environ. Health Sci. Eng. 17 (2019) 479–492.

[25] F. Yu, B. Wang, H. Hu, H. Li, T. Song, B. Xu, L. He, H. Duan, S. Wang. Phys. Status Solidi. 216 (2019) 1900386-1900395.

[26] N. Ahammed, M.S. Hassan, M. Hassan. Mater. Sci.-Poland. 36 (2018) 419–426.

[27] R. Mahdavi, S.S.A. Talesh. Adv. Powder. Technol. 28 (2017) 1418–1425.

[28] F.I. Lai, J.F. Yang, Y.C. Hsu, S.Y. Kuo. Mater. 14 (2021) 6313-6323.

[29] P. Tang, B. Li, L. Feng. Ceram. Int. 44 (2018) 4154–4157.

[30] J.-K. Jeong, H.-J. Yun, S.-D. Yang, K.-Y. Eom, S.-W. Chea, J.-H. Park, H.-D. Lee, G.-W. Lee. Thin. Solid. Films. 638 (2017) 89–95.

[31] N. Kaneva, I. Stambolova, V. Blaskov, Y. Dimitriev, A. Bojinova, C. Dushkin. Surf. Coat. Technol. 207 (2011) 5–10.

[32] Y. Wang, X. Zhang, L. Bai, Q. Huang, C. Wei, Y. Zhao. Appl. Phys. Lett. 100 (2012) 263508-263622.

[33] S.H. Jeong, G.C. Park, J.H. Choi, C.M. Lee, S.M. Lee, T.Y. Seo, D.H. Choi, S.B. Jung, J.H. Lim, J. Joo. J. Nanosci. Nanotechnol. 16 (2016) 11272–11276.

[34] P. Rutthongjan, Liu, M. Nishi, M. Sakamoto, S. Sato, E.K.C. Pradeep, G.T. Dang, T. Kawaharamura. J. Appl. Phys. 58 (2019) 035503-035512.

[35] L. Liu, Y. Suwa, S. Sato, Y. Nakasone, M. Nishi, G.T. Dang, E.K.C. Pradeep, T. Kawaharamura. Jpn. J. Appl. Phys. 58 (2019) 025502-025509.

[36] M. Golshan, M. Zare, G. Goudarzi, M. Abtahi, A.A. Babaei. Mater. Res. Bull. 91 (2017) 59–67.

# Chapter 6

## Summary

In this thesis, fabrication of ZnO-related thin films and nanostructures in application of photocatalytic was investigated.

Pure ZnO thin films with different thicknesses were fabricated using mist CVD method. The structural, and optical properties were evaluated. In order to reduce the recombination rate of electron and hole pairs, mist CVD method was used to dope the Al into ZnO thin films with varied Al doping ratios and thermal annealing process was carried to enhance the quality of the films. Their structural, optical and photocatalytic properties were evaluated. It was found that the varied Al doping ratios were influenced on the properties of the AZO film. The crystallinity of obtained AZO films can be improved by using the AZO seeds layers as substrate during the mist CVD process. To further increase the surface-to-volume ratio of ZnO and enhance the dye absorption during photocatalytic measurement, well-aligned ZnO nanorods were fabricated on the AZO substrate, using CBD method with different reaction times. In order to prevent the direct contact of dye molecules and ZnO, and to reduce the recombination rates of electron and hole pairs, AZO was coated onto ZnO nanorods to fabricated AZO/ZnO core-shell nanostructures.

The main conclusions of this thesis were summarized as follows;

## 1. Fabrication of ZnO films with different thicknesses

In this part, mist CVD method was applied to fabricated the high uniform ZnO thin film on the glass substrate. The effect of thickness on the properties of ZnO thin film was investigated. The crystallinity of obtained ZnO films was improved by increasing the film thickness. Wedge-like structure was found on the surface of the ZnO film and the average grain size was increased with the thickness increasing from 300 nm to 750 nm. High uniform ZnO thin film with better crystallinity were obtained from 750 nm-thick ZnO film. The obtained all ZnO films showed the high transmittance of above 70% within visible range.

## 2. Fabrication of AZO films with varied Al doping ratios

In this section, we applied the mist CVD method to fabricate AZO films with varying ratios of Al doping. When the Al doping ratio was increased from 1% to 5%, the aspect ratios of the AZO nanosheets initially showed an increase followed by a decrease. Remarkably, the highest aspect ratio was achieved with the AZO film containing a 2% Al doping ratio. The surface roughness of all the AZO films remained below 10 nm, irrespective of the Al doping ratios. The crystallinity of the AZO films exhibited a consistent dominant growth direction along the (101) crystal plane. The 2% Al doped ZnO film exhibited the most favorable crystalline quality along the (101) direction. However, no distinct diffraction peaks were observed on the AZO films when the Al doping ratios were raised to 4 wt% and 5 wt%, indicating the films had transitioned to an amorphous state. The transmittance measurements of the resulting AZO films demonstrated high optical transmittance of approximately 90% within the visible spectrum. When the Al doping ratios were elevated from 1 wt% to 5 wt%, the calculated optical bandgaps were enlarged from 3.58 eV to 3.87 eV. Notably, the AZO film featuring a 2 wt% Al doping ratio exhibited high first-order reaction rate value of 0.004 $\text{min}^{-1}$ with the highest photodegradation efficiency and the

## 3. Fabrication of AZO seeds layer on the control of growth and crystallinity of AZO films by mist CVD method

In this section, we introduced a novel hybrid approach that synergizes RF magnetron sputtering with the mist CVD method, thereby enabling the fabrication of AZO films with precise control over growth orientation and a substantial surface area. Our investigation explored into the structural, optical, and photocatalytic attributes of these films.

The starting point involved depositing ZnO films with varying Al doping ratios through radio frequency magnetron sputtering, which subsequently acted as the foundational seed layers for the growth of AZO films by mist CVD process. Notably, it was affirmed that the growth direction of AZO film during the mist CVD process was inherently influenced by the crystalline quality of the as-deposited AZO thin films. This growth phenomenon followed the similar orientation as the underneath as-deposited AZO seed layer, exhibiting alignment along (0001) crystal orientation.

Our findings revealed a crucial interplay between lattice mismatch and columnar structure growth. Lower lattice mismatch between the AZO films and the seed layer emerged as a key factor that contributed to the promotion of higher columnar structure growth. Additionally, augmenting the aluminum doping ratio within the ZnO film led to a reduction in compressive stress. This, in turn, yielded an enhancement in the crystallinity of the AZO film.

Remarkably, the most remarkable photocatalytic efficiency was observed in the AZO film deposited onto the AZO seed layer featuring a 5 wt% Al doping ratio. The photocatalytic prowess of this arrangement was particularly noteworthy, spanning a wavelength range from 340 nm to 700 nm. This comprehensive photodegradation efficiency encompassed both the ultraviolet and visible regions of the electromagnetic spectrum. Specifically, the AZO film on the AZO-5wt% seed layer exhibited the highest photocatalytic degradation rate, quantified at 0.0043 min$^{-1}$.

## 4. Fabrication of well-aligned ZnO nanorods on AZO substrate by CBD method

Transparent conductive AZO films were employed as substrates for the fabrication of ZnO nanorods via the CBD method. Structural, optical, and photocatalytic properties of obtained ZnO nanorods were attributed by varying growth reaction times. A discernible trend emerged as ZnO nanorods with a well-organized hexagonal structure were successfully synthesized by extending the growth reaction time from 1 hour to 5 hours. Intriguingly, the crystallinity of the as-deposited AZO seed layer exhibited a direct correlation with the orientation of ZnO nanorod. Progressively elongated nanorods with a vertically aligned growth direction were achieved as the reaction time was prolonged. This intriguing growth phenomenon was governed by the interaction between the reaction times and the rate of nanorod growth. Specifically, longer reaction times facilitated the formation of more ZnO crystalline structures that aligned and stacked along the c-axis orientation, leading to a substantial increase in nanorod length. The most pronounced outcomes, both in terms of length and crystallinity, were realized in ZnO nanorods grown for 5 hours.

The optical transmittance properties of the resulting ZnO nanorods were impressive, with all samples exhibiting transmittance levels exceeding 70% within visible range. Remarkably, nanorods grown for 5 hours displayed exceptional MR dyes degradation efficiency under UV irradiation, coupled with notable high degradation rate of 0.00572 min$^{-1}$.

## 5. Fabrication of AZO/ZnO core-shells nanorods by mist CVD method

Following the growth of well-aligned ZnO nanorods on AZO substrate by CBD method, AZO was coated on the as-deposited ZnO nanorods using mist CVD method to reduce the recombination rate of photogenerated charged carriers. The influence of AZO coating on the structural, optical and photocatalytic properties of AZO/ZnO core-shells was investigated.

It was clearly observed that the hexagonal structure of as-deposited ZnO nanorods was transformed to circle structure when AZO was coated from 5 minutes to 20 minutes. When the AZO coating time was increased, the high concentration of Al was replaced to the ZnO and the structure was changed due to the different ionic radius between $Al^{3+}$ ions (0.53 Å), and $Zn^{2+}$ ions (0.74 Å) during the mist CVD process. As the coating time increased, the crystallinity was also enhanced along the (002) crystal plane and the highest crystallinity was obtained from the AZO/ZnO core-shells nanorods coated for 20 minutes. The high crystallinity in (0001) growth orientation could be contributed to absorb more $OH^-$ to generate ROS species and enhance the degradation efficiency. The transmittance of around 60% was occurred in the visible region and the optical bandgap was enlarged from 3.52 eV to 3.65 eV. The high degradation rate of 0.0053 $min^{-1}$ with high degradation efficiency was achieved from the AZO/ZnO core-shells coated with 20 minutes. Furthermore, this thesis investigated into the explanation of the photocatalytic mechanism underlying these promising outcomes, further enhancing our understanding of the complicated relationship between growth conditions and photocatalytic performance.

## 6. Innovative points of thesis

This thesis aimed to enhance the photodegradation efficiency of thin films related to zinc ZnO. The deposition of ZnO thin films with varying thicknesses was conducted using the mist CVD technique. Upon structural and optical analysis, it was determined that an increase in the thickness of ZnO films resulted in high crystallinity. Remarkably, the obtained ZnO films exhibited high transmittance of approximately 75% within the visible region. It was pointed that the applying of mist CVD could potentially increase the photodegradation efficiency of ZnO thin films.

Based on the serious issue of rapid charged carrier recombination in pure ZnO, which can unfavorably affect its degradation efficiency, Al was introduced into the ZnO film using mist CVD. To investigate the influence of Al doping, different Al ratios ranging from 1 wt% to 5 wt% were selected. Notably, due to the differing ionic radii between $Al^{3+}$ and $Zn^{2+}$, the structure of AZO film was transformed from an intertwined nanosheet structure to particle shapes as the Al concentration increased. The growth of AZO film was observed to align with the (001) growth direction during the mist CVD process, and the growth mechanism of AZO films was revealed. Photodegradation analysis of obtained AZO films indicated that, except for the 5 wt% Al, the remaining AZO films exhibited photodegradation efficiency. Notably, the highest degradation efficiency, with a rate of 0.004 $min^{-1}$, was achieved from 2 wt% Al. To further enhance the degradation rate, sputtered AZO seeds layer with different Al ratios (AZO-2wt%, AZO-5wt%) were applied to control the crystallinity and growth of the AZO film. As estimated, during the mist CVD experiment, the AZO seed layer played a pivotal role in directing the growth of the AZO film along the (0001) crystal plane. The AZO/AZO 5% film exhibited high crystallinity due to the low lattice mismatch between AZO film and AZO-5wt% seeds layer during mist CVD process. The high transmittance of around 85% was achieved, optical bandgaps were increased. Consequently, the degradation rate was further improved to 0.0043 $min^{-1}$.

In order to increase the degradation rate, ZnO nanorods were fabricated using the CBD technique to achieve the large surface area. Subsequently, obtained ZnO nanorods were coated with AZO to reduce the recombination rate of charged carriers, accomplished through mist CVD. Structural changes were observed as the AZO coating time was increased from 5 minutes to 10 minutes, eventually covered on the surface of ZnO nanorods. High crystallinity was achieved in AZO/ZnO core-shell nanorods coated with AZO for 20 minutes. The optical bandgap was enlarged with increasing of AZO coating time. Remarkably, AZO/ZnO core-shell nanorods coated with AZO for 20 minutes exhibited highest photodegradation effect. This concluded in the understanding of an AZO/ZnO core-shell structure characterized by high crystallinity and a large surface area, finally leading to a high degradation rate of 0.0053 $min^{-1}$.

In summary, as shown in the Fig. 6.1, the degradation effects were found to be improved gradually, which indicated that this researches successfully enhanced the photodegradation rates of ZnO related thin films from 0.004 $min^{-1}$ to 0.0053 $min^{-1}$ through a several innovative approaches involving mist CVD technique, doping with Al, controlling crystallinity using AZO seed layers, and fabrication of core-shell nanostructures. In Fig. 6.2, it can be clearly observed that the color of the original MR dyes was changed to the colorless during the degradation process which might be due to the high degradation effects of MR dyes by ZnO related thin films. The resultant ZnO related thin films are promising significant advancements in degradation efficiency of MR dyes, which is expected to apply in wastewater treatments.

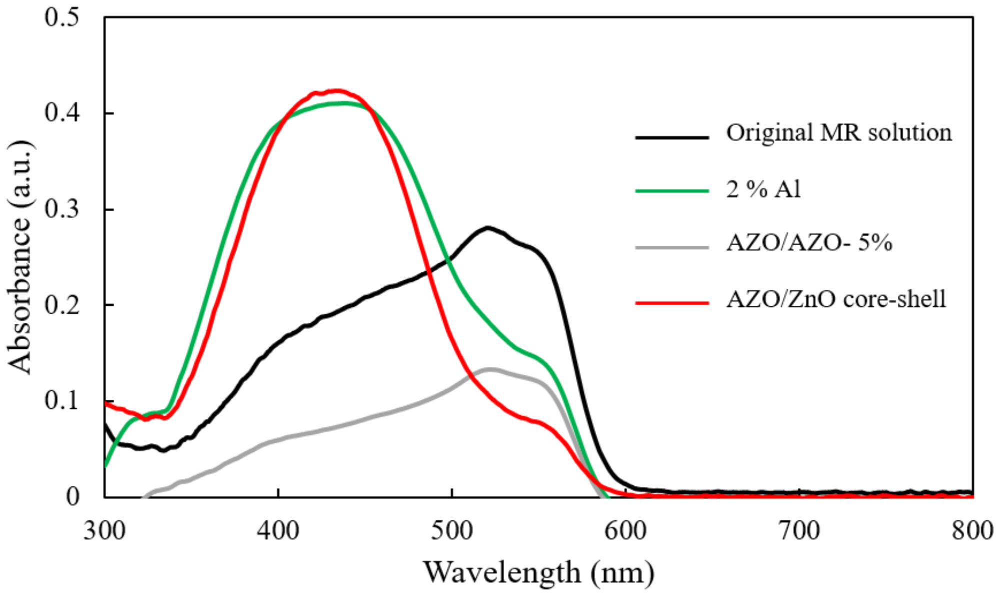

Fig. 6.1 Absorption spectra of MR solution for optimized samples.

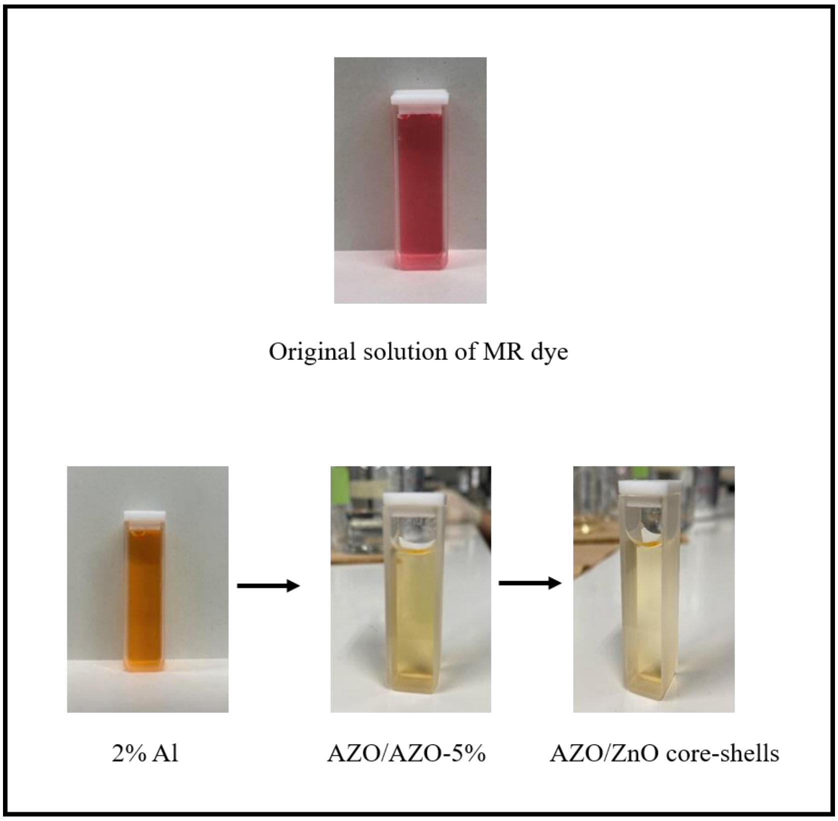
Original solution of MR dye

2% Al

AZO/AZO-5%

AZO/ZnO core-shells

Fig. 6.2 Color changes of MR dyes for optimized samples.

## List of Publications

## (A) Peer reviewed journal papers

### First Author (2)

1. **H.S. Wai**; C. Li. Effect of Aluminum Doping Ratios on the Properties of Aluminum-Doped Zinc Oxide Films Deposited by Mist Chemical Vapor Deposition Method Applying for Photocatalysis. Nanomaterials, 2022, 12, 195. Q1 level. (IF: 5.719)

2. **H.S. Wai**; C. Li. Fabrication of Well-Aligned ZnO Nanorods with Different Reaction Times by Chemical Bath Deposition Method Applying for Photocatalysis Application. Molecules, 2023, 28, 397. Q1 level. (IF: 5.138)

3. **H.S. Wai**; C. Li. Fabrication of AZO Core-Shells on ZnO Nanorods by Mist Chemical Vapor Deposition Method and Applying for Photocatalysis. (Scheduled to publish)

### Co-Author (1)

1. C. Li; **H.S. Wai**. Influence of Seeds Layer on the Control of Growth and Crystallinity of AZO Films Deposited by Mist Vapor Deposition Applying for Photocatalytic Activity. Topic in Catalysis, 2023. Q2 level. (IF:2.781)

## (B) Proceeding Papers (3)

1. **H.S. Wai**; M. Morimoto; C. Li. Fabrication of ZnO nanorods and applied for flexible Dye-Sensitized Solar Cells. IEEE Xplore, 2022, 128-131.

2. **H.S. Wai**; K. Takeda; C. Li. Pure Anatase Phase Titanium Dioxide Thin Films Prepared by Mist Chemical Vapor Deposition Applying for Photocatalysis. ECS Transactions, 2021, 104.

3. **H.S. Wai**; T. Ueda; C. Li. Oxygen Ratio effect on Zinc Oxide Films Fabricated by Radio Frequency Magnetron Sputtering for Photoluminescence Type Gas Sensor Application. IEEE Xplore, 2021, 141-143.

## (C) International conferences (4)

1. **H. S. Wai**; C. Li. Zinc Oxide Photocatalysis Synthesized by Mist Chemical Vapor Deposition, E-MRS Spring Meeting on 2, June, 2021, Online. (Poster Presentation)

2. **H. S. Wai**; T. Ueda; C. Li. Oxygen Ratio Effect on Zinc Oxide Films Fabricated by Radio Frequency Magnetron Sputtering for Photoluminescence Type Gas Sensor Application, AMFPD 28th International Workshop on 2, July, 2021, Online. (Oral Presentation) (Best Student Award)

3. **H. S. Wai**; C. Li. Effect of Aluminum Doping Ratios on the Properties of Aluminum-Doped Zinc Oxide Films Deposited by Mist Chemical Vapor Deposition Method Applying for Photocatalysis, MRM-J International conference on 13, December, 2021, Yokohama (Oral Presentation).

4. **H.S. Wai**; M. Morimoto; C. Li. Fabrication of ZnO nanorods and applied for flexible Dye-Sensitized Solar Cells, AMFPD 29th International Workshop on 7, July, 2022, Kyoto. (Poster Presentation).

5. **H.S. Wai**; I. Daichi; C. Li. Large surface of nano-structured ZnO thin film phosphor fabricated on GZO substrate for lighting application, IMID2023, Aug.21-25, 2023, Busan Korean. (Poster Presentation).

## (D) Domestic Conferences (4)

1. **H. S. Wai**; C. Li. Effect of Thickness on The Properties of ZnO Films Synthesized by Mist Chemical Vapor Deposition Method, 68th JSAP Spring Meeting on 16, March, 2021, Online (Oral Presentation).

2. **H. S. Wai**; C. Li. Effect of Thermal Annealing on the Properties of ZnO Films Deposited by Mist Chemical Vapor Deposition Method, 82th JSAP Autumn Meeting on 10, September, 2021, Online (Oral Presentation).

3. **H. S. Wai**; C. Li. Effect of thermal annealing on the properties of AZO film deposited by mist chemical vapor deposition and applying for photocatalysis, Applied Physics and Physics Chugoku-Shikoku Branch Joint Academic Lecture on 30, July, 2022, Takamatsu. (Oral Presentation).

4. **H. S. Wai**; C. Li. Modification of AZO Core-shells on ZnO Nanorods Applying for Photocatalytical Activity, Applied Physics and Physics Chugoku-Shikoku Branch Joint Academic Lecture on 29, July, 2022, Shimane University. (Oral Presentation).